GRAVITATIONAL REDSHIFT SPACE-PROBE EXPERIMENT

GP-A Project Final Report

Contract NAS8-27969

Principal Investigator: Dr. R. F. C. Vessot
Coinvestigator: Dr. M. W. Levine

Prepared for

National Aeronautics and Space Administration
George C. Marshall Space Flight Center
Huntsville, Alabama 35812

December 1979

Smithsonian Institution
Astrophysical Observatory
Cambridge, Massachusetts 02138

The Smithsonian Astrophysical Observatory and the Harvard College Observatory are members of the Center for Astrophysics

GRAVITATIONAL REDSHIFT SPACE-PROBE EXPERIMENT

GP-A Project Final Report

Contract NAS8-27969

Principal Investigator: Dr. R.F.C. Vessot
Coinvestigator: Dr. M.W. Levine

Prepared for

National Aeronautics and Space Administration
George C. Marshall Space Flight Center
Huntsville, Alabama 35812

December 1979

Smithsonian Institution
Astrophysical Observatory
Cambridge, Massachusetts 02138

The Smithsonian Astrophysical Observatory
and the Harvard College Observatory
are members of the
Center for Astrophysics

TABLE OF CONTENTS

SUMMARY

On June 18, 1976, a Scout D rocket was launched from Wallops Island, Virginia, carrying an atomic hydrogen maser oscillator system as the payload. The frequency of signals from the oscillator was monitored on the ground at Merritt Island, Florida, by using two hydrogen masers as comparison oscillators. The first-order doppler shift in the signals was eliminated by a go-return transponder link to the payload, and the resulting data, representing the relativistic shifts, were recovered and recorded. The objective of this experiment was to measure directly the effect of the gravitational potential on the frequency of an atomic hydrogen maser assuming it to be a "proper" clock.

In the experiment, a gravitational effect amounting to some 4.5 parts in 10^{10} was measured with an oscillator having a stability better than 1 part in 10^{14}. Therefore, to make the best possible use of the oscillator, we must account for all frequency shifts at the 2 to 5×10^{-15} level in $\Delta f/f$ in the system, and this, of course, includes all the phase variations that can cause such a shift to appear.

This report presents the experiment, a description of the data now available and the manner in which they were processed, and the results.

We wish to emphasize that this experiment was conducted by a large number of people and involved many different organizations. The program was managed by the George C. Marshall Space Flight Center of the National Aeronautics and Space Administration (NASA), which was also responsible for designing and assembling the payload structure and testing it before launch. NASA's Goddard Space Flight Center performed the task of tracking and data acquisition, and NASA's Langley Research Center and the Vought Corporation were responsible for the vehicle. We gratefully acknowledge the assistant of the Jet Propulsion Laboratory in the solution of the probe's trajectory. The Smithsonian Astrophysical Observatory provided the scientific and technical leadership and constructed the probe and ground clocks and the doppler cancellation system.

GRAVITATIONAL REDSHIFT SPACE-PROBE EXPERIMENT

GP-A Final Report
Contract NAS8-27969

1. INTRODUCTION

The test of the gravitational redshift predicted by Albert Einstein in 1907 had its beginnings with the development of atomic clocks in the 1950s; at that time, J.R. Zacharias' group at the Massachusetts Institute of Technology began working on cesium-beam clocks with an eye toward conducting an experiment between a clock placed on a mountain top and one in a valley to detect the predicted gravitational redshift. In a sense, Zacharias is a godfather of our present experiment. Its other godfather is N.F. Ramsey (1956), who discusses redshift measurement in Molecular Beams; more importantly, however, it was Ramsey who invented the hydrogen maser, in 1959.

The redshift test itself was first performed by R.V. Pound (Pound and Rebka, 1960) using a 75-ft elevator shaft. His now classic 1% test of the gravitational redshift was performed in 1960 by using the then recently discovered Mossbauer effect. It is interesting to note that this terrestrial test was made over a height approximately the same as that of the Scout rocket used in the present experiment and discussed below. The test by Pound and his coworkers, S.A. Rebka, Jr., and J.L. Snider, temporarily wiped out any further zeal to conduct a redshift experiment with clocks. To improve on their results would require far better clocks and enormously greater gravitational-potential differences between them.

However, the space program, in fact, did evolve methods to obtain larger gravitational-potential differences, and the atomic hydrogen maser was invented in 1959. This new type of oscillator was developed into a stable clock that could resolve time differences at the 10^{-14} level. With the entire effect of the earth's gravity (consisting

of 7 parts in 10^{10}) made available, thanks to the space program of the National Aeronautics and Space Administration (NASA), the prospect of a significant improvement over the 1% tests made by Pound became evident, and the redshift clock experiment was revived in 1966 by Ramsey, D. Kleppner, and R.F.C. Vessot (Ramsey et al., 1970).

Unfortunately, circumstances favoring this experiment soon changed. The Vietnamese war turmoil at universities, the guns and butter disputes, and above all, the tremendously expensive prospect of a Titan 3C vehicle and a 2000-lb payload all led to the termination of this version of the experiment. At about the same time, the maser group working at Varian Associates and Hewlett-Packard was successfully transplanted to the Smithsonian Astrophysical Observatory (SAO) to continue clock development in support of satellite tracking, astronomy, and very long-baseline interferometry.

Redshift experiments with clocks remained dormant until 1970, when, at the Conference on Experimental Tests of Gravitation Theories at the California Institute of Technology, Vessot and M.W. Levine gave a paper (1971) describing a 24-hour eccentric-orbit redshift experiment and its capabilities. This talk prompted N.G. Roman and J. Mitchell to suggest an exceedingly eccentric orbit, essentially vertically up and down, achievable by the Scout rocket system. While this was a far more modest version than the original experiment, we were encouraged to pursue it. After some initial calculations, we concluded that it was indeed a viable possibility; the most serious limitation would be to keep the payload weight low enough for the Scout rocket to achieve both a reasonably high altitude and a sufficient time aloft. This necessitated a complete replanning of the operational strategy of the experiment. The payload system would have to recover very rapidly from the severe transitions in environment and the trauma of the launch itself. The hazards of such a one-shot approach led to a very severe set of design constraints.

This report describes the new departure by NASA into the field of relativity in the flying of a dedicated payload as a laboratory experiment to study gravitation. The laboratory itself consists of the earth and its gravity field and extends over the total

range of distance traveled by the probe vehicle and the earth station used to obtain the data, the two being connected by electromagnetic signals propagated to and from the probe.

2. THE EQUIVALENCE PRINCIPLE

In 1907, Albert Einstein announced the principle of equivalence, which was doubtless inspired by his reflections on the universality of free fall – that all objects, regardless of their weight or composition, follow the same path when allowed to fall in a gravity field. Einstein extended his observation to state that "all freely falling, nonrotating laboratories are completely equivalent" and that all physics experiments done within the local confines of such laboratories are governed by the laws of special relativity. In particular, this means that it is impossible to distinguish, over small distances, the difference between a laboratory acted on by gravity and the same laboratory accelerated by mechanical means.

The equivalence principle is, in fact, the cornerstone of Einstein's General Theory of Relativity and of all other relativity theories that are based on a geometrical concept of space-time, the so-called metric theories.

Metric theories of gravity – in particular, General Relativity, the most promising of all theories – arose from a merger of curved geometry with the four-dimensional space that Einstein and others used to describe physics in inertial (or unaccelerated) frames of reference. The description for such inertial frames involves three dimensions of space plus the additional dimension of time and is called the Special Theory of Relativity. It is considered a flat space, since the four coordinate axes are straight lines and mathematically orthogonal. To include the effect of accelerations and gravitation, Einstein envisioned a warping of this coordinate system and used the geometry of curvilinear coordinates developed by Riemann and others to express the curvature. With extraordinary insight, he then related this curvature to physical parameters. The outcome is that physical experiments described in such a curvilinear coordinate frame include <u>all</u> aspects of acceleration and gravitation. Over small enough regions, the curvature is negligible and the "local" coordinates have the appearance of the flat space-time of special relativity. Figure 1 attempts to provide a visualization of this local connection between gravitation and acceleration.

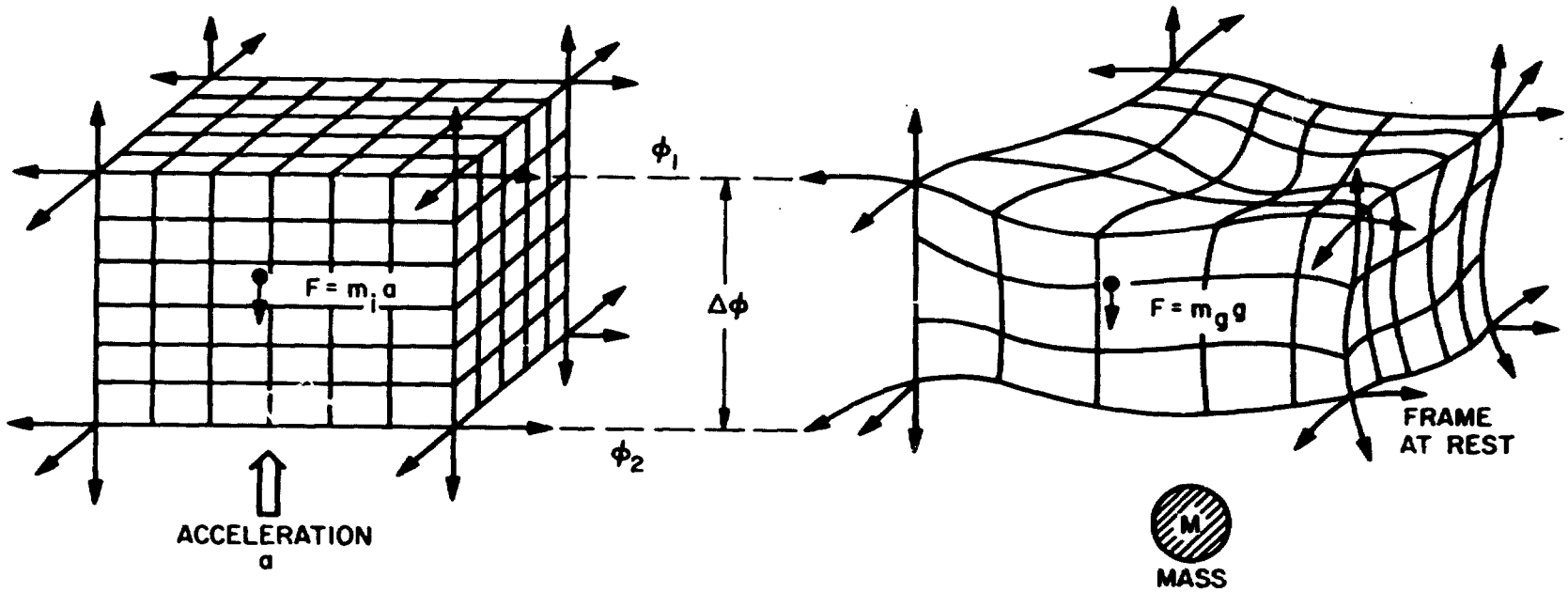

"ALL LOCAL, FREELY FALLING, NONROTATING LABORATORIES ARE FULLY EQUIVALENT FOR THE PERFORMANCE OF ALL PHYSICAL EXPERIMENTS" A. EINSTEIN - 1907 -

IT FOLLOWS THAT THERE IS NO WAY LOCALLY OF DISTINGUISHING BETWEEN THE PULL OF GRAVITY AND AN OPPOSITELY DIRECTED ACCELERATION

Figure 1. Einstein Equivalence Principle.

The experiments that led to this concept of space and time go back in history to the Renaissance, when Galileo Galilei is alleged to have tested the universality of free fall by dropping an iron cannon ball and a wooden ball from the Leaning Tower and observing that they fell in the same manner. Although this particular test is probably apocryphal, it is true that Galileo performed experiments to observe the rate of fall of objects made of different materials by using inclined planes to dilute the effects of gravity. He also made some observations on pendulums, but it remained for Isaac Newton to employ this technique in a more careful and quantitative manner.

At this point, it was recognized that there might be a conceptual difference between the acceleration due to gravity on a particle and the usual mechanical acceleration. The attribution of gravitational mass and inertial mass was given to the material body such that $m_i a = F$ and $m_g g = F$, and the question of the proportionality of m_i to m_g regardless of the composition of the mass resulted in experimental tests with pendulums of various types. In 1686, Isaac Newton published his monumental Mathematical Principles of Natural Philosophy – or Principia – and the very beginning of the English translation from Newtonian Latin by Motte in 1729 refers to a set of pendulum experiments "very accurately made;" the cover page and first page of this work are reproduced as Figures 2 and 3.

These experiments were later repeated by Bessel with a reported accuracy of about 1 part in 1000. Then, in the 1890, Eötvös (1922) conducted a series of tests using a torsion pendulum of very long period to look for the effect of the earth's gravity (m_g effect) and the effect of centrifugal acceleration (m_i effect) on various kinds of masses. He reached a level of about 10^{-9} in the constancy of the ratio of m_i to m_g. These data were undoubtedly a large influence on Einstein's thinking during the formation of his theories in the early 1900s. This type of pendulum experiment was also repeated with far greater precision using the sun's gravity at the earth's surface in the 1964 to 1971 time frame by R.H. Dicke (see Roll et al., 1964) and by V.B. Braginsky and V.I. Panov (1971), whose experiments achieved an accuracy between 10^{-11} and 10^{-12}.

The formal theoretical extension of these tests for matter as a generalization of the Einstein equivalence principle is still in progress, and various forms of the

PHILOSOPHIÆ
NATURALIS
PRINCIPIA
MATHEMATICA.

Autore *J S. NEWTON, Trin. Coll. Cantab. Soc.* Matheſeos Profeſſore *Lucaſiano,* & Societatis Regalis Sodali.

IMPRIMATUR.
S. PEPYS, *Reg. Soc.* PRÆSES.
Julii 5. 1686.

LONDINI,

Juſſu *Societatis Regiæ* ac Typis *Joſephi Streater.* Proſtat apud plures Bibliopolas. *Anno* MDCLXXXVII.

TITLE PAGE OF THE FIRST EDITION OF THE PRINCIPIA
(See Appendix, Note 3, page 627)

Figure 2. Newton's Principia.

MATHEMATICAL PRINCIPLES OF NATURAL PHILOSOPHY[1]

Definitions

DEFINITION I

The quantity of matter is the measure of the same, arising from its density and bulk conjointly.[2]

Thus air of a double density, in a double space, is quadruple in quantity; in a triple space, sextuple in quantity. The same thing is to be understood of snow, and fine dust or powders, that are condensed by compression or liquefaction, and of all bodies that are by any causes whatever differently condensed. I have no regard in this place to a medium, if any such there is, that freely pervades the interstices between the parts of bodies. It is this quantity that I mean hereafter everywhere under the name of body or mass. And the same is known by the weight of each body, for it is proportional to the weight, as I have found by experiments on pendulums, very accurately made, which shall be shown hereafter.

DEFINITION II[3]

The quantity of motion is the measure of the same, arising from the velocity and quantity of matter conjointly.

The motion of the whole is the sum of the motions of all the parts; and therefore in a body double in quantity, with equal velocity, the motion is double; with twice the velocity, it is quadruple.

[1 Appendix, Note 10.] [2 Appendix, Note 11.] [3 Appendix, Note 12.]

Figure 3. First page of Motte's translation.

equivalence principle have been devised. The so-called "weak" equivalence principle applies only to conclusions obtained from tests for matter, the "strong" principle being Einstein's. By invoking other physical laws, such as the conservation of energy, it can be argued that connections exist between the two. However, like all the laws of physics, the principle of equivalence has its ultimate justification in experimental test.

The general term "Equivalence Principle" is often referred to in terms of the type of data that support it. The Eötvös-type experiments expressing the universality of free-fall trajectories are referred to as supporting the Weak Equivalence Principle (WEP). The redshift phenomenon tests the Einstein Equivalence Principle (EEP). Schiff in 1960 argued that the WEP implies the EEP for any self-consistent theory of gravity. Lightman and Lee (1973) were able to prove Schiff's conjecture for electromagnetically interacting systems in a static spherically symmetric gravitational field. Ni (1977) later showed that by loosening their assumptions, violations of Schiff's conjecture could be found for spinning test bodies.

By removing the implicit assumption that material bodies are governed by the same metric as electromagnetic fields, Ni (1979) has recently investigated what is proved by certain aspects of different types of Equivalence Principle experiments typified by those of Eötvös, Hughes (Hughes and Robinson, 1960) and Drever (1961), and the redshift experiment being reported here.

Ni finds that the Eötvös and Hughes-Drever experiments demonstrate the equality of the space-space components of the two presumably different metrics at the 10^{-12} level. To describe the equality of the space-time components this level of accuracy must be reduced by a factor $v/c \sim 10^{-4}$, where v is the earth's orbital velocity, to yield a test at the 10^{-8} level. In the case of the time-time component comparison the 10^{-12} accuracy level must be reduced by a factor v^2/c^2 leading to a test at the 10^{-4} level. The present, direct test of the Einstein Equivalence Principle is aimed at this level of accuracy.

3. THE GRAVITATIONAL REDSHIFT AS A TEST OF THE EQUIVALENCE PRINCIPLE

The simplest demonstration for the predicted connection between the effect of gravitation on time (redshift) and the equivalence principle can best be given by the following type of argument, which is illustrated in Figure 4.

Let us assume that a radio transmitter is located at the east wall of a laboratory, with a receiver on the west wall a distance ℓ away. The signals will take a time $\Delta t = \ell/c$ to cross the laboratory, c being the velocity of light. Now let the laboratory be accelerated eastward by a bulldozer charging into the west wall. During the time interval Δt, the laboratory will be accelerated to a velocity $a\Delta t = \underline{a}\ell/c$, and the frequency of the received signal at the west wall will be doppler shifted by a fractional amount: $\Delta f/f = \Delta v/c = \underline{a}\ell/c^2$. The question is whether, if we tip the laboratory on edge east end up, the fractional shift would be $\Delta f/f = \underline{g}\ell/c^2$; that is, can we replace $\underline{a}$ by $\underline{g}$? This expression takes on the usual form for expressing redshift if we write $\underline{g}\ell$ as the Newtonian potential $\Delta\phi$ and thus obtain

$$\frac{\Delta f}{f} = \frac{\Delta\phi}{c^2} \quad . \tag{1}$$

We can answer the above question if we write the metric expression for an interval of space-time ds using the free parameters β and γ, as done in the static and isotropic expression given by Eddington (1922) and Robertson (1962), and <u>also</u> including in the redshift a free parameter α. We have

$$ds^2 = \left(1 - \frac{2\alpha M}{R} + \frac{2\beta M^2}{R^2}\right) c^2 dt^2 - \left(1 + \frac{2\gamma M}{R}\right)(dx^2 + dy^2 + dz^2) \quad ; \tag{2}$$

here, $M/R \equiv Gm/c^2 r_c$, where G is the universal constant of gravitation, m is the mass of the spherically symmetric gravitating body, and r_c is the distance from its center.

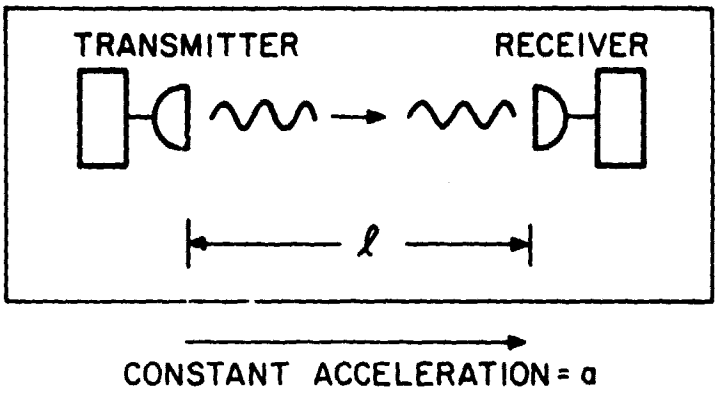

$$\Delta t = \frac{\ell}{c}$$

$$\Delta V = a\Delta t = \frac{a\ell}{c}$$

$$\frac{\Delta f}{f} = \frac{\Delta V}{c} = \frac{a\ell}{c^2}$$

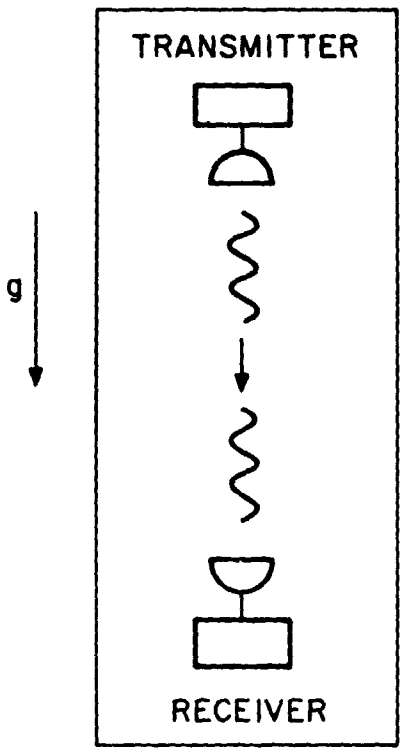

DOES $\frac{\Delta f}{f} = \frac{g\ell}{c^2}$

WHEN WE REPLACE
a BY g FROM GRAVITY ?

Figure 4. Illustration of Equivalence Principle.

If we connect two fixed regions of space-time with light signals, keeping to terms of order c^2, we have

$$\frac{\Delta f}{f} = \alpha \frac{\Delta \phi}{c^2} \quad . \tag{3}$$

Since we are interested in the departure of α from unity, we can write $\alpha = 1 \pm \epsilon$, where $\pm\epsilon$ is a measure of the invalidity of the principle of equivalence. We should note here that the very concept of the existence of a metric description of space time depends on α being equal to 1 and that the use of the symbol in equation (2) (which is a metrical description) is therefore tantological. Nevertheless we choose to retain it and defend its presence as a means for testing the self consistency of the theory.

4. THE BASIC CONCEPT OF THE GRAVITATIONAL REDSHIFT SPACE-BORNE EXPERIMENT

The redshift experiment using clocks in a spacecraft and on earth compared by electromagnetic signals can be described in simple terms as follows: "Take a perfect (or "proper") clock and position it at several locations having a different gravitational potential and measure its rate at each position by comparing it to a clock that is at a constant gravitational potential." By plotting the relative frequency difference versus gravitational potential, we can test the extent the slope of this relationship departs from unity in equation (1). The operation of comparing is done by means of light signals, either by looking at the hands of the clock in the literal sense or by transmitting time information (or phase), to give the rate of time variation (or frequency) at a particular gravitational potential measured in terms of the standard or fixed clock. Here, the clocks are assumed to be totally unaffected by gravity fields or by acceleration. They are assumed to be the proper clocks of theoretical relativity.

At present, the best embodiment of a proper clock for the purpose of such a test is the atomic hydrogen maser, whose stability, described in terms of the Allan two-sample variance (Allan, 1966), is shown in Figure 5. This form of variance, often referred to as the Kolmogorov variance, expresses the 1σ expectation value of the frequency difference between adjacent measurements each of duration, τ, in a time-ordered series of data. Since the maser develops stability better than 1 part in 10^{14} for time intervals beyond 100 sec, we need at least 100 sec to get data for comparison with a 1σ accuracy of frequency at the 1×10^{-14} level.

The next requirement is to place the clock at different gravitational potentials. In this test using earth's gravity, we predict the redshift versus radial distance from the earth's center as shown in Figure 6. The idea of making comparisons at different gravity potentials can be implemented by using a nearly straight up and down ballistic trajectory and measuring the redshift frequency continuously as the vehicle travels in space.

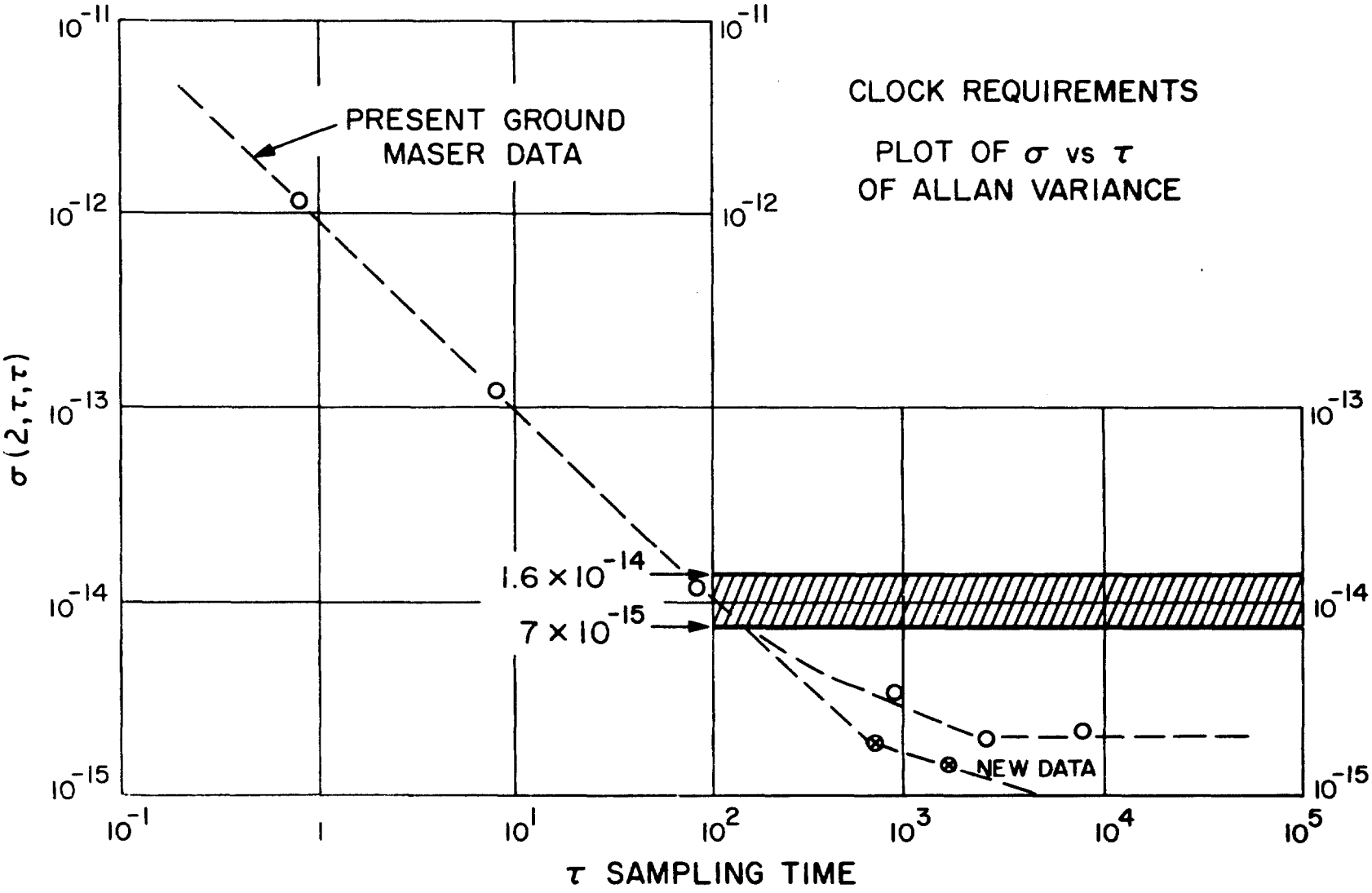

Figure 5. Clock performance requirements.

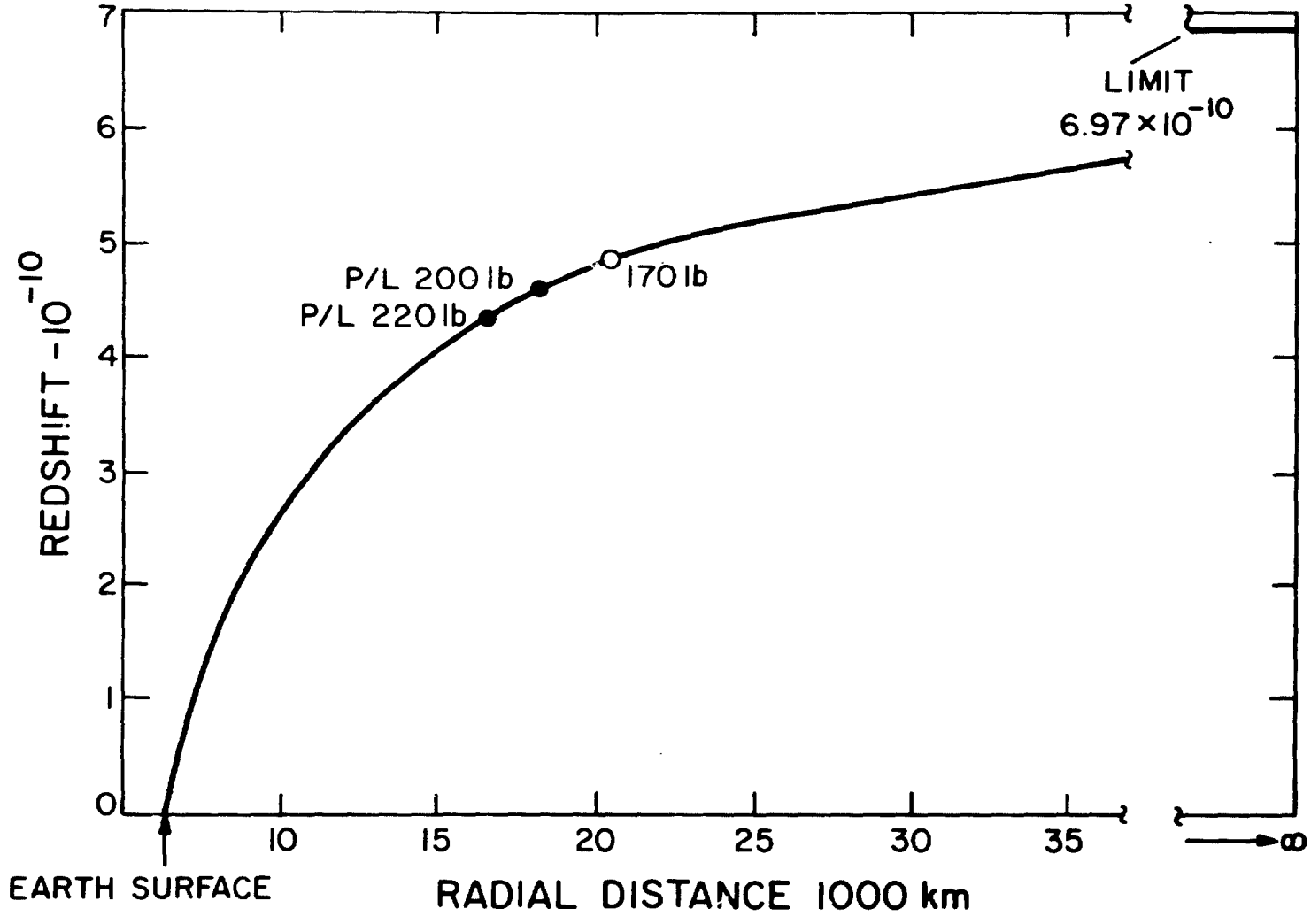

Figure 6. Redshift vs. radial distance from earth center.

The original idea of using an eccentric orbit would allow the experiment to be repeated many times, thus improving the statistical validity of the data; however, under conditions such as this case where the rocket's weight-carrying capabity is small and the payload operating time is limited, it is better to put the rocket's energy into obtaining gravitational potential. In other words, the strategy is to reach as high an altitude and to obtain as many data as possible across a large difference in gravity potential. Figure 6 shows roughly the altitude and redshift for a range of payload weight between 200 and 220 lb (91 to 100 kg) when propelled nearly vertically by the four-stage Scout D rocket system.

At this point, it is probably more realistic to refer to the clock as an oscillator and turn the discussion in terms of frequency rather than time or phase. While the distinction is mostly one of semantics, for clarity in pictorial discussions, we will use frequency, which is the parameter we are comparing as a function of gravitational potential. Our experiment, then, is to test the observed frequency of the probe clock in the manner shown in Figure 7 and establish the nature of the parameter $\alpha = 1 \pm \epsilon$.

Since the test is expected to span a range of 4×10^{-10} in $\Delta\phi/c^2$ and our oscillators have stability greater than 1×10^{-14} throughout the expected time interval of the mission we can aim for a maximum sensitivity in the determination of the value of α of $1 \times 10^{-14}/4 \times 10^{-10}$ or 25 parts per million. This excludes the question of systematic errors inherent to the experiment hardware, signal propagation and of our knowledge of the trajectory upon which our predictions will depend. Because the probe's trajectory is ballistic with an apogee altitude of about 10,000 km, we will encounter large first-order doppler shifts in the microwave signals connecting the space and earth station clocks. Expressed as fractional frequency changes these will be on the order of 1 to 2×10^{-5}, some nine orders of magnitude greater than the stability of the oscillators. The first-order doppler effect must be accounted for at the 10^{-9} level if we are to achieve the expected accuracy in the redshift measurement.

In our considerations the possible error sources and the generation of error budgets to guide the design of the experiment, we insist that the errors in the oscillators should predominate and that the oscillators and their associated signal processing equipment will perform within or below the shaded band in Figure 5. It is obvious

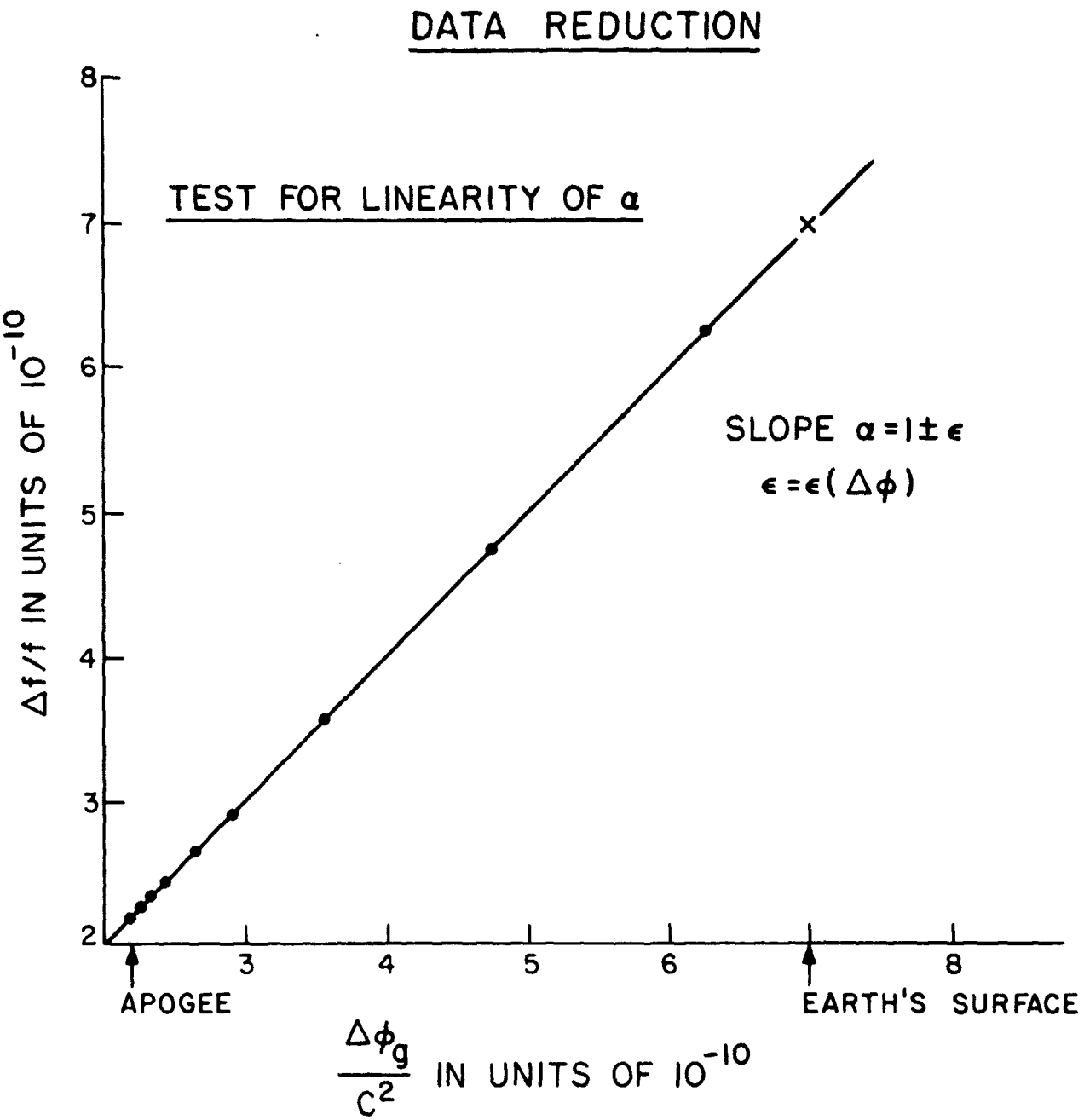

Figure 7. Illustration of test for linearity of α.

that frequency contributions to error at the level of a few parts in 10^{15} can mount up, even when considered to be statistically independent and combined in a root-sum-squares manner. For this reason, all frequency errors at the 2×10^{-15} level or greater in our error budgets are considered to be significant.

5. THE DOPPLER CANCELLATION SYSTEM

Next to the clocks, the most crucial part of the experiment is the system that removes the first-order doppler effects so that the relativistic data are revealed for measurement. This system is shown in very simple form in Figure 8, where a three-link microwave system connects the probe and earth oscillators. One link transmits the probe oscillator signals to the earth, where the comparison is made. This comparison is shown as the beat signal from the microwave mixer M1 in Figure 8 and contains the first-order doppler and relativity information. A second microwave system attached to the probe receives a maser-controlled uplink signal from earth and phase coherently retransmits it back to earth via a transponder. The returned signal is compared with the uplink signal and mixer M2 in Figure 8; the resulting beat frequency contains twice the first-order doppler-frequency shift, which, when divided in frequency by 2, is subtracted from the probe-maser signal at mixer M3, thus removing the first-order doppler frequency from the output frequency.

The development of this system began with the original suggestion made in 1960 by Badessa et al. Since we will require continuous operation of three microwave links each will require its own frequency to prevent self jamming and regeneration. Figure 9 conceptually describes the use of rational frequency multipliers to generate the separate frequencies required.

It was pointed out to us by Prof. R. V. Pound (1973) that the use of three separate carrier frequencies in the S-Band region, spaced apart in frequency by the transponder input-output frequency ratio imposed by our use of the existing Unified S-Band system transponder, would produce substantial ionospheric doppler shifts that result from the rapid changes in columnar electron density in the signal paths. The system, shown conceptually in Figure 8 will cancel nondispersive propagation effects such as the refraction from the earth's troposphere; however to assess its behavior in a dispersive medium such as the ionosphere we must look at it in more detail.

To bring the properties of the doppler and ionosphere cancelling system together, we can discuss the total doppler effect $\Delta f_d/f$ in terms of the rate of change of the

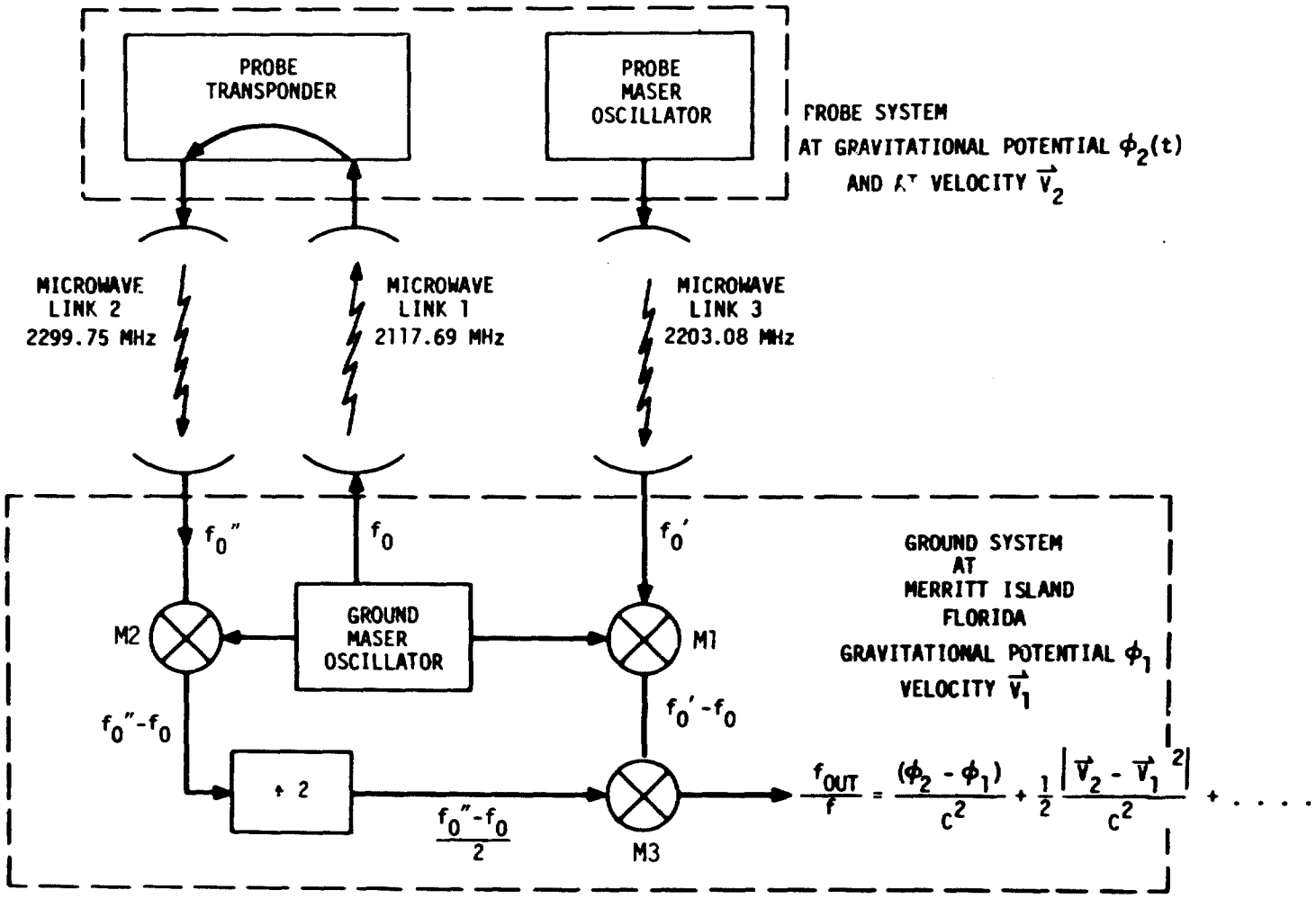

Figure 8. Doppler cancelling system concept.

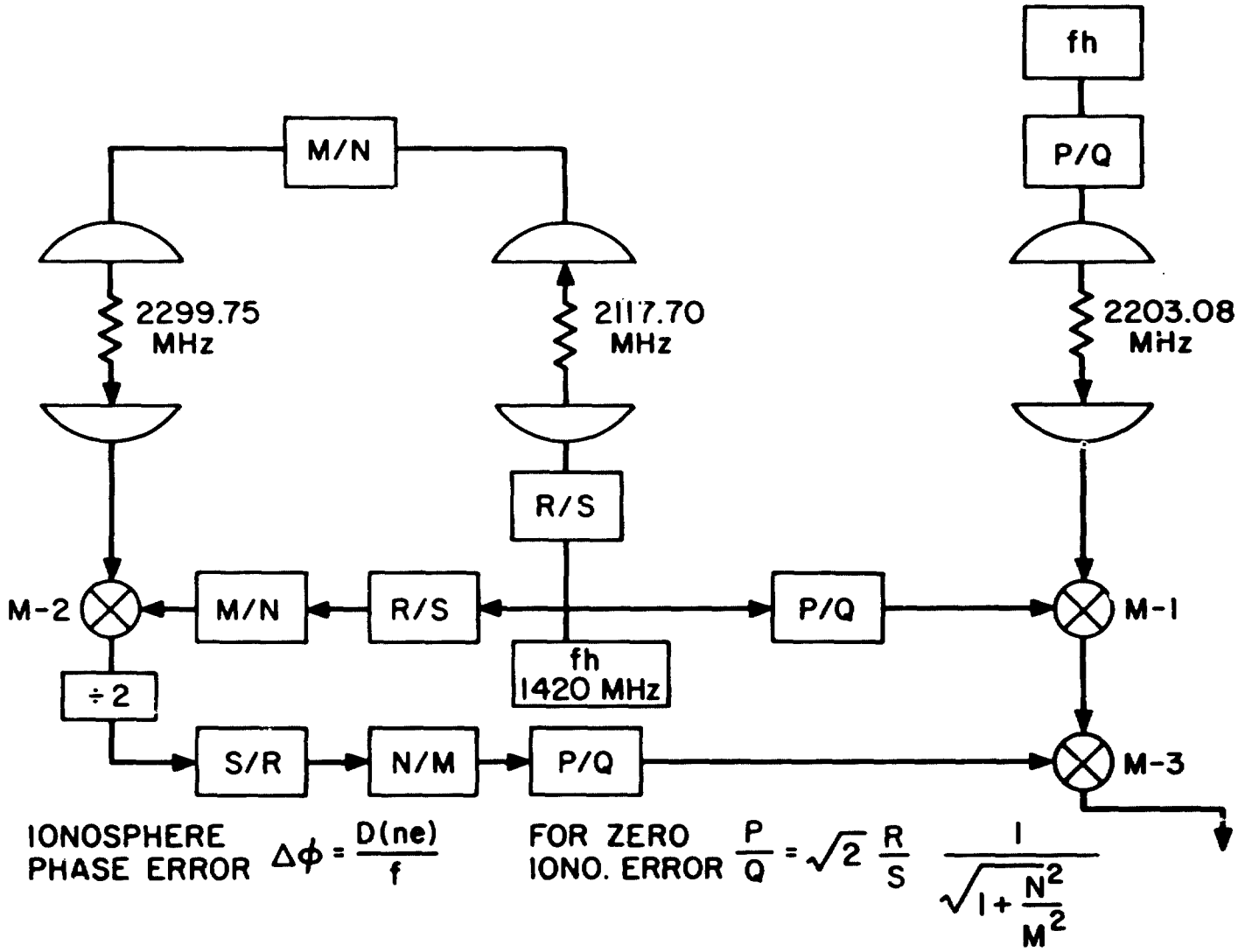

Figure 9. Doppler and ionospheric effects cancellation system concept.

"optical path" of the electromagnetic energy through the medium having a refractive index n. The atmospheric and ionospheric doppler shift resulting from propagation along a path P is as follows:

$$\frac{\Delta f_d}{f} = \frac{1}{c} \frac{d}{dt} \int_P n(t)\, ds \quad . \tag{4}$$

Here, n(t) has three components corresponding to a vacuum (n = 1), atmospheric refraction n_a, and ionospheric refraction n_i. Of these, only the ionospheric term depends on frequency for signals near 2 GHz. Consequently except for ionospheric dispersion, all effects between the spacecraft and ground stations are cancelled provided that the antenna system treats the signals at all three frequencies in the same manner.

This point is crucial to the success of the technique, for it is the antenna that represents the trajectory of the payload, and its position is considered to be the point in space that interacts with the upcoming electromagnetic signal from the ground-station transmitter and simultaneously phase coherently retransmits this signal while simultaneously transmitting the clock downlink signal to the earth.

For the moment, we can consider that our system will strictly account for the probe motion as represented by its antenna, and the cancellation is complete if n = 1. The nondispersive refraction from the atmosphere is cancelled exactly only if the path integral P of the upward signal from the ground station is exactly the same as that of the downlink signals from the clock and the transponder. These effects and those of the earth station motion during the light time of the signals will be considered later.

To make use of existing Unified S-Band (USB) transponder designs, we adopted a turn-around frequency ratio of 240/221 for the transponder uplink and downlink. The resulting separation of these frequencies requires a technique to cope with ionospheric dispersion.

Phase shifts that result from propagation through the ionosphere can be evaluated by tracing the signals shown in Figure 9. The refractive component of the ionosphere n_I is a function of position $\vec{\xi}$ and time I, and depends on electron density and magnetic field as follows:

$$n_I(\vec{\xi}, t) = \left[1 - \frac{f_n^2}{f^2 \left(1 \pm \frac{f_m}{f}\right)} \right]^{1/2} \quad . \tag{5}$$

Here, f is the propagation frequency and the plasma frequency $f_n = \frac{1}{2\pi} \frac{\rho}{\epsilon_0} \frac{e^2}{m}$ depends on the number density of electrons $\rho(\vec{\xi}, t)$, the electronic charge to mass ratio e/m, and the permittivity of free space ϵ_0. The frequency f_m is the electron gyromagnetic frequency 2.8 mHz per oersted of magnetic field. The ratio f_m/f is less than 1×10^{-3} even for maximum terrestrial magnetic fields and this term can be ignored. Under these conditions following Tucker and Fannin (1968) we identify the do: nt term of a power series expansion in frequency f as follows:

$$n_I(\vec{\xi}, t) = \left(1 - \frac{1}{4\pi^2} \frac{\rho}{\epsilon_0} \frac{e^2}{m} \frac{1}{f^2}\right)^{1/2} = 1 - \frac{1}{8\pi^2} \frac{\rho}{\epsilon_0} \frac{e^2}{m} \frac{1}{f^2} \quad , \tag{6}$$

and

$$\Delta f_I = -\frac{f}{c} \frac{d}{dt} \int_P n_I \, ds = \frac{1}{8\pi^2 f c \epsilon_0} \frac{e^2}{m} \int_P \rho(\vec{\xi}, t) \, ds \quad . \tag{7}$$

In the system shown in Figure 9 we can trace the frequency shifts resulting from changes in the columnar electron density $\rho(\vec{\xi}, t)$ and obtain the ionospheric frequency error at the input to mixer M3

$$\Delta f_{I\ 2\ way} = \frac{1}{8\pi^2 f_h c \epsilon_0} \frac{e^2}{m} \left[\frac{d}{dt} \int_P \rho(\vec{\xi}, t) \, ds \right] \left(\frac{M}{N} + \frac{N}{M} \right) \frac{1}{2} \frac{S^2}{R^2} \frac{P}{Q} \frac{N}{M} \quad . \tag{8}$$

Here, f_h is the hydrogen maser output frequency (Hellwig et al., 1970) 1,420,405,751.68 Hz and M/N, P/Q, R/S are numerical ratios used to synthesize the frequencies in the three microwave links. Similarly, for the spacecraft oscillator downlink we find an ionospheric frequency shift given at the other input to mixer M3 as follows:

$$\Delta f_{I\ 1\ way} = \frac{1}{8\pi^2 f_h c \epsilon_0} \frac{e^2}{m} \left[\frac{d}{dt} \int_P \rho(\vec{\xi}, t)\, ds\right] \frac{Q}{P} \quad . \tag{9}$$

The mixer M3 produces a net shift given by the difference of these two shifts:

$$\Delta f_{error} = \Delta f_{I\ 2\ way} - \Delta f_{I\ 1\ way} = \frac{1}{8\pi^2 f_h c \epsilon_0} \frac{e^2}{m} \left[\frac{d}{dt} \int_P \rho(\vec{\xi}, t)\, ds\right] \times \left[\frac{Q}{P} - \frac{S^2}{2R^2} \left(1 + \frac{N^2}{M^2}\right) \frac{P}{Q}\right] \quad . \tag{10}$$

The ratios P/Q, M/N, and R/S can be chosen to make the last term equal to zero and, to the extent that the approximations made in equation (7) hold true, including the effects of ray path separation owing to dispersion and elapsed time between upgoing and downgoing rays, the effect of the ionosphere can be cancelled.

Since our system made use of already existing Unified S-Band equipment, the transponder ratio, M/N, as mentioned earlier was 240/221. This predetermined ratio and the usable frequency range of the USB system led us to choose P/Q = 76/49 and R/S = 82/55.

The residual error given by

$$\frac{\Delta f_e}{\Delta f_{1\ way}} = 1 - \frac{S^2}{2R^2} \left(1 + \frac{N^2}{M^2}\right) \frac{P^2}{Q^2}$$

when the ratios are chosen as above is

$$\frac{\Delta f_e}{\Delta f_{1\ way}} = 2.5 \times 10^{-5} \quad .$$

For typical ionospheric conditions and with the trajectory flown we find that $\Delta f_{1\ way}/f$ is, at worst, about 10^{-10} so that $\Delta f_e/f$ is, at worst, 2.5×10^{-15}.

The ionospheric frequency signature (Figure 10) shows the uncancelled behavior predicted from measurements of ionospheric columnar electron density made during the experiment.

The extent to which the approximations made in equation (7) and the effect of ray bending and retardation (nonsimultaneous ray paths) through the troposphere and ionosphere have been studied by Mr. C. Baugher at the Marshall Space Flight Center using more exact ray-tracing methods (1980). These values of the ionospheric profile were measured at 1145 and 1330 GMT, June 18, 1976. These calculations were made to estimate the f^{-2} and f^{-3} terms not included in the expansion given in equation (7). Here the f^{-2} term is identified with Faraday rotation of the plane of polarization; this is a nonreciprocal effect in the propagation direction. The f^{-3} term is chiefly associated with the differential bending of the ray paths that result from ionospheric dispersion. The system, in fact, cancels the electromagnetic effects of ray paths that are not exactly coincident in time but are separated by a time interval of r/c sec.

Taking these effects into consideration, the ray-tracing computations, including time delay, between uplink transmission and downlink reception, show a significant effect $\Delta f/f > 0.5 \times 10^{14}$ only during the last 2 min before impact. As will be seen later, the data taken after the uplink transmitter interruption, which occurred 12 min before impact, were not considered reliable and have not been used in the present reports of the redshift results.

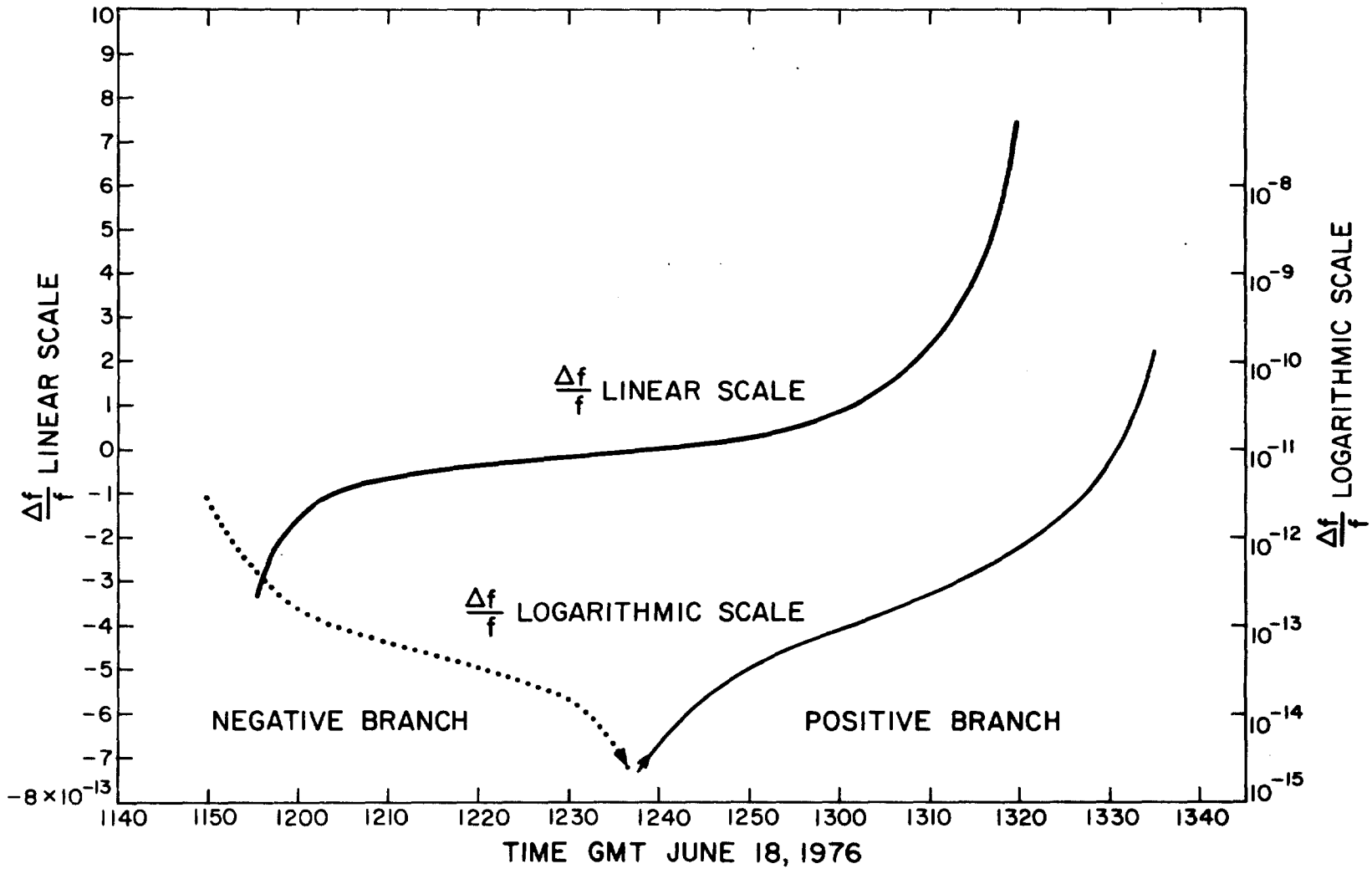

Figure 10. Uncancelled ionospheric frequency shifts for trajectory flown June 18, 1976.

Variations in the troposphere and ionosphere that occur rapidly compared to the light time (which is always less than the value at apogee of 0.03 sec) will produce phase variations that are not cancelled by this system. These will occur only at Fourier frequencies higher than 33 Hz and since our data averaging intervals to obtain frequency stability at the 10^{-14} level are greater than 100 sec, these short-term phase noise fluctuations will not affect the experiment.

C. PHASE STABILITY CONSIDERATIONS IN THE PROBE AND GROUND STATION ANTENNA SYSTEMS

A very critical factor in the frequency stability of the system shown in Figure 9 is the phase stability of the electronic systems, cables, and propagation paths. This is vividly brought into focus when we consider that a fractional frequency shift of 1×10^{-14} at 2.2 GHz results from a change of only 1.3×10^{-2} rad in 100 sec or a change in cable length of 0.03 cm in the same time interval. Questions relating to the dispersive and nondispersive aspects of the propagation have been discussed and we have seen that all perturbations resulting from the relative motion of the antennas are cancelled within the light-time interval r/c. However, this cancellation does not apply to the cables connecting the ground station antenna with the transmitters and receiver parts of Unified S-Band system (USB) located some distance away. In the normal USB system the two receivers share a common low-noise "front end" and the signals are carried via common cables to the phase-locked tracking filter receivers. The uplink transmitter signals are sent to the antenna along a separate cable. Because the doppler cancelling system subtracts one-half the two-way doppler signal from the one-way, only one-half of the phase fluctuations in the receiver cable are cancelled and none of those variations of the transmitter cable are accounted for. In addition to this totally uncancelled aspect of the transmitter cable there existed the very large uncontrolled phase variations in the signal path from the transmitter exciter, through the many stages of frequency multiplication and on to the high power amplifiers. This problem was solved by using a separate, specially controlled, cable to sample the transmitted power near the feed point of the antenna and bring this signal back to the control station where the hydrogen maser master oscillators were located. The phase of this signal was compared with the phase of a maser-generated signal, and the offset signal, proportional to the phase difference, was used to control the phase of the transmitter master oscillator. In this way the fluctuation of cable length, power amplifier and frequency multiplier stages were all placed within the phase-locked loop and the output signal.

In the case of the spacecraft antenna, transponder, and downlink transmitter, the situation was very different. Here cable distances were short and the transponder and transmitter operated their three separate links through a triplexer that routed incoming signals to the receiver and sent both outgoing signals to the antenna.

The chief concern in the probe was the phase stability of the transponder and downlink transmitter during the large temperature changes expected when the spacecraft was launched into space. Since no time could be allowed to restabilize these components while in space their temperature control systems were required to cope with unusually large perturbations. The usual USB transponder design incorporated two separate units within a single enclosure. For the present application, the USB transponder was modified by replacing one transponder section with the frequency translator system, shown as the P/Q block in Figure 9. The complete transponder and translator package were temperature-controlled by a liquid ammonia boiler, which kept the temperature within a range of 0.25°C during the part of the mission when useful data were acquired. Our strategy for the one-shot mission was to stabilize the device thermally for several days before the flight and then to launch it into space with the same thermal-control system used on the ground. The thermal control system, specially developed at the Marshall Space Flight Center for this experiment, consisted of an ammonia boiler that contains enough liquid to last the duration of the mission. The boil-off temperature was controlled by gas pressure, which was maintained by a venting orifice. Remarkably close control of temperature was achieved in both the transponder and the translator; these units were located in the same insulated container housing the USB transponder, which was in thermal contact with the boiler. Performance data and the calibrations for phase with temperature are discussed in Section 14.

Phase variations resulting from the antenna radiation patterns are also important. In the case of the ground station antenna, which is steered toward the probe, the signal propagation directions is very constant with respect to the axis of the antenna. In the case of the probe, which did not have a steerable antenna, the signal phase depended on the relationship between the signal propagation vector and the direction

of the antenna dipole; the phase shifts also depended on the frequency of the signal in each of the three links.

Since the probe was spin-stabilized, the axis of rotation was chosen as the center of symmetry of the dipole antenna system. The antenna, including its ground plane, in fact encompasses the entire exterior conducting surfaces of the vehicle. The space vehicle was therefore completely enclosed in an electrically conductive shroud that was made symmetric in rotation about the spin axis.

The dipole antenna that operated the three links was located on axis in a 10° conical ground plane. Under these conditions, rotation of the payload will cause no change in signal phase. Because the location of the phase center of the antenna is slightly different for each frequency some change of phase with aspect angle is expected. Careful atenna design was required to provide a low level of phase variation.

Figure 11 shows the predicted combined effect from the three signal links when processed by the system shown in Figure 9.

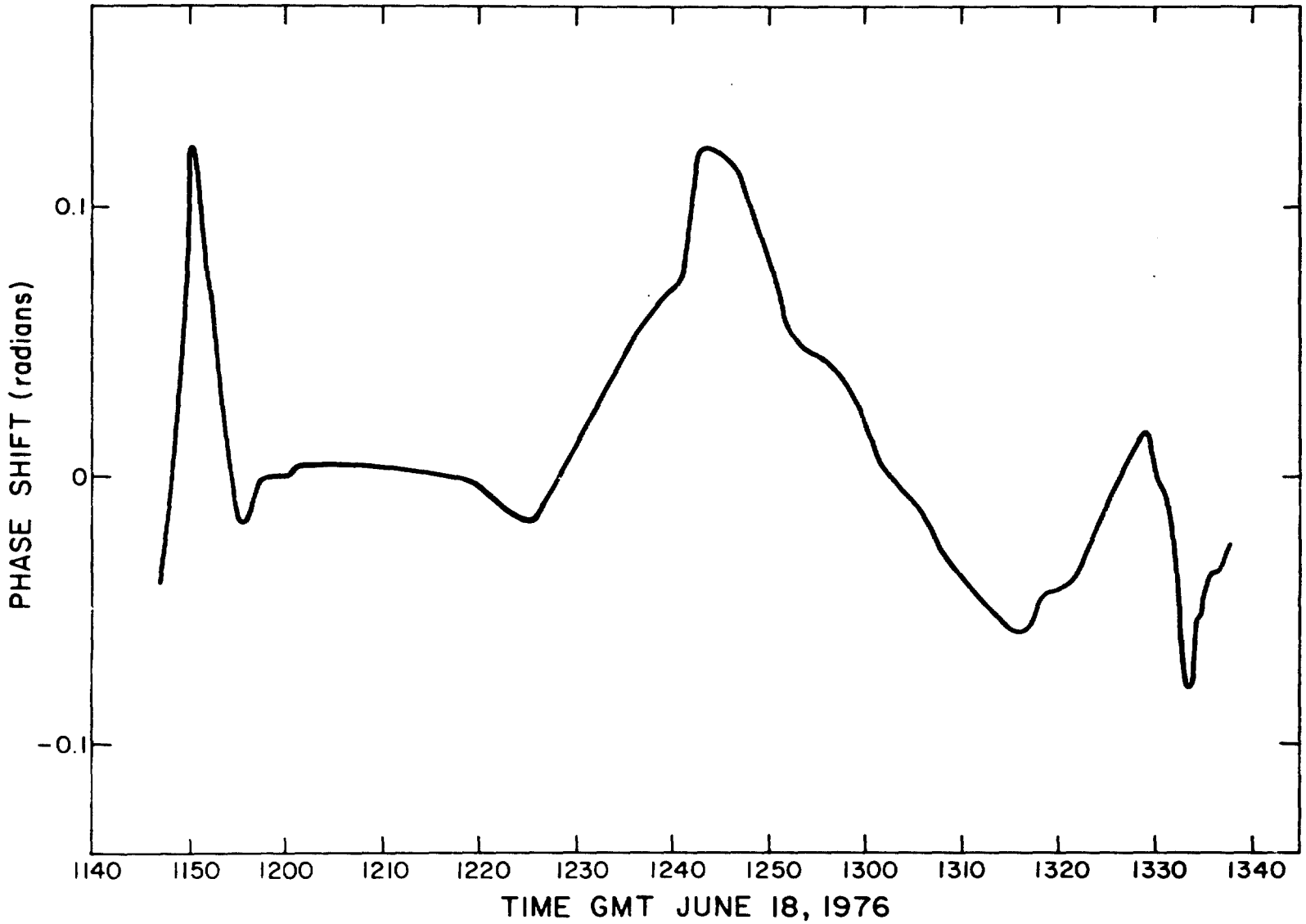

Figure 11. Phase shift signature from probe antenna aspect variations as seen from the ground station.

7. PREDICTIONS MADE FROM RELATIVITY THEORY

This section discusses the behavior of the output frequency from the system shown in Figure 9 according to the predictions made from the general theory of relativity. The derivation follows the notation and method used by Kleppner, Vessot, and Ramsey (1970) to obtain the relativistic prediction of the one-way and two-way doppler shifts, which are then combined by subtracting one-half the two-way signal from the one-way signal to obtain a doppler-cancelled signal containing only relativistic effects.

We choose an inertial earth-centered coordinate frame as shown in Figure 12 and apply the doppler equation of general relativity to an oscillator having a proper frequency f_0 at a position $\vec{r}_2$ moving with velocity $\vec{\beta}_2$ measured by receiving a signal of frequency f' at a position $\vec{r}_3$ moving with velocity $\vec{\beta}_3$. The unit vector describing the inertial propagation direction from the $\vec{r}_2$ position to the $\vec{r}_3$ position is $\vec{\epsilon}_{23}$. Keeping terms of order c^{-2}, we obtain f', the frequency at the ground station received from the probe:

$$f' = f_0 \left[\frac{1 + (2\phi_2/c^2) - \vec{\beta}_2^2}{1 + (2\phi_3/c^2) - \vec{\beta}_3^2}\right]^{1/2} \left[\frac{1 - \vec{\beta}_3 \cdot \vec{\epsilon}_{23}}{1 - \vec{\beta}_2 \cdot \vec{\epsilon}_{23}}\right] , \qquad (11)$$

where ϕ_2 and ϕ_3 are the gravitational potentials of the probe and the ground station, respectively. If we expand this expression binomially, the term in the first bracket is recognized as containing $1 + [(\phi_2 - \phi_3)/c^2] - [(|\vec{\beta}_2^2| - |\vec{\beta}_3^2|)/2]$, which is the combination of the redshift and second-order doppler effects. The second bracket in equation (11) contains the first-order doppler effects, which are some 10^5 times larger.

In a similar manner, we can successively apply the doppler equations of general relativity to the transponder signals:

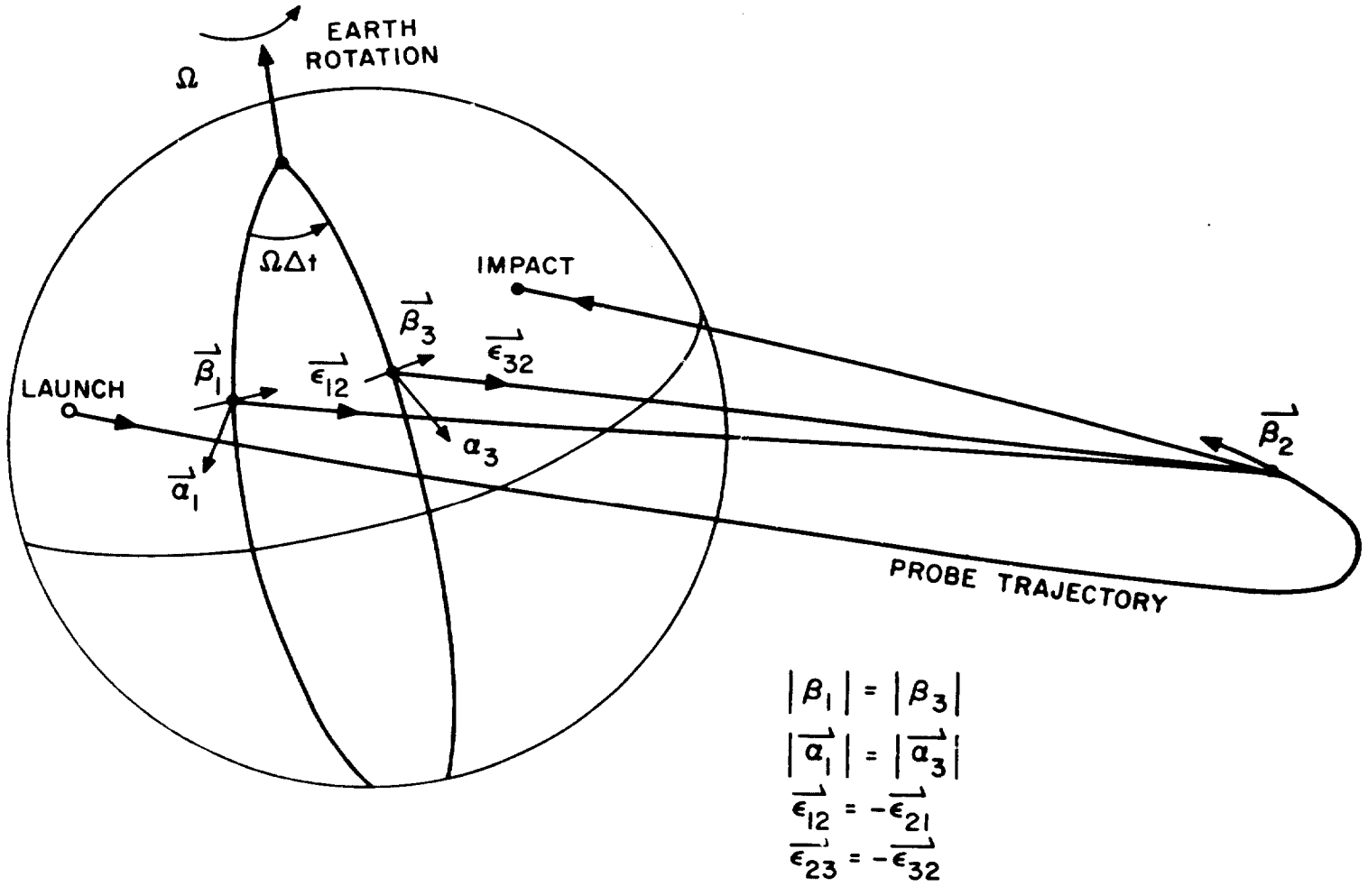

Figure 12. Geometry of acceleration, velocity, and signal propagation vectors.

$$f'' = f_0 \left[\frac{1 + (2\phi_1/c^2) - \vec{\beta}_1^2}{1 + (2\phi_3/c^2) - \vec{\beta}_3^2}\right]^{1/2} \left(\frac{1 - \vec{\beta}_3 \cdot \vec{\epsilon}_{23}}{1 - \vec{\beta}_2 \cdot \vec{\epsilon}_{23}}\right) \cdot \left(\frac{1 - \vec{\beta}_2 \cdot \vec{\epsilon}_{12}}{1 - \vec{\beta}_1 \cdot \vec{\epsilon}_{12}}\right) \quad . \tag{12}$$

Here we observe that the subscripts 1 and 3 refer to the ground station at the time of transmitting and receiving the signal. During this time (which equals 2r/c, where r is the path distance to the probe), the earth has rotated and β_2 has changed direction but not magnitude. The earth's gravity has not changed, so $\phi_1 = \phi_3$. The term in the first bracket thus cancels to 1, leaving only the first-order doppler expression in the two remaining brackets, which, if we approximate by putting $\vec{\beta}_1 = \vec{\beta}_3$ and $\vec{\epsilon}_{23} = -\vec{\epsilon}_{12}$, as expected, converges to twice the doppler frequency: $[1 + 2(\vec{\beta}_2 - \vec{\beta}_3) \cdot \vec{\epsilon}_{23}]$, given by $f'' - f_0$. [Note: This last approximation is given only to illustrate magnitudes and will not be applied in the following derivations.]

The system in Figure 9 combines the two downlink signals to obtain at mixer M3

$$\Delta f = (f_0' - f_0) - \frac{1}{2}(f_0'' - f_0) \quad ,$$

and

$$\frac{\Delta f}{f_0} = \frac{f_0}{f_0} - \frac{f_0'' + f_0}{2f_0} \quad . \tag{13}$$

Substituting equations (11) and (12) into equation (13) and setting $\phi_1 = \phi_3$ and $|\beta_1| = |\beta_3|$, we obtain, after considerable manipulation,

$$\frac{\Delta f}{f_0} = \left[\frac{\phi_2 - \phi_3}{c^2} - \frac{1}{2}(\beta_2^2 - \beta_3^2)\right] - \frac{1}{2}[\vec{\beta}_1 \cdot \vec{\epsilon}_{12} + \vec{\beta}_3 \cdot \vec{\epsilon}_{23} - \vec{\beta}_2 \cdot (\vec{\epsilon}_{12} + \vec{\epsilon}_{23})]$$
$$+ (\delta_p^2 - \delta_e\delta_p) - [(\delta_e^2 + \delta_p^2) - 2\delta_e\delta_p] \quad , \tag{14}$$

where, in the second-order terms, we define

$$\delta_e = \vec{\beta}_1 \cdot \vec{\epsilon}_{12} = -\vec{\beta}_3 \cdot \vec{\epsilon}_{23} \quad \text{and} \quad \delta_p = \vec{\beta}_2 \cdot \vec{\epsilon}_{12} = -\vec{\beta}_2 \cdot \vec{\epsilon}_{23} \quad .$$

This expression can be put in the following form, which we use to describe the relative motion between the earth and the probe:

$$\frac{\Delta f}{f} = \frac{\phi_p - \phi_e}{c^2} - \frac{|\vec{\beta}_2 - \vec{\beta}_1|^2}{2} - \frac{\Delta t}{2c}\vec{\epsilon}_{23} \cdot \vec{a}_3 \quad . \tag{15}$$

We note, however, that $\vec{\beta}_1$ and $\vec{\beta}_3$ are not the same, since the earth, whose angular rotation rate is Ω, has rotated an angle $\Omega\Delta t$, where Δt is the go-return time of the transponded signal. The direction of $\vec{\beta}_1$ has changed, and the corresponding acceleration representing this velocity change is the familiar centripetal acceleration $\vec{a}$ in the radial direction perpendicular to the earth's axis of rotation.

The last term in equation (15) expresses the fact that the earth moved during the light time Δt of the two-way signal and that the doppler cancellation system, which cannot react faster than the speed of light, must account for the change in velocity of the earth's rotation during the light time of the signal. This is an exact replica of the situation shown in Figure 4, which was used to illustrate the redshift. Here the acceleration is the result of the rotating earth and, assuming the coordinate frame we are using, would vanish in our experiment only if we chose to locate the tracking station at one of the earth's poles. The residual effect is the first-order doppler shift of a receiving station, whose velocity changes during the time $\Delta t/2$ (one-way owing to an acceleration $\vec{a}_3$). The component of this velocity change in the propagation direction is represented by the dot product $\vec{\epsilon}_{23} \cdot \vec{a}_3$, where $\vec{\epsilon}_{23}$ is the unit vector describing the direction of propagation from the probe to the earth station. Figure 13 shows the magnitude of this term as a function of time for a trajectory similar to the one actually flown.

The major relativistic effects are contained in the first two terms of equation (15). The first is the redshift effect we seek to test, while the second is the second-order doppler effect of special relativity due to the relative velocity of the earth and the probe oscillators. It is interesting to note that, because this experiment is essentially one involving a freely falling object, the contribution of the v^2/c^2 second-order doppler effect (where v is the velocity) is equal to the redshift. This can readily be seen if we consider the conversion of potential energy ϕ to kinetic energy over the trajectory between points A and B:

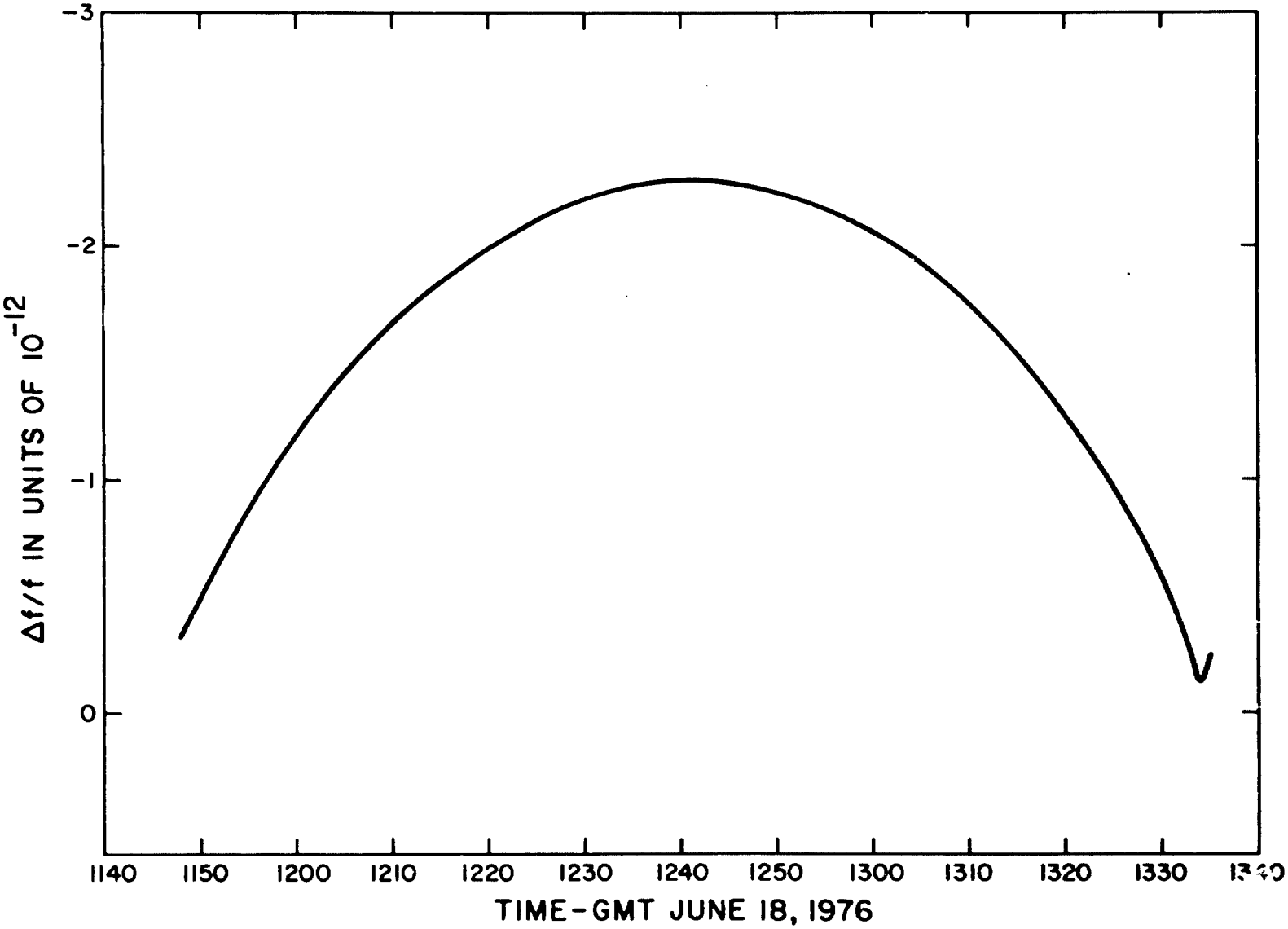

Figure 13. Effect of earth station motion during light time from probe.

$$\frac{1}{c^2}\int_A^B \phi = \frac{1}{2c^2}\left(v_B^2 - v_A^2\right) \quad . \tag{16}$$

This is a manifestation of the virial theorem of classical mechanics, where the total energy is equal to the average value of the kinetic energy.

The result of combining the redshift and the second-order doppler effects is shown in Figure 14, which are very nearly equal as a result of the free fall of the probe. We observe there the effect of the negative sign of the second-order doppler effect at the ends of the trajectory, where the relative velocity between the earth and the probe is greatest, and the effect in the positive direction near apogee, where the redshift term dominates.

The objective of this experiment is to see how $\Delta f/f$ varies with gravitational potential. We must therefore account for the second-order doppler and earth motion effects shown as the second and third term of equation (15) in addition to predicting the gravitational potential variation shown in the first term. Position, velocity, and direction information are required as a function of time at an accuracy commensurate with the clock stability. In addition to this we must know the gravitational potential including possible effects of lunar and solar gravity as a function of the probe's position.

Knowledge of the time dependence of the geopotential at the probe, along with position and velocity data, is used to generate a prediction of the right-hand side of equation (15). The comparison of the prediction with the actual data is, in fact, the test we are making.

The fact that the microwave signals traverse large distances over which substantial changes in gravity field occur means that this comparison of oscillators is a measurement of very nonlocal effects. Furthermore it relies on the assumption of the isotropy of the one-way velocity of light. To predict the behavior of the data from this rather complex system we will assume that the oscillators, electromagnetic signals, velocities, and gravitational fields are all interacting in the self-consistent manner described by General Relativity. In short, this experiment tests the internal self-consistency of these aspects of General Relativity.

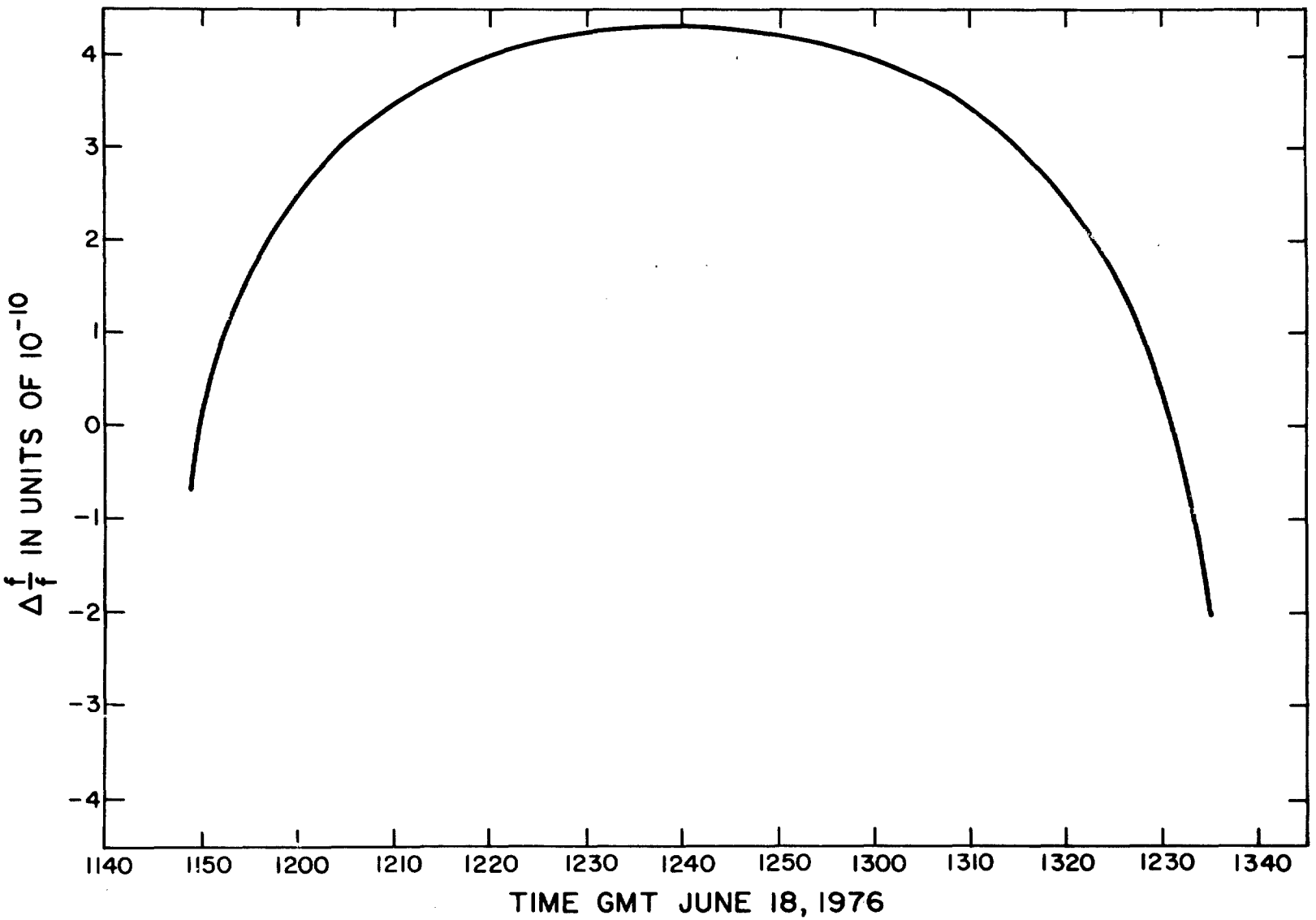

Figure 14. Combined redshift second-order doppler and earth motion effects.

8. PROBE TRACKING REQUIREMENTS

The experimental test of the gravitational redshift depends on our knowledge of all the terms in equation (15) at all points in the trajectory. The data-reduction process we use will compare the measured value of $\Delta f/f$ with the predicted value of $\Delta f/f$ obtained from our knowledge of the geopotential, the relative velocity, and the value of the component of the acceleration of the ground station due to the earth's rotation in the direction of the line of sight to the probe. We will presume that the second-order doppler and earth-acceleration terms of the special theory of relativity are, in principle, correct and will assign all the discrepancies in the data to the gravitational effect $(\phi_p - \phi_e)/c^2$.

In keeping with the constraints on accuracy set forth earlier we require that the overall error in the trajectory determination must be such that the error in the redshift prediction, including the second-order doppler and earth rotation terms of equation (15), is less than 1×10^{-14} in $\Delta f/f$. To achieve this, we set the error in the position determination, which, in turn, governs the gravitational potential prediction as follows:

$$\partial\left(\frac{\Delta f}{f}\right) = \partial\left(\frac{\Delta\phi}{c^2}\right)$$

$$\simeq \partial\left(\frac{GM}{c^2}\frac{1}{r}\right) = -\frac{GM}{c^2}\frac{\partial r}{r^2} \quad .$$

For an error contribution of $\pm 2 \times 10^{-15}$ near apogee (altitude 10,000 km) we must determine position in the radial direction within ± 100 m. For the same error near earth, the radial distance must be ± 16 m.

The error contribution from uncertainties in the second-order doppler are as follows:

$$\partial\left(\frac{\Delta f}{f}\right) = \partial\left(\frac{v^2}{2c^2}\right) = \frac{1}{c^2}\, 2v\, \partial v \quad .$$

For the same level of error taken as $\pm 2 \times 10^{-15}$ we must determine the velocity within 6 cm/sec near apogee and 1 cm/sec near earth. The uncertainty in the angular position of the centrifugal acceleration in relation to the propagation vector is consistent with the position requirements given above.

Under the above position and velocity restrictions on the tracking accuracy, the root-sum-square contribution of tracking-related parameters to the experiment's accuracy is about 3.5 parts in 10^{15}.

The question of position and velocity tracking accuracy is crucial to the accuracy of the mission. At the beginning of the program, two separate studies were made to ascertain the feasibility of the experiment in this regard (Townsend and Alford, 1972; Ryan, 1973). The recommendations were to use range-rate data exclusively and to take these data from at least three tracking stations equipped either with atomic hydrogen masers or improved cesium-beam frequency standards.

The USB system had four stations that can provide useful data; their station locations are as follows:

Station	Latitude	Longitude
1. Merritt Island, Florida	28°30'30"	279°18'24"
2. Bermuda	32 21 5	295 20 32
3. NTTF	38 59 55	283 9 25
4. Ascension Island	-7 57 17	345 40 23

Of these, stations 1, 2, and 3 were equipped with hydrogen masers; the masers at Bermuda and the National Test and Training Facility (NTTF) were built by the Goddard Space Flight Center (GSFC). The Merritt Island Launch and Acquisition (MILA) station was the primary data-acquisition site, recovering the relativity data with the system shown in Figure 9. Two SAO-constructed VLG-10A masers were located at MILA to serve several purposes: to provide redundancy in the event of failure, to furnish an internal self-checking capability throughout the actual mission, and to enable preflight simulation tests to be done before the mission.

Doppler tracking was done at Merritt Island using both the two-way and the one-way methods. The two-way doppler data were recovered by measuring the doppler beat frequency between the uplink and the translated down-link signals. The one-way doppler data, which also included the relativistic frequency shifts, were obtained by comparing the clock signal received from the probe with the station oscillator. At MILA both types of data were logged in terms of actual counts of doppler-frequency zero crossings taken over 0.2-sec intervals. The one-way data were taken at the even tenths of a second, the two-way at the odd tenths.

Doppler tracking at the other stations was done by logging three-way doppler cycles, the latter resulting from the behavior of the frequency of the signal that originates in the uplink transmitter at Merritt Island and is transponded to the several ground stations.

The operations plan allowed for a minimum of three stations in addition to Merritt Island to be ready at the time of launch; the Merritt Island, Bermuda, and NTTF stations were considered as the primary tracking stations, with Ascension Island serving as back-up statior Merritt Island had the additional responsibility of being the redshift data-acquisition station. All stations recovered telemetry data from the probe.

9. REDSHIFT DATA ACQUISITION

The primary redshift data from the last mixer shown schematically in Figure 9 were recorded in digital form by measuring the voltage of the sinusoidal signal at 14-bit accuracy (0.006%) every 0.01 sec. Output data in the form of both sine and cosine voltages were acquired so as to resolve ambiguity of phase reversal, which, as mentioned before, occurred at two points in the mission.

The instability that these discontinuous and granular measurements produced in the data are shown in Figure 15 and are well below the instabilities of the maser oscillators being compared. A redundant data-acquisition system operating completely independently of the primary system was also included at the MILA site to act as a backup in the event the primary data system malfunctioned. This system sampled the data at the same rate but at 12-bit granularity.

The MILA station data were acquired and placed into the 1-frame/sec format depicted in Figure 16. To relate the redshift beat-frequency data to the predicted redshift data with a maximum error of 2×10^{-15}, the time synchronization between the tracking stations and the MILA redshift data-acquisition station must be maintained within 10^{-4} sec. Since a synchronization accuracy at the 10^{-5}-sec level is routinely available to satisfy the tracking requirements; the experimental error contribution from this source is negligible.

Timing for the 0.01-sec interval between 14-bit samples of the redshift data is done by freezing the voltage in a sample-and-hold amplifier on command from the 100-pulse/sec signal obtained from the station clock, which is monitored from Loran C signals controlled by the United States Naval Observatory. These signals represent the UT1 time scale and provide the data required to determine the angular position of the rotating earth with respect to the usual astronomical coordinate axes. This information is necessary, since equation (15) is given in terms of the relative position of the earth and probe, and the probe trajectory, in terms of a coordinate system based on an earth-centered inertial frame. In representing the predicted values for equation (15), care must be taken to place the earth and the probe in the same coordinate.

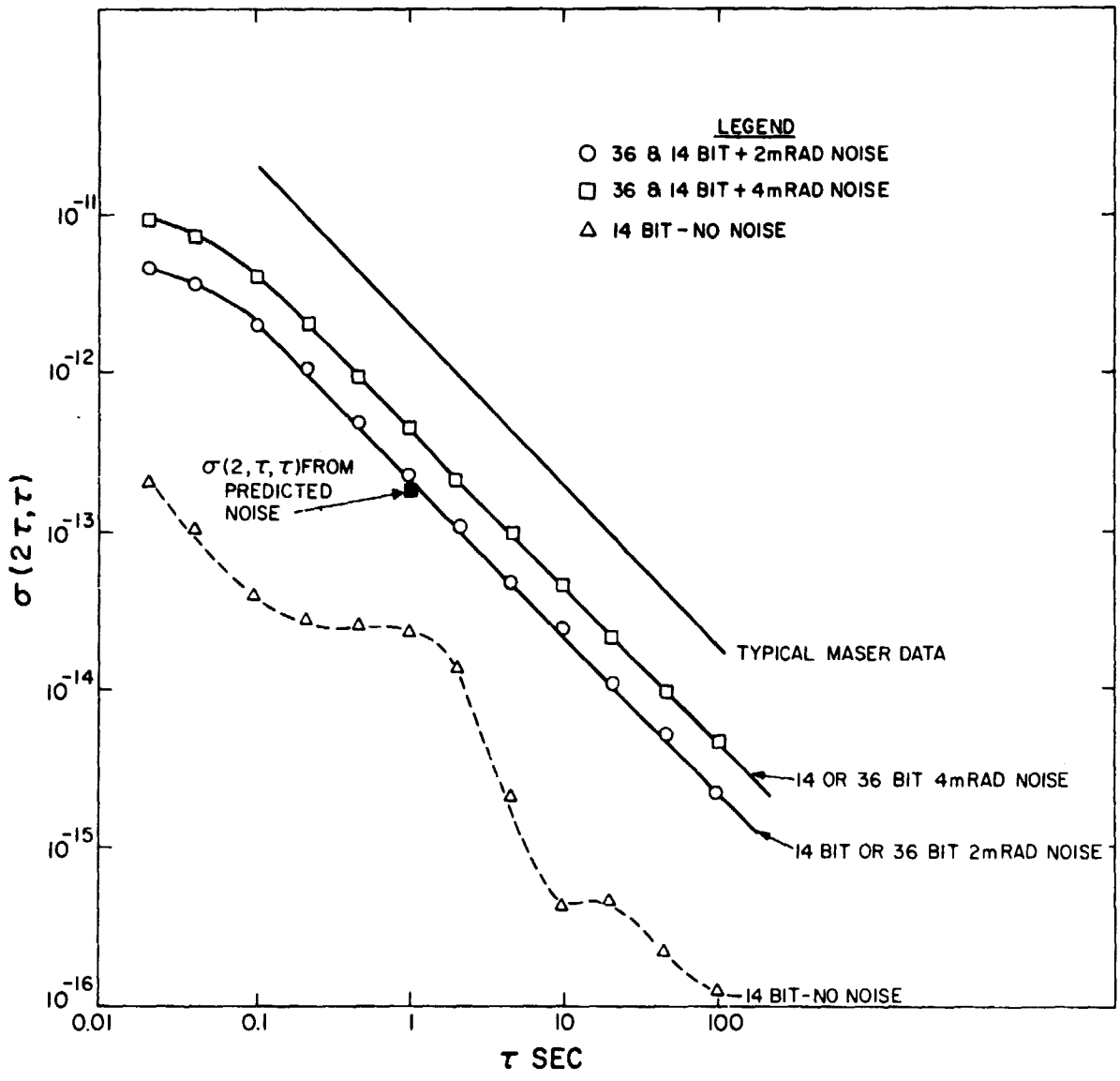

Figure 15. Noise from recording system expressed as Allan variances.

GPA EXPERIMENT

PROCESSED DATA OUTPUT TAPE RECORD FORMAT 1 SEC/RECORD ON
7-TRACK DIGITAL TAPE AT 556 BPI

RECORD HEADER

TOD	REC 1 & 2 AGC'S AND SPE'S AND EXCITER-1 SPE	TELEMETRY DATA	TEMP. IN	TEMP. OUT	BAR. PRESS	HUMID. OUT	SPARE

SIN_1^+	COS_1^+	$POS_1^{\neq}$	SAMPLE GROUP 2-9	SIN_{10}^+	COS_{10}^+	$POS_{10}^{\neq}$	STRIPPED TDP DATA	
			12-19					
			22-29					
			32-39					
			42-49					
			52-59					
			62-69					
			72-79					
			82-89					
SIN_{91}^+	COS_{91}^+	$POS_{91}^{\neq}$	92-99	SIN_{100}^+	COS_{100}^+	$POS_{100}^{\neq}$	STRIPPED TDP DATA	E.O.R.

Figure 16. Format for data acquisition.

10. THE DATA-REDUCTION METHOD FOR THE REDSHIFT EXPERIMENT

The actual behavior of the output frequency obtained from the doppler cancelling system is compared with the theory according to the flow plan shown in Figure 17. The left-hand arrows symbolize the three input data sources, which come from the format described earlier. These sources are 1) the sine and cosine output from the doppler cancellation system, 2) the probe trajectory as recovered from the doppler tracking data, and 3) the telemetry data describing the environmental conditions at the probe and the internal operating conditions in the probe maser, the transponder, and the translator.

The overall program predicts the behavior of the redshift beat signal from the trajectory by using the general theory of relativity as the working hypothesis. Further predictions relating to the previously calibrated phase and frequency sensitivities are added to the redshift prediction, including the fixed offset measured by direct comparison of the probe and ground masers. These data are expressed in terms of phase by integrating frequency data from an arbitrary epoch and encoding them magnetically to produce a data prediction tape. Because the trajectory information and phase correction data are relatively noise-free these data show little or no short-term variations.

The sine and cosine data, are left unfiltered so as to recover the noise and whatever rapid systematic effects resulted from the probe's rotation and nutration. Values of redshift beat data are recorded in terms of phase versus time, starting at the same arbitrary epoch that was chosen for the prediction tape. As before, these data are recorded on magnetic tape to provide a redshift data tape.

A 300-sec stretch of data centered at apogee is used to determine the fixed offset frequency of the probe maser that resulted from the trauma of launch. This fixed offset frequency is removed from the whole data set so that only the variation of the frequency from apogee is considered. In the results we find that the offset was very small, -3.1×10^{-13}.

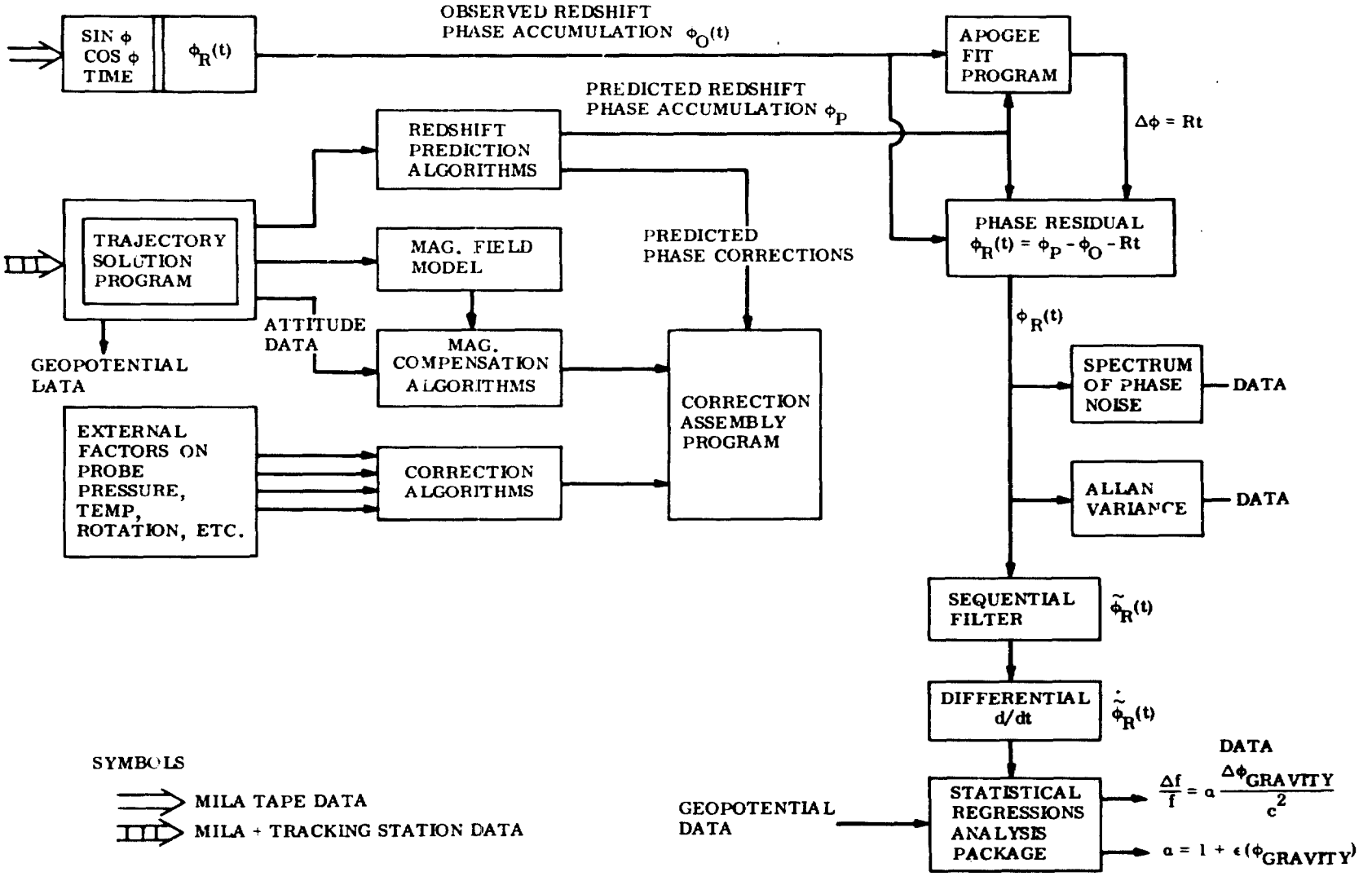

Figure 17. Data-reduction flow chart.

This offset information was intended for use in estimating the cavity frequency shift, which, if appreciable flux variation had occurred, would have caused systematic output frequency shifts. This correction was not required.

In the data-reduction process all comparisons of prediction with actual data are made in terms of phase, thus avoiding the problems that could result if we attempted to determine, as a function of time, the frequency information in the data by filtering and differentiating. Filtering and differentiating that is required is done only to represent the departure in the redshift data from the prediction for the statistical regression process, and since the frequency variations are small, no problems are anticipated.

The geopotential at apogee is taken as the zero potential for our comparison of the redshift, $\Delta\phi/c^2$, with $\Delta f/f$. In the data-flow diagram, the linear regression of the residual frequency, obtained by subtracting the prediction data from the redshift data versus $\Delta\phi/c^2$, should have a slope of zero if the equivalence principle holds. Since there are random noise processes as well as possible residuals, the data are represented statistically as a slope ϵ with a 1σ uncertainty in the slope, $\pm\delta$. Other frequency uncertainties resulting from the calibration and measurement errors determined during testing are computed along with the corrections applied to the prediction data; since they are uncorrelated, they are combined in a root-sum-square manner to represent the 1σ-accuracy capability of the experiment system and is designated as $\pm\iota$. The combination of $\pm\delta$ and $\pm\iota$, again as root sum squares, comprises the combined 1σ-accuracy capability of the experiment.

In the development of the experiment plan, the accuracy capability was discussed in terms of a predicted error budget, which was used as a guideline for allocating errors among the various components of the experiment that result from random effects and systematic uncertainties. In the final analysis of the data, the random or noise effects can be compared to $\pm\delta$ and the systematics with $\pm\iota$ to obtain an evaluation of the system performance.

Additional means are available to evaluate the data and extract further systematic and statistical information. The residual phase data are treated as a time series and

are processed to yield the Allan variance of the frequency comparison. This technique gives information about the spectral densities of the various noise components in the data, enabling us, to identify physical processes that can cause these disturbances. As shown in Figure 5, we see that the hydrogen-maser performance instabilities are caused chiefly by two processes: the behavior of the τ^{-1} slope from 0.01- to 100-sec averaging intervals and of the $\tau^{-1/2}$ slope for 100-sec averaging intervals and longer then an upturn resulting from systematic effects. These two slopes are characteristics of the additive white phase noise (τ^{-1}), the flicker-of-phase noise (τ^{-1}), and the white frequency noise ($\tau^{-1/2}$) contribution originating in the hydrogen maser.

11. THE SPACE PROBE MASER OSCILLATOR

Since the probe maser was specifically developed for the redshift probe experiment, and since its performance and our knowledge of its systematics under environmental stress are crucial to the outcome of the experiment, the construction of the maser is described here in some detail, together with a discussion of the major perturbing environmental effects. Section 14 contains further details on the actual calibration data used to correct the redshift data for systematic variations owing to the space environment.

From the data given for the ground-maser performance shown in Figure 5, we see that the contributions to errors from this source are on the order of 8×10^{-15} and 3×10^{-15} for 100-sec and 1000-sec averaging times and that, following the original precepts discussed in Section 4, the maser errors are taken as the chief limitation to accuracy. Since there has been no previous experience, we expect that the error contributions in the space maser will dominate. The identification of these errors and the removal of their systematics through tests and calibrations have constituted a significant portion of our effort in the program. These tests and calibrations were performed as part of the qualification test program for the actual flight hardware. This is the "protoflight" concept under which the program was governed.

It is clear that there is a dilemna inherent to this concept. How far should a new device be tested to gain assurance of its mechanical, vacuum, and structural integrity without its flight-worthiness being lost? Many questions of this type were answered by testing an earlier engineering model of the flight maser, which was designated as the engineering verification unit (EVU).

The list of tests of the EVU and the later tests of the flight article will not be spelled out here. Detailed procedures for all these tests are on record. Many of the tests were substantially complicated by the requirement for accurate simulation of launch conditions for calibration purposes. Also, simulations of vehicle spinup and magnetic profiles during thermal-vacuum tests because of magnetic hysteresis effects had to be made in the proper sequence.

However, it must be emphasized that the success of the experiment resulted almost entirely from this massive test program, which served simultaneously both to qualify the probe maser and the other probe components and to calibrate the systematic variations of phase (or frequency) resulting from environmental variations from launch to the end of the mission.

In addition to all the scheduled aspects of the test program, many unexpected problems arose, which had to be solved by making engineering changes, often on the spot, without perturbing the planned test schedule. It is clear that engineering development tests were frequently being made coincidentally with the qualification and calibration tests. Required for all this was substantial flexibility in the test philosophy as well as good engineering practice. During this testing phase the problems that arose were solved in such a manner that the validity of a qualification result or a parameter for a calibration was not compromised by a subsequent engineering modification. Under the leadership of the MSFC program manager, the SAO and MSFC science, engineering, and test groups worked very effectively together to overcome many problems that often seemed impossible to solve within the schedule leading to the launch.

11.1 Probe-Maser Design Requirements

From the dynamics of a body falling nearly vertically in the gravity field of the earth and from the known behavior of atomic hydrogen masers, we can establish a very rough optimum situation, based on the following considerations:

1. Allow enough time aloft to stabilize whatever launch-induced perturbations occur and minimize the effect of such thermal and mechanical perturbations so that the maximum possible stable operating time is available.

2. Maintain communication between the payload and the ground station throughout the mission; concentrate on obtaining data from apogee down to altitudes as low as possible at the end of the mission.

Owing to the R^{-1} gravity potential acting on a freely falling body, the time available for measurements near impact is a relatively insensitive function of the time aloft,

and the strategy therefore is to obtain a minimum period of about 2 hours, in which apogee redshift values greater than 4 parts in 10^{10} are attained. The upward branch of the trajectory would also contain some data; however, because of the propulsion phase and payload stabilizing time, these data will be of less value than the data from the later, downward branch.

Obviously, no time is available for the more conventional spacecraft outgassing and thermal stabilizing. Furthermore, since this is a one-shot mission, both the space and the ground equipment must operate without interruption and with the required stability throughout the mission. A very stable operating condition before launch and thermal and mechanical stability through the experiment are necessary. This plus the weight limitations resulting from the vehicle constraints placed rather stringent design requirements on the experiment.

The first requirement is that of survival through the vibration, shock, acoustical pressures, and decompression of launch by the four-stage, solid-fueled Scout system into a zero g and spinning condition while in space. Of the total payload equipment, the hydrogen maser and the newly designed ammonia cooling system for the transponder are the only types of items that had not previously been flown in space.

At the outset, we allowed about 90 lb for the maser and adhered as closely as possible to this limit. The requirements for its survival and operation in space were as follows:

1. The maser-frequency fixed-frequency offset resulting from the trauma of launch should be small, less than 5 parts in 10^{12}, stabilizing within about 10 min to an overall stability of 1 part in 10^{14} for the remainder of the mission.

2. Thermal, zero g, spin, and pressure effects from the transition into space causing possible longer term instability must be less than 1×10^{-14} either by calibrating for various environmental factors during preflight simulation tests or by engineering the maser to cope with its immediate environment at this level of stability.

3. The maser should be built so as to operate continuously for about 9 months to allow time for its qualification testing and calibration and to permit it to operate, without alteration, as a piece of flight hardware; this includes several weeks of preflight stabilization.

11.2 Maser Frequency Perturbations

The principal systematic frequency variation of hydrogen masers is described by the following expression:

$$\frac{\Delta f}{f} = \frac{1}{f}\left[\frac{Q_c}{Q_\ell}(f_c - f_0) + 2750\ B^2\right] \quad . \tag{17}$$

The first term is the cavity-resonance mistuning, or "pulling," effect, and the second is the second-order magnetic-field dependence of the atomic hydrogen hyperfine transition $F = 1,\ M_F = 0 \rightarrow F = 0,\ M_F = 0$. Q_c is the cavity resonator Q, and Q_ℓ is the Q of the atomic transition, which depends on the geometry of the hydrogen-maser storage bulb, the quality of the wall coating, and the collision rate of the atoms among themselves (spin-exchange processes). This last process is a function of beam input flux, which, in turn, can be represented in terms of the maser output power level.

Two aspects of the cavity-resonance shift especially concern us: 1) the variation in Δf_c during the mission, and 2) the average magnitude of Δf_c as a result of the combination of shake, shock, and zero gravity that occurs from earth-bound conditions through to the free-fall condition after powered flight ceases. The effect of cavity-resonance variations is obvious in equation (17). However, if there is also a large fixed offset $(f_c - f_0)$, we are further subject to output frequency variations due to variations in Q_ℓ resulting from changes in atomic hydrogen flux during the mission. These changes in flux result in changes in power level W, and the measured power level is used as a measure of the beam flux for calibration.

In the probe maser, the cavity-resonance frequency is subject to many changes – from stress changes resulting from variations in the gas pressure P of the enclosure surrounding the cavity vacuum system, from thermal expansion or contraction resulting from changes in temperature T, owing to centrifugal forces resulting from variations in the payload spin, and from changes in the cavity shape.

The expression describing all the known perturbations to the output frequency of the maser is

$$\frac{df}{f} = \frac{1}{f}\left[\frac{Q_c}{Q_\ell}\left(\frac{\partial f_c}{\partial P}\,dP + \frac{\partial f_c}{\partial T}\,dT + \frac{\partial f_c}{\partial \Omega}\,d\Omega\right) + Q_c \Delta f_c \frac{\partial (1/Q)}{\partial W}\,dW + \frac{\partial f}{\partial B_0}\,dB_0\right] \quad . \quad (18)$$

In the magnetic calibration of the maser we observed that there was very little correlation between the second-order magnetic field sensitivity of the atomic hydrogen hyperfine separation predicted from the expression $\Delta f_m \quad 2750\ H^2$ and the measured output frequency shift. At first we attributed this anomaly to the cavity microwave isolator, which, being a ferrite device operating in a magnetic field carefully adjusted to provide the proper resonance despite being shielded, was though to be affected by external fields. Subsequent developments and research on hydrogen masers disclosed that the effect was the result of changes in the state distribution of atoms among the hyperfine magnetic sublevels while in transit from the hexapole magnet to the bulb.

Changes in population among the atomic hyperfine sublevels produce changes in the output frequency of the maser as a result of interatomic spin-exchange collision processes during the storage lifetime of the atoms in the bulbs. Our solution to this problem was not only to calibrate the magnetic sensitivity but to simulate the whole magnetic history from prelaunch erection of the Scout rocket on through launch, spin up, and during the mission.

The magnetic field behavior was measured by simulating the magnetic history of the payload before launch, during launch, and throughout the flight. A standard initial-condition state magnetization of the magnetic shields was ensured by a pregaussing operation performed before the vehicle-erection phase of both the actual flight and the magnetic simulation of the flight. We had previously obtained the magnetic conditions from a survey of the launch area and from measurements at the position of the maser in the launcher while the launcher was being erected. The fields during liftoff and into the trajectory were obtained from earth field models, and the effect of the spinup of the probe at the appropriate earth field was incorporated in the simulation. The simulation of the rapid ascent into the vacuum of space was also included at the appropriate time in the sequence.

The magnetic field encountered during the flight has been determined from standard earth models. We found that, only the axial component appears to be important. The algorithm developed for the magnetic influence on the probe output frequency has two branches owing to hysteresis effects in the magnetic shields. The following algorithm was developed in the magnetic calibrations:

$$\frac{\Delta f}{f} = -5.8992 \times 10^{-13} B_{axial} \text{ ascending} \quad ,$$

$$\frac{\Delta f}{f} = -12.7213 \times 10^{-13} B_{axial} \text{ descending} \quad . \tag{19}$$

The sign convention is that the plus direction of field enters the earth at its north magnetic pole.

The effect of temperature variations within the maser causing cavity frequency shifts was measured via telemetry in terms of the aft-oven heater voltage. The frequency variation due to this effect was determined during tests. The following relationship for frequency versus aft-oven heater voltage was found:

$$\frac{\Delta f}{f} = -3.60 \times 10^{-14} \Delta V \quad . \tag{20}$$

The effect of pressure variations measured in the dome enclosing the forward assembly of the maser containing the cavity resonator was determined by calibration to be as follows:

$$\frac{\Delta f}{f} = -2.26 \times 10^{-12} \Delta P \text{ (decreasing pressure)} \quad ,$$

$$\frac{\Delta f}{f} = -3.11 \times 10^{-12} \Delta P \text{ (increasing pressure)} \quad , \tag{21}$$

where ΔP is in psi. The pressure was measured by telemetry.

The effect of spin-rate variations on the output frequency of the maser was measured:

$$\frac{\Delta f}{f} = (0.1906 \times 10^{-14}) \Omega - (7.554 \times 10^{-17}) \Omega^2 \quad , \tag{22}$$

where Ω is in rpm. An optical device on the payload provided rotation-rate data through the telemetry system.

12. EXPERIMENT OPERATIONS

The final payload weight was 225.49 lb. On May 3, 1976, SAO received an updated trajectory prediction from the Vought Corporation for a payload weight of 226.1 lb. Table 1 illustrates the as-flown performance with respect to the 226.1-lb trajectory prediction of May 3 and with the preflight predictions made from an updated weight estimate of 225.49 lb.

Table 1. Flight performance.

Parameter	May 3, 1976 prediction (226.1 lb)	Preflight prediction (225.49 lb)	Flight results (225.49 lb)
Impact of spacecraft			
Latitude, geodetic	24°.5909 N	27°.5544 N	29°.3027 N
Longitude	50°.5860 N	48°.7257 W	47°.4568 N
Time after liftoff (sec)	7090.7	7042.83	7002.98
Experiment time (sec) (time to x° tracking elevation minus 366 sec)	7°.6, 6584 sec 0°.7, 6634 sec		7°.9, 6480 sec 0°.4, 6540 sec
Apogee geocentric radius	1.6752×10^4 km	1.6684×10^4	1.66242×10^4 km
Apogee time after liftoff (sec)	3610.87	3586.84	3567.21
Redshift at apogee	4.306×10^{-10}	4.295×10^{-10}	4.285×10^{-10}

The trajectory, apogee altitude, and experiment time were remarkably close to the preflight predictions, and the vehicle performance was completely satisfactory.

The data-acquisition system at Merritt Island recorded the beat frequency in terms of sine and cosine voltages at 14-bit accuracy every 0.01 sec. The beat data were also acquired for "quick-look" purposes by a strip-chart recorder, some features of which are reproduced in Figures 18 through 23.

Figure 18 shows the acquisition of the payload signal while the payload was still attached to the fourth stage during the third-stage powered phase of the flight. The probe was not rotating, and the signals were being communicated through three parasitic antennas located on the skin of the vehicle and connected to the on-axis antenna of the payload by a coupler, which was later disconnected when the payload separated from the fourth stage. After third-stage burnout, we can see in the figure the effect of the spinup of the payload and fourth stage (while still attached to the third stage) before fourth-stage ignition. The phase of the beat signal was broken up because of the motion of the three separate antennas as the vehicle rotated.

Figure 19 depicts the end of this broken pattern when the payload separated from the burned-out fourth stage, exposing the dipole antenna. By having located the antenna on the spin axis and having made the probe's exterior surface rotationally symmetrical, very little variation of phase with rotation was observed. This figure represents the beginning of the useful data. Note that the beat frequency was slowing down (time goes to the right, with two major divisions equal to 1 sec).

About 5 min later, the beat signal went through zero, as shown in Figure 20. Here we see that the beat has gone from a negative frequency to zero and has reversed in sign. At this time, the aspect angle of the on-axis dipole probe antenna as seen from the ground was very nearly zero, close to the null of the antenna. The slight misalignment of the probe's rotation axis with respect to the dipole electrical axis, which occurred at payload separation, caused a small but observable modulation of the signal amplitude as the probe rotated. Incidental amplitude-to-phase conversion, present in all electronic systems, produced the observed phase modulation. Both the rotation rate and a modulation of the nutation rate are visible in the trace. These rates agree well with those predicted from our measurements both of the moments of inertia and of the impulsive torques available from the spinup thrusters. The spin rate also agrees with data from an optical spin sensor.

Figure 21 shows the beats as they continued near apogee about an hour later, and in Figure 22, the beat signal is seen going to zero and reversing in sign during payload descent. No antenna modulation is visible in Figure 22; nutational motion, as expected, had damped out by this time.

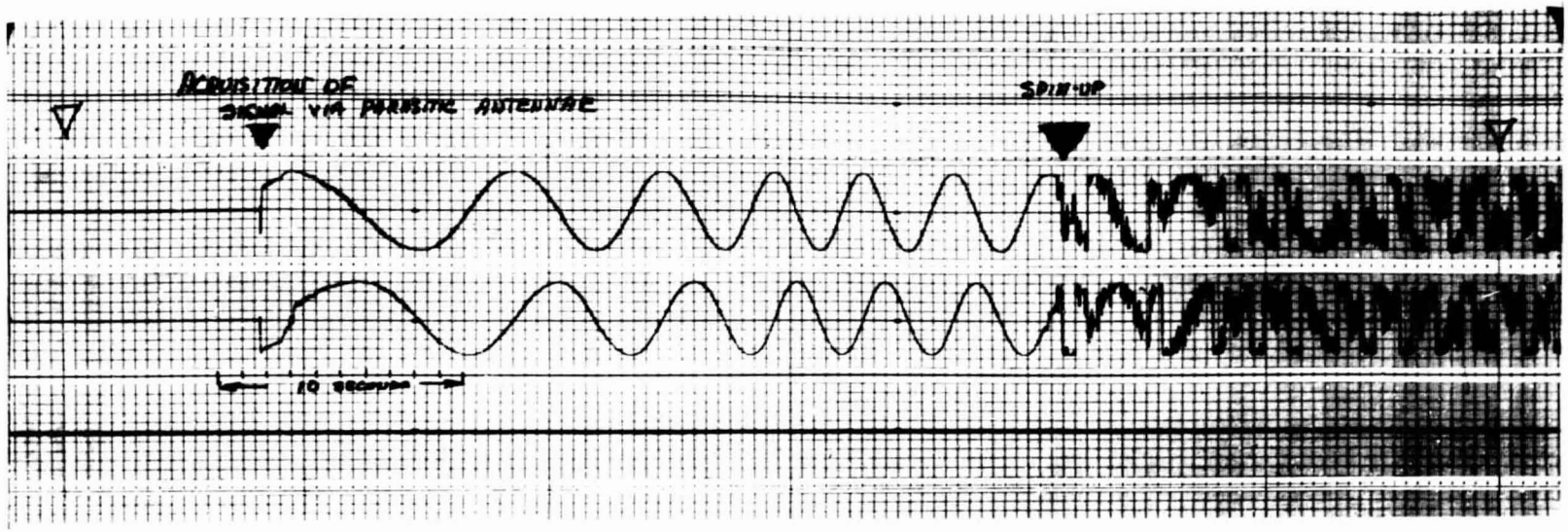

Figure 18. Sine cosine chart of relativistic effects: Acquisition of signal to spin up of 4th stage.

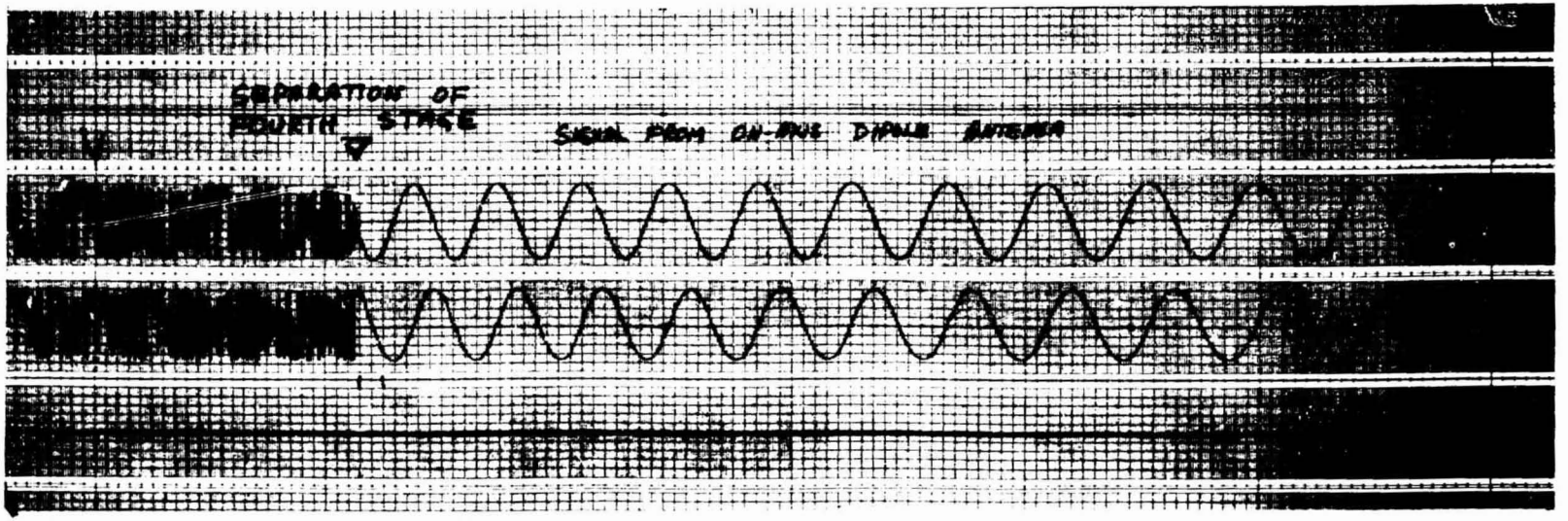

Figure 19. Sine cosine chart of relativistic effects: 4th stage separation.

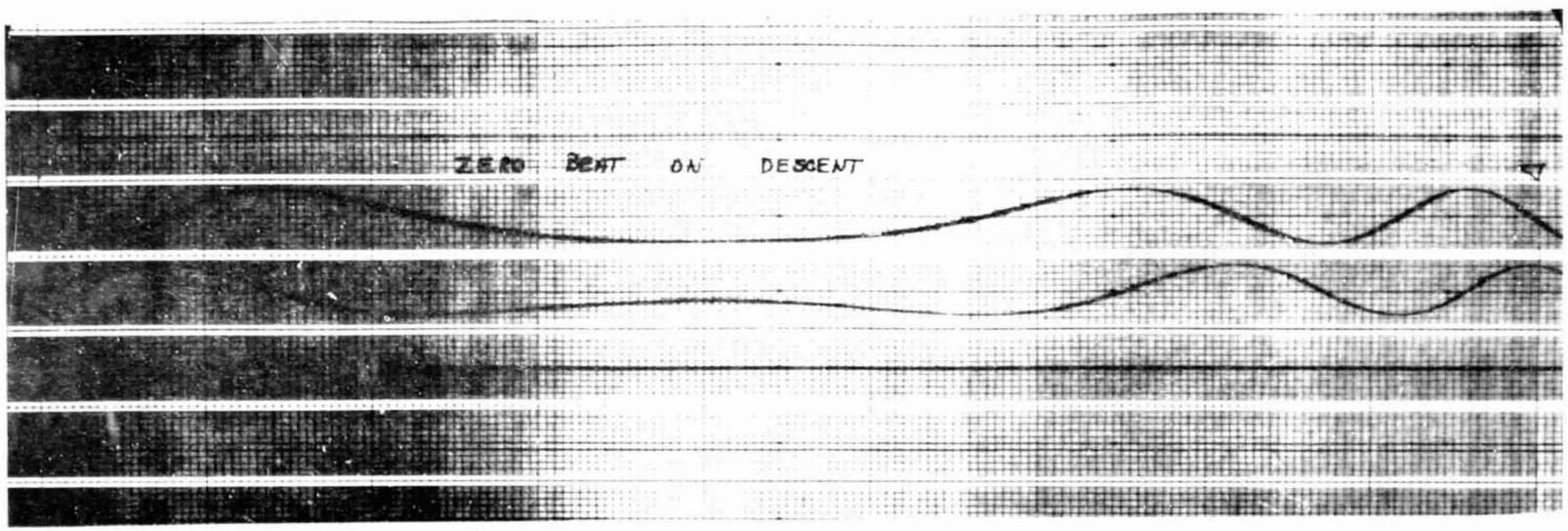

Figure 20. Sine cosine chart of relativistic effects: Zero heat on ascent.

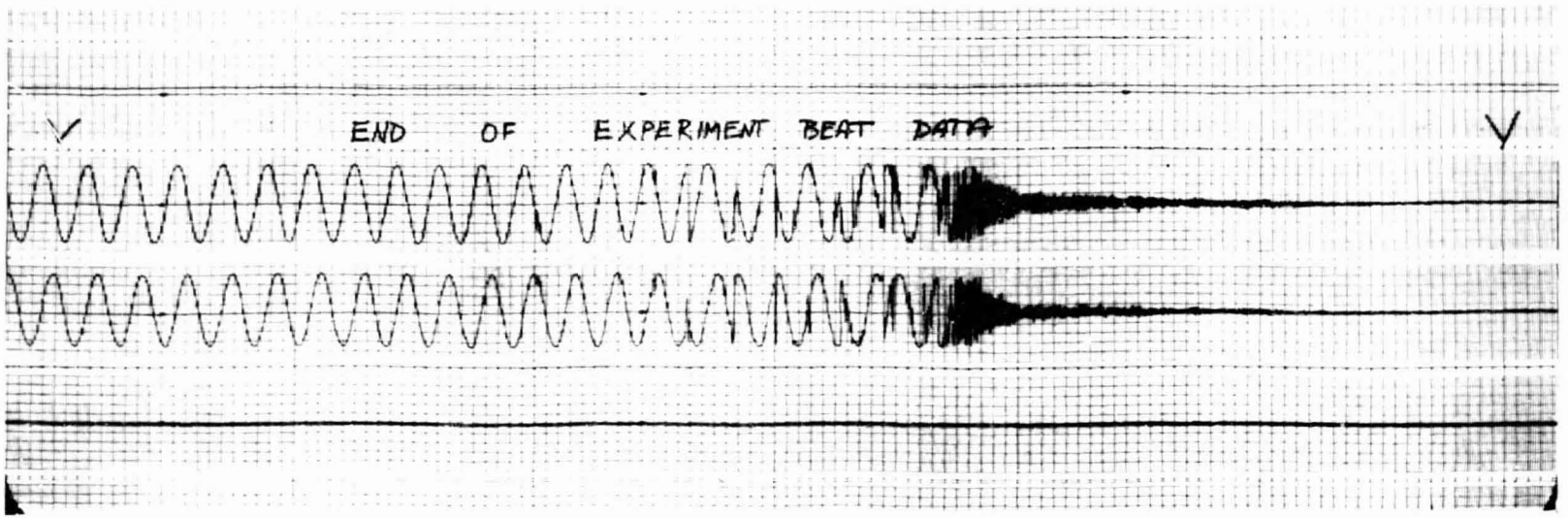

Figure 21. Sine cosine chart of relativistic effects: Beats near apogee.

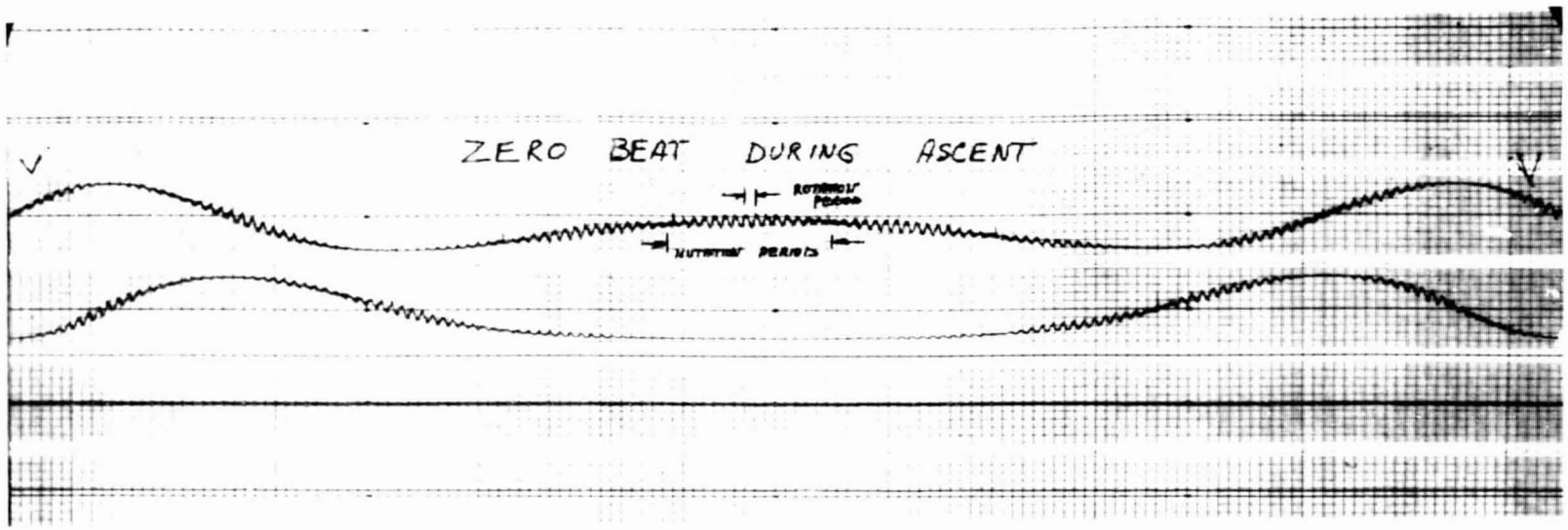

Figure 22. Sine cosine chart of relativistic effects: Zero beat on descent.

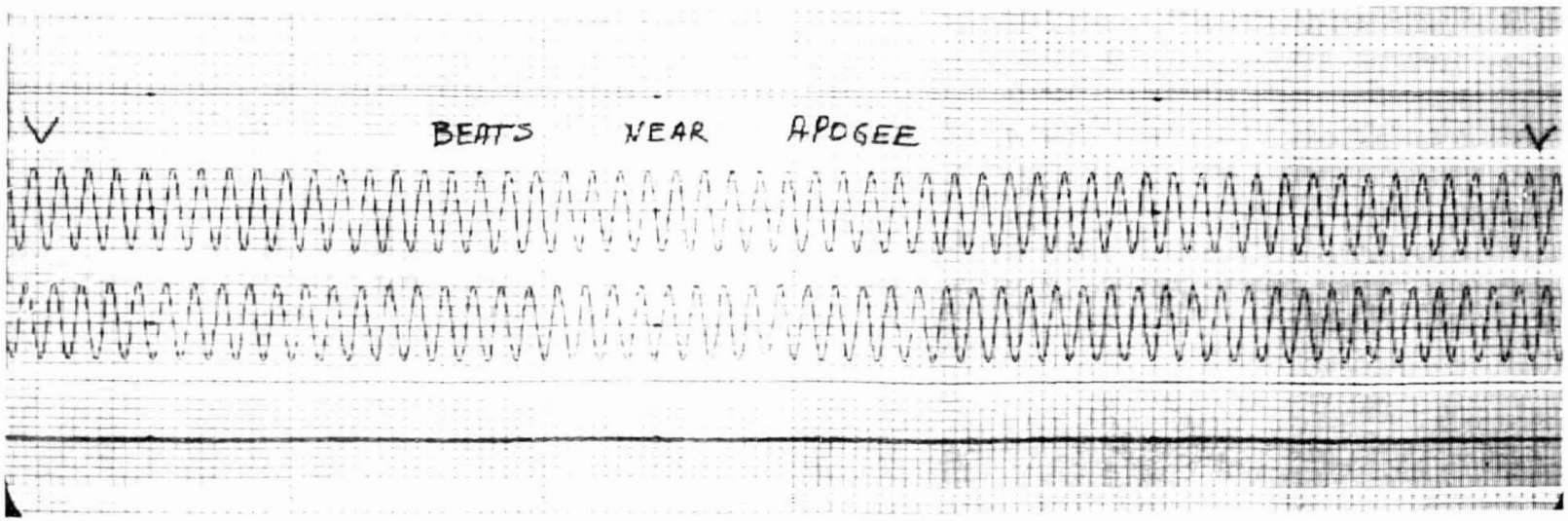

Figure 23. Sine cosine chart of relativistic effects: End of experiment.

The frequency continued to increase as the probe approached the earth, and we see the end of the experiment data in Figure 23. The apparent loss of phase coherence at about 12 sec before complete loss of signal is probably due to multipath propagation at low elevation angles. According to the existing trajectory, the phase apparently suffered no loss of continuity down to an elevation angle of 0.4°.

A time line of the significant events during the mission is shown in Table 2.

During the mission, we experienced only one loss of phase coherence, which resulted from a circuit-breaker dropout in the power supply for the uplink transmitter at the Merritt Island station. While this problem was quickly solved and only $1^m 8^s$ elapsed before the probe signals were reacquired, the phase stability of the system suffered severely and the data acquired after the dropout are still not understood well enough to be included in the results of this experiment. This problem was further complicated by the earlier than anticipated depletion of the liquid ammonia used to control the temperature of transponder-translator electronics. After the flight careful simulations were made on a similar set of electronics following the same time-temperature profiles and only very small phase variations were observed.

A rough approximation of the shape of the beat frequency versus time is given in Figure 24, which is plotted from quick-look frequency measurements.

Table 2. Significant mission events.

Event	Time (GMT)	Unexpected events	
Liftoff	11:41:00.24		
First-stage burnout			
First-stage separation			
First-stage heat shield ejected			
Second-stage ignition			
Second-stage burnout			
Second-stage separation			
Signal acquired at MILA and locked in	11:43:09.06		
Third-stage ignition			
Third-stage burnout			
Third-stage spinup start	11:44		
Third-stage spinup end			
Third-stage separation			
Fourth-stage ignition			
Fourth-stage burnout			
Payload separation	11:46		
Zero beat in redshift data on ascending branch	11:49	Payload rotation rate increased	
Bandwidth changed from 1.5 to 0.5 mHz	12:03		
Apogee	12:40:27		
	13:18	NH_3 ran out	
	13:22:47.63	Loss of lock; MILA failure	
	13:23:55.93	Signal reacquired	
	13:24:50.86	MILA exciter relocked to ground maser; all lock loops closed	Payload rotation rate constant
Zero beat in redshift data on descending branch	13:31		
First phase discontinuity; MILA elevation angle 0.4°	13:36:00		

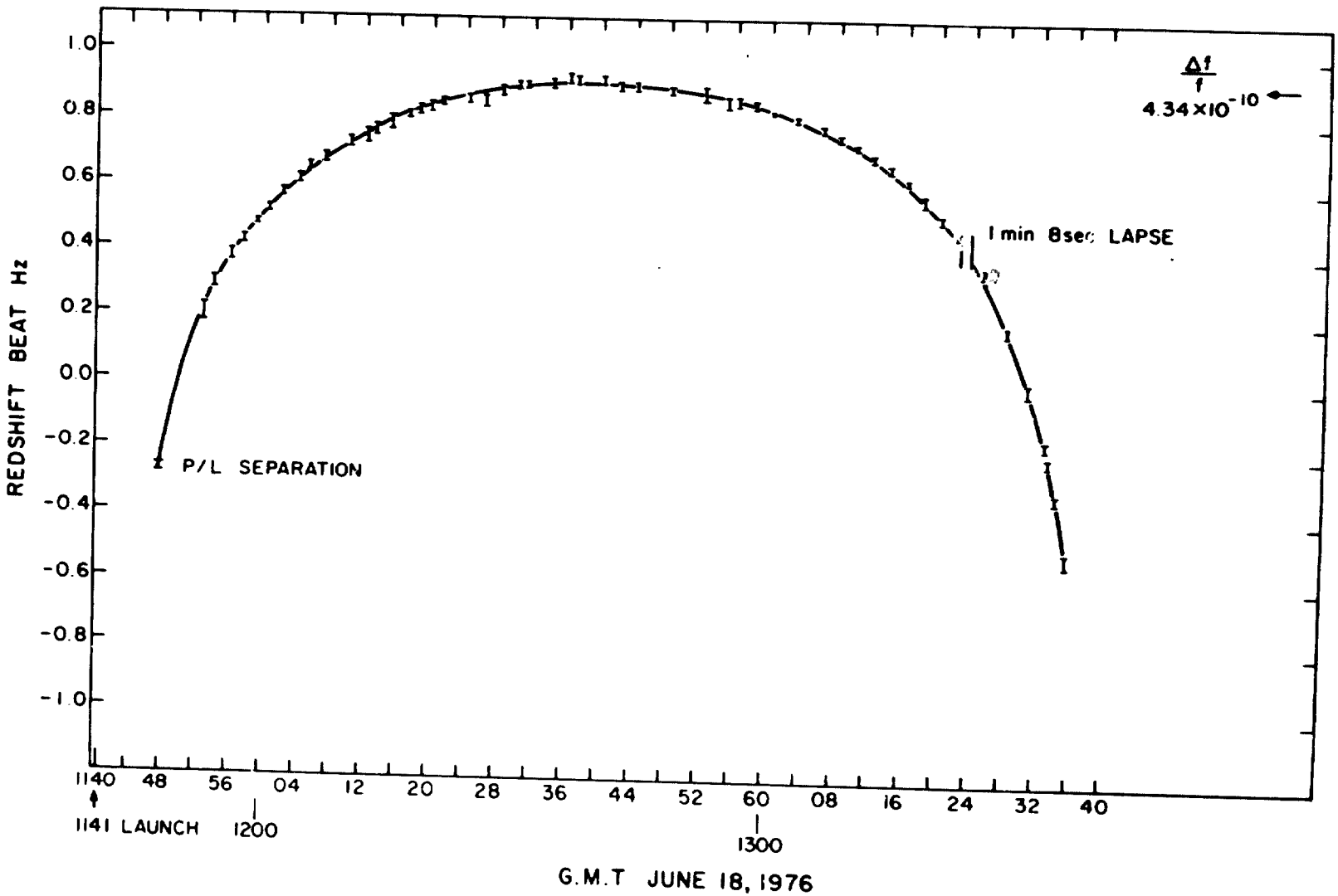

Figure 24. Redshift beat data from quick-look high-speed printer.

13. TRACKING DATA AND TRAJECTORY SOLUTIONS

Tracking data were obtained in the form of doppler cycle counts at Bermuda (BDA), NTTF (Goddard Space Flight Center, Greenbelt, Maryland), Ascension Island, and Merritt Island (MILA), Florida. All stations obtained data in the form of measurements of cycles of phase resulting from the change in signal path from Merritt Island, to the probe and back to the station. In the case of Merritt Island, which received its own uplink transmissions from the probe transponder, the doppler data represent twice the range rate of the probe and are represented as the cycles shown at mixer M1 of Figure 8. These data were encoded in the format shown in Figure 16 every 0.2 sec on the odd numbered tenths of the second and are interleaved between the data taken from mixer M2, which are recorded at even tenths. The other stations recorded doppler and telemetry data in the same format, however they did not take one-way data from the probe; the three-way data were encoded every 0.1 sec.

Our plan was to use NASA's normal data reduction procedure to process the doppler data from all stations by fitting them to a ballistic model of the trajectory. This procedure evaluates the fit and adjusts the initial conditions of position and velocity (state vector) to obtain an optimum fit to the ballistic model. Corrections for tropospheric and ionospheric effects, light-time delay (retardation), residual drag from the earth's troposphere, and light pressure are included in the ballistic model. During the process of reducing the telemetry data to convert them to useful measurements, we observed that the rotation rate of the probe changed significantly during the mission and that this angular acceleration stopped at a time coinciding with the depletion of the ammonia boiler. Careful research of the question of how the ammonia was vented from the probe led us to believe that the vent nozzle may have slightly misdirected the plume of spent ammonia and that a small residual thrust existed that caused angular acceleration of the probe. The existence of a component of thrust was present along the probe's spin axis caused a great deal of difficulty in the solution of the probe's trajectory from the doppler data. The fact that the uplink tracking signal was interrupted was also a hindrance to obtaining a clear-cut solution using standard techniques.

With the usual 20-20 hindsight we now see clearly that a few stretches of data from the standard USB range measurement system would have provided extremely valuable bench marks of position to verify the solutions obtained by fitting doppler data to a dynamical model.

The first attempts at trajectory solutions by the Goddard Space Flight Center showed that some nongravitational forces were at work on the payload and gave some insights to the possible problems to be encountered in modelling these forces to obtain an accurate trajectory using the dynamical methods. A close study of the suspected thrust from the ammonia boiler observed in the angular acceleration of the payload gave a time profile of the tangential component. Assuming that the nozzle configuration remained constant during the ammonia boil off we can infer from this time profile what the time profile will be for the axial component. The axial component will alter the course of the normally ballistic trajectory the radial component is averaged out owing to the 115 rpm (approx.) rotation rate.

This complication led to a reassessment of the problem and further dynamical solution methods were attempted at GSFC. Concurrently with these efforts, a non-dynamical method was developed at SAO, which amounted to a strictly geometrical intersection of three spheres whose radii were measured in terms of the doppler cycle wavelengths counted at the MILA, BDA, and NTTF stations.

This method of solution is not original and has been long used for tracking vehicles under powered flight. Its application depends on establishing a point of departure, or some known position during the flight at a known time. This is used to determine the number of doppler cycle counts at each of the three stations simultaneously with the time of the known position. Here, as mentioned earlier, the use of the USB range determining capability would have been very valuable. Fortunately we have data from a fourth tracking station at Ascension Island, which we used as a constraint on the choice of starting coordinates for the geometrical solution.

By observing the time behavior of the predicted minus the observed residual doppler cycle counts from the Ascension station as a function of starting position variations in each of three directions, we look for the starting position that gives a zero time slope to

this residual. Except for the uplink interruption, the cycle counts are continuous with very little jitter. The Ascension residuals give a very distinct and different time signature when the originating point is varied 500 meters in each direction. These three signatures, when expressed in terms of a cubic equation, supply us with a series of polynomial coefficients for each Δx, Δy, Δz from a standard starting point. We can then determine the optimum values of Δx, Δy, and Δz that make the residual signature closest to a straight line with zero slope.

The observations from Ascension were very limited however, and the probe never exceeded 6° elevation angle, which led to a problem of effects of tropospheric and ionospheric refraction and the question arose regarding how much of the data could be considered reliable in steering the starting point. Certainly near apogee, when there was little change of elevation angle with time, these effects would be minimum, however the extent to which Ascension data before and after apogee could be used was an open question. Test solutions were made using varying intervals of data centered at apogee and the behavior and the stationarity of the coordinates of the starting point was determined as a function of interval. Using this method, the estimated uncertainty in the coordinates put the starting point within a box approximately 40 meters on a side.

A third solution of the trajectory was made by Dr. J.D. Anderson and Mr. A. Liu of JPL using the dynamic approach with an axial force parameter modelled on the rotational information. This solution emphasized the fitting of the data taken after the ammonia was depleted where no thrust was expected and solved for the magnitude of the axial thrust coefficient. The standard deviation of the orbital parameters when transformed into speed and radial distance by simple conic equations gives a maximum radial error of 12 meters occurring near the end of the flight and a velocity error of 0.04 cm/sec. The magnitude of the thrust was found to be about 163 dynes and did not deviate in direction more than 5° initial velocity vector. The final analysis showed the S-Band phase residuals to be less than 0.8 cycles and the maximum doppler error was 0.5×10^{-3} Hz. A more complete account of this solution is given in Appendix I. The ground track of the trajectory is shown in Figure 25.

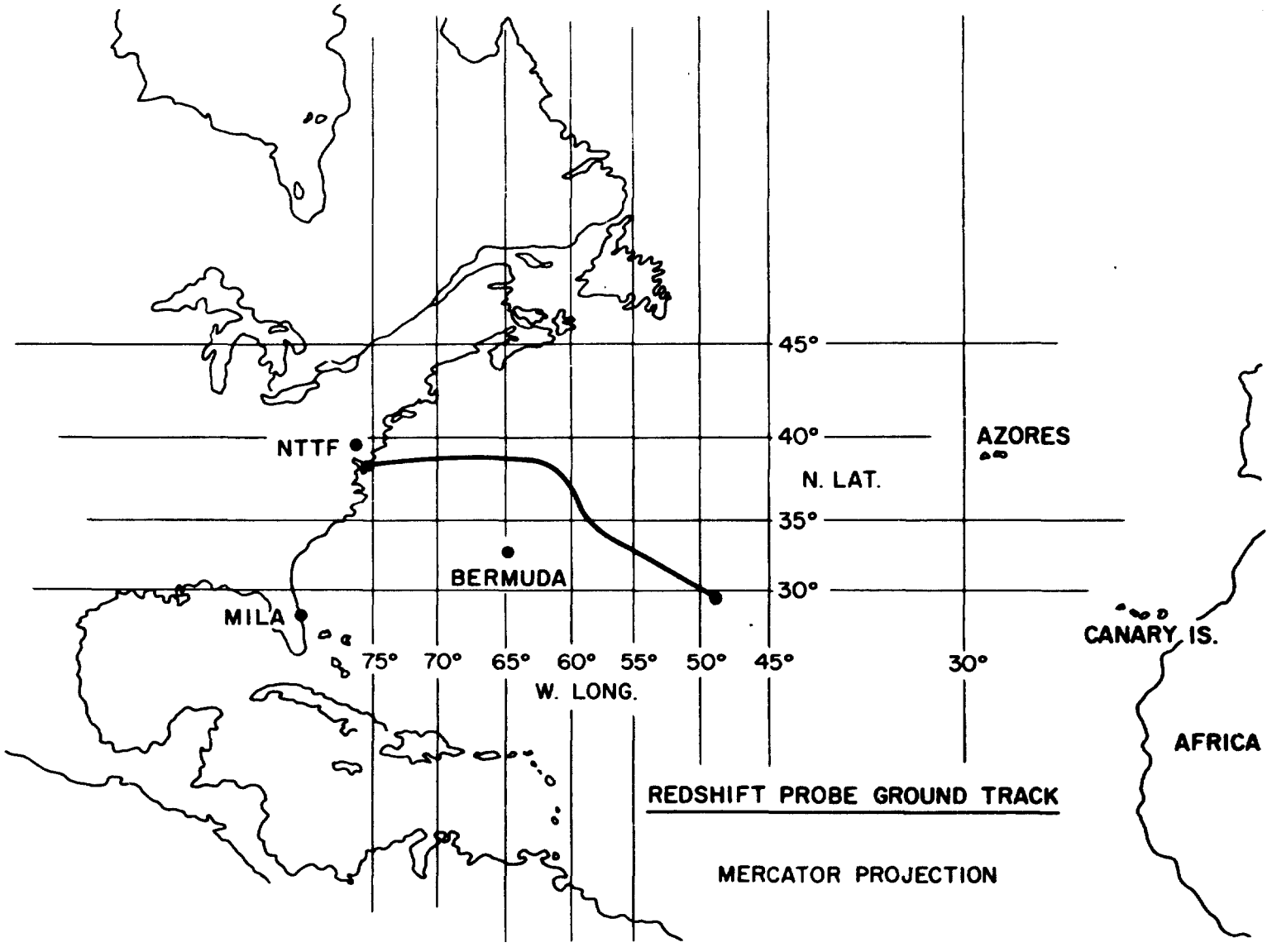

Figure 25. Redshift probe ground track.

This carefully developed solution from JPL finally resolved the nagging questions that had long delayed our ability to reach acceptable conclusions about the experiment. Table 3 shows for the JPL, SAO and GSFC solutions the magnitudes of the position and velocity differences from mean values established at times 1215, 1240 and 1322 GMT.

We conclude that the combined error of the position and velocity uncertainties across the interval 1215 to 1322 is on the order of $\pm 3.33 \times 10^{-15}$ when expressed in terms of $\Delta f/f$ given in equation (15).

The predicted phase accumulation for f = 2117.7 Hz using equation 15 is shown in Figure 26.

Table 3. Effect of differences between JPL, SAO, and GSFC trajectory solutions on redshift prediction. Comparison are shown at 1215, 1240 (apogee) and 1322 in terms of differences from average altitude and velocity.

Time	Average Radius from Earth Center, $\bar{r}$	$\delta\left(\frac{\Delta\phi}{c^2}\right)$ from average
1215	($\bar{r}$ = 14,972,895.88 m)	
	$r_{JPL} - \bar{r} = -79.2$ m	$+1.58 \times 10^{-15}$
	$r_{SAO} - \bar{r} = +137.63$ m	-2.7×10^{-15}
	$r_{GSFC} - \bar{r} = -58.4$ m	$+1.16 \times 10^{-15}$
		RMS $\delta\left(\frac{\Delta\phi}{c^2}\right) = 1.93 \times 10^{-15}$
	Average Relative Velocity, $\bar{v}$	$\delta\left(\frac{v^2}{2c^2}\right)$ from average
	($\bar{v}$ = 228,510.0 cm/sec)	
	$v_{JPL} - \bar{v} = 0.1$ cm/sec	$+0.2 \times 10^{-16}$
	$v_{SAO} - \bar{v} = -0.7$ cm/sec	-1.8×10^{-16}
	$v_{GSFC} - \bar{v} = -0.5$ cm/sec	$+1.3 \times 10^{-16}$
		RMS $\delta\left(\frac{v^2}{2c^2}\right) = 1.29 \times 10^{-16}$
1240 (apogee)	Average Radius from Earth Center	$\delta\frac{(\Delta\phi)}{c^2}$ from average
	$\bar{r}$ = 16,624,474.35 m	
	$r_{JPL} - \bar{r} = -77.68$ m	$+1.25 \times 10^{-15}$
	$r_{SAO} - \bar{r} = +134.17$ m	-2.16×10^{-15}
	$r_{GSFC} - \bar{r} = -56.48$ m	$+0.9 \times 10^{-15}$
		RMS $\delta\left(\frac{\Delta\phi}{c^2}\right) = 1.53 \times 10^{-15}$
	$\bar{v}$ = 70,710.3 cm/sec	$\delta\left(\frac{v^2}{2c^2}\right)$ from average
	$v_{JPL} - \bar{v} = -2.33$ cm/sec	-1.8×10^{-16}
	$v_{SAO} - \bar{v} = 4.67$ cm/sec	$+3.6 \times 10^{-16}$
	$v_{GSFC} - \bar{v} = -2.33$ cm/sec	-1.8×10^{-16}
		RMS $\delta\left(\frac{v^2}{2c^2}\right) = 2.55 \times 10^{-16}$

Table 3. (Continued)

Time	$\bar{r} = 11,930,118.6$ m	$\delta\left(\frac{\Delta\phi}{c^2}\right)$ from average
1322	$r_{JPL} - \bar{r} = -72.16$ m	2.2×10^{-15}
	$r_{SAO} - \bar{r} = 122.02$ m	-3.8×10^{-15}
	$r_{GSFC} - \bar{r} = -49.85$ m	1.5×10^{-15}
		RMS $\delta\left(\frac{\Delta\phi}{c^2}\right) = 2.68 \times 10^{-15}$

	$\bar{v} = 449,864.6$ cm/sec	$\delta\left(\frac{v^2}{2c^2}\right)$ from average
	$v_{JPL} - \bar{v} = -0.7$ cm/sec	-3.5×10^{-16}
	$v_{SAO} - \bar{v} = +1.2$ cm/sec	6.0×10^{-16}
	$v_{GSFC} - \bar{v} = -0.5$ cm/sec	-2.0×10^{-16}
		RMS $\delta\left(\frac{v^2}{2c^2}\right) = 4.16 \times 10^{-16}$

Taking RSS of End Points 1215 to 1322 RMS Values:

	$\delta\left(\frac{\Delta\phi}{c^2}\right)$	$\delta\left(\frac{v^2}{2c^2}\right)$
1215	$\pm 1.93 \times 10^{-15}$	$\pm 1.29 \times 10^{-16}$
1322	$\pm 2.68 \times 10^{-15}$	$\pm 4.16 \times 10^{-16}$
Overall	$\pm 3.3 \times 10^{-15}$	$\pm 4.36 \times 10^{-16}$

Error from Trajectory: $\pm 3.33 \times 10^{-15}$

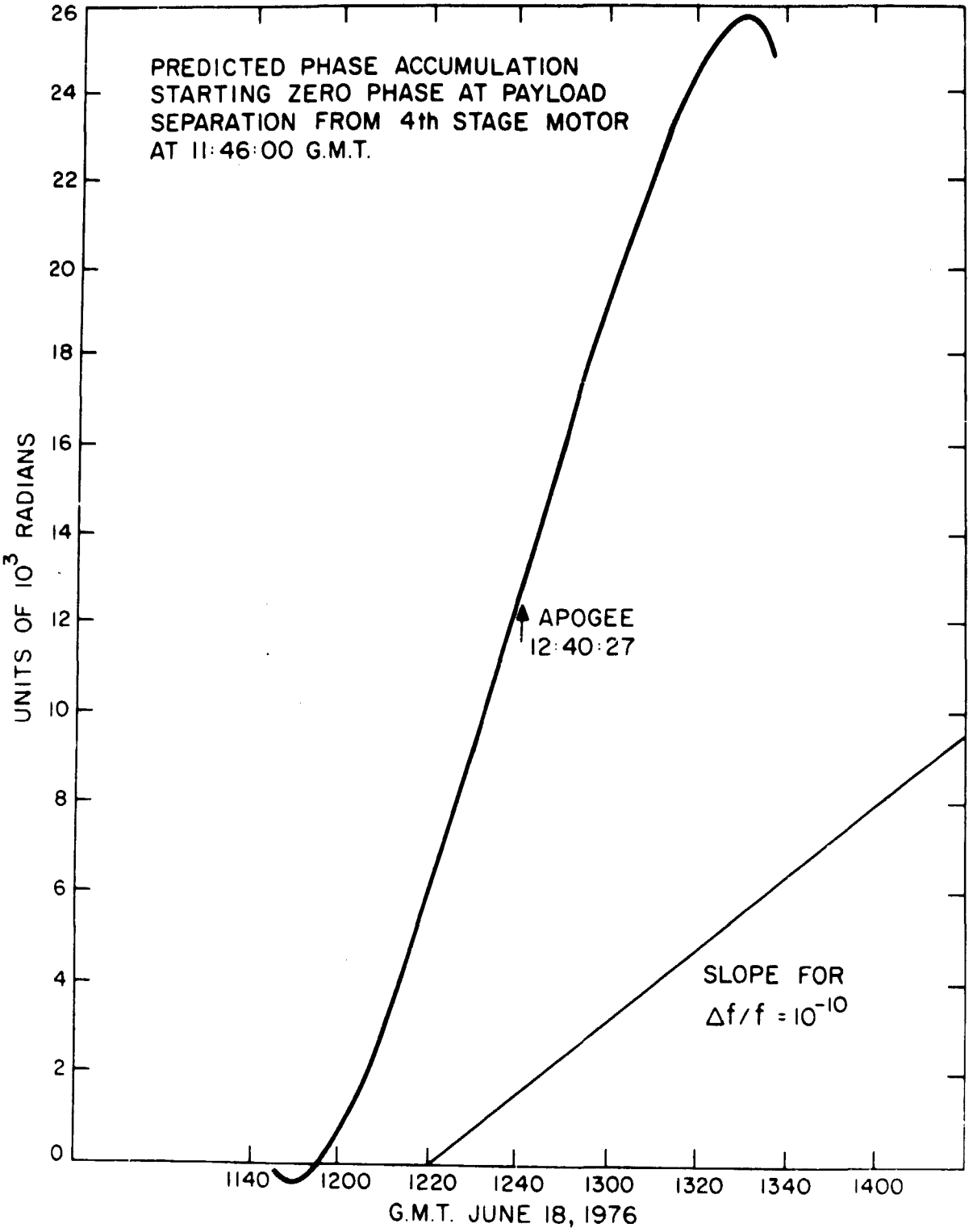

Figure 26. Predicted phase accumulation.

14. CALIBRATION DATA

During the 2-hr time span from launch to impact the probe encountered a variety of environmental changes. The signal levels in the three microwave links varied widely. The effects of these changes on the payload were calibrated during a series of thermal vacuum tests. In the case of magnetic and barometric variations, hystereris effects were observed and, where applicable, the correction algorithms have two branches for use if the direction of the stimulus is changed.

The effects of zero g on the payload maser were estimated by upending it and measuring its output frequency shift. This was found to be about 2.57×10^{-12} and the corresponding cavity shift was found to be 119.3 Hz. One half of this shift, 59.65 Hz, was taken as the shift to zero g, and, before launch the cavity frequency was offset by this amount so that when it was in a weightless condition it would be close to the properly tuned frequency. While our confidence in the structural integrity of the cavity was good as it had survived some very severe shock and vibration tests, we developed further corrections to be used in the event that the cavity shifted several hundred Hz combined with the occurrence of a substantial change in atomic hydrogen flux as observed by a variation in maser output power. The cavity shift was measured from the redshift prediction using a 500-sec segment of data near apogee. The difference in the output frequency of the maser from the predicted value was -2.91×10^{-13} in $\Delta f/f$. From this we deduce that the cavity was low in frequency by 20 Hz. This small shift combined with the negligible change in maser output power level rendered the correction for flux variation completely negligible. The value -2.91×10^{-13} in $\Delta f/f$ was taken as a fixed frequency offset throughout the mission and was incorporated as a constant rate of phase accumulation in the phase prediction as shown in the data processing diagram given as Figure 17.

The only effect that was not simulated during the test sequence was the sustained thrust acceleration of up to 20 g from the rocket. Mechanical stress analyses and stress testing of components gave us confidence that the probe would survive and

that whatever momentary deformations occurred, such as the foam supports of magnetic shields in the maser, would return to their original state within a few minutes.

A number of effects were identified that produced significant frequency shifts and frequency correction formulas were developed during the test phases of the payload. These are shown in Table 4 "Sources of Possible Bias Errors." In particular we must keep in mind the possible errors involved in making these corrections since they will contribute uncertainty in the measuring accuracy of the overall experimental apparatus. The table shows the magnitude of the variation various perturbations in the interval 1215/1322 GMT and the predicted possible bias error estimated at the 1σ level of confidence.

The time signatures of these effects is given in Appendix II under two categories: Maser Frequency Variation Corrections and System Phase Variation Corrections. The latter are very small compared to the frequency effects and their contributions to overall bias errors are not considered to be significant.

The combination of all the corrections for phase and frequency effects is shown in Figure 27 in terms of phase versus time.

Not included in the above is the calibration of the fixed offset error of the probe maser versus the ground maser. Owing to changes in the design of the maser for space use its temperature and magnetic fields are different from the ground masers. The net offset is 5.5×10^{-12} in $\Delta f/f$, the probe running at a higher frequency by this amount.

Table 4. Sources of possible bias errors.

Parameter	Correction formula	Range of variable 1215–1240	Range of variable 1240–1322	1σ contribution to Δf/f
Axial magnetic field from trajectory	$\frac{1}{f}\frac{\Delta f}{\Delta H} = (-5.8992 \pm 0.567) \times 10^{-13}$/Oe to apogee	-0.98×10^{-2} Oe	$+3.36 \times 10^{-2}$ Oe	$\pm 0.6 \times 10^{-15}$
	$\frac{1}{f}\frac{\Delta f}{\Delta H} = (-12.7213 \pm 0.894) \times 10^{-13}$/Oe from apogee			$\pm 3.0 \times 10^{-15}$
Maser oven temperature (oven heater voltage)	$\frac{1}{f}\frac{\Delta f}{\Delta H} = (-3.60 \pm 0.60) \times 10^{-14}$/V	-0.25 V	+0.25 V	$\pm 1.5 \times 10^{-15}$
Maser outer can pressure	$\frac{1}{f}\frac{\Delta f}{\Delta P} = (-310.8 \pm 4.3) \times 10^{-14}$/psi	+0.02 psi	+0.02 psi	$\pm 1.7 \times 10^{-15}$
Probe rotation rate	$\frac{1}{f}\frac{\Delta f}{\Delta \Omega} = [-(1.435 \pm 0.48) + (0.148 \pm 0.0084)\Omega] \times 10^{-15}$/rpm	+1.4 rpm	+1.8 rpm	$\pm 4.6 \times 10^{-15}$
Trajectory uncertainties	See Table 3			$\pm 3.3 \times 10^{-15}$
Root-sum-squares: Estimate of overall possible bias				$\pm 6.8 \times 10^{-15}$

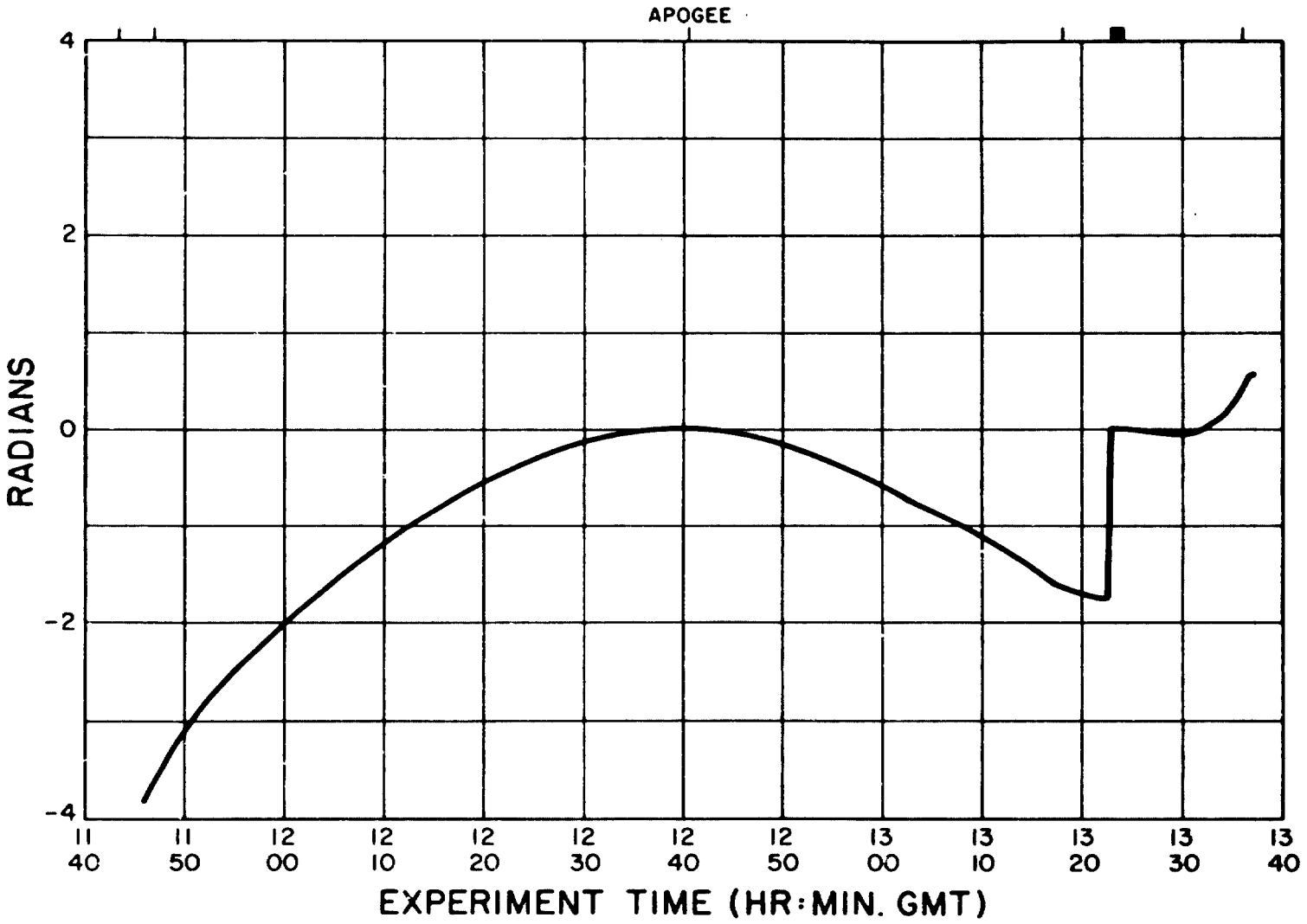

Figure 27. Combination of all corrections.

15. EXPERIMENT RESULTS

The relativistic effects we are testing, have been discussed in Section 7 and are contained in equation (15):

$$\frac{\Delta f_p(t)}{f} = \frac{\phi_p(t) - \phi_e}{c^2} - \frac{\left|\vec{\beta}_1(t) - \vec{\beta}_2(t)\right|^2}{2} - \frac{\Delta t}{2c}\,\vec{\epsilon}_{23}(t) \cdot \vec{a}_3(t) \quad . \tag{15}$$

The trajectory data and the map of the geopotential provide the information we require to generate a predicted value $[\Delta f(t)/f]_p$ as shown in the data-reduction flow plan (Figure 17). The predictions of the relativistic effects and the systematic phase and frequency shifts are all expressed in terms of accumulated phase shifts at the 2117.7-MHz uplink frequency. For convenience these data are all normalized to zero at apogee and have been normalized again to zero after the interruption at 1322:47 GMT. Similarly, the sine cosine observations given in Figures (18) and (19) from the doppler cancelling system have been expressed in terms of accumulated phase normalized to zero at apogee.

The uncorrected residuals resulting from the difference $\Delta\phi(t) = \phi_p^*(t) - \phi_e(t)$ are shown in Figure 28. The average slope in the interval 1235:27 to 1245:27 is used to determine the probe maser offset frequency owing to launch and zero g effects. The frequency offset, as mentioned earlier, was 3.1×10^{-13} on $\Delta f/f$, which, when removed from the plot shown in Figure 28 gives the result shown in Figure 29. The predicted systematic phase variations relating to the maser and system shown in Figure 27, when removed from the data, give the overall phase residuals shown in Figure 30. These have been smoothed by use of a 100-sec filter weighted by a Hanning function. The time derivative of the phase, expressed as $\Delta f/f$, is shown in Figure 31. Here we observe most vividly the discontinuity that resulted when the system was relocked after the uplink transmitter dropped out at 1322:47. Despite repeated efforts to understand this shift, it remains a mystery. All phase lock loops were relocked

*This prediction also includes the 5.5×10^{-12} offset between probe and ground masers measured before the flight.

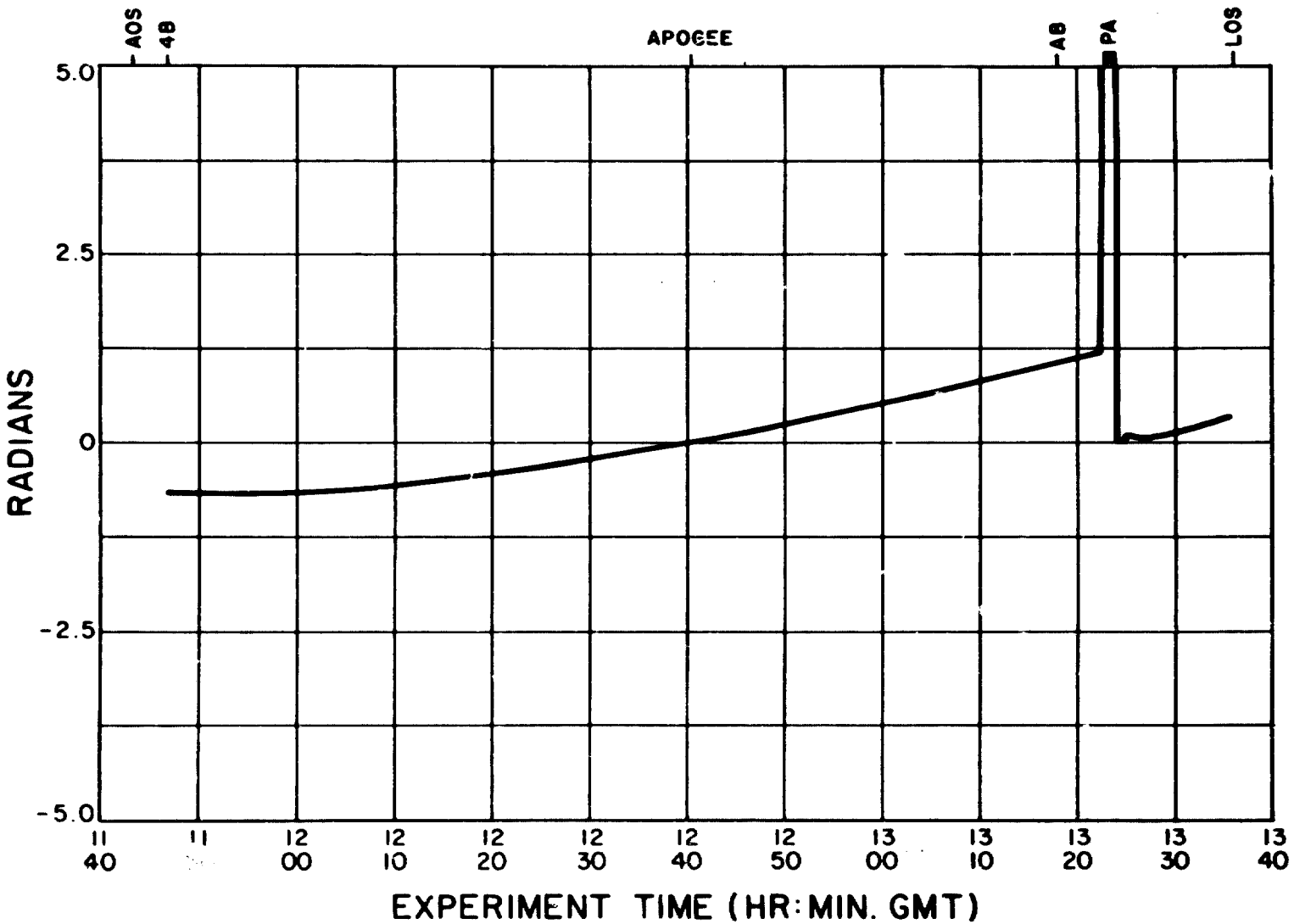

Figure 28. Redshift phase residuals– uncorrected.

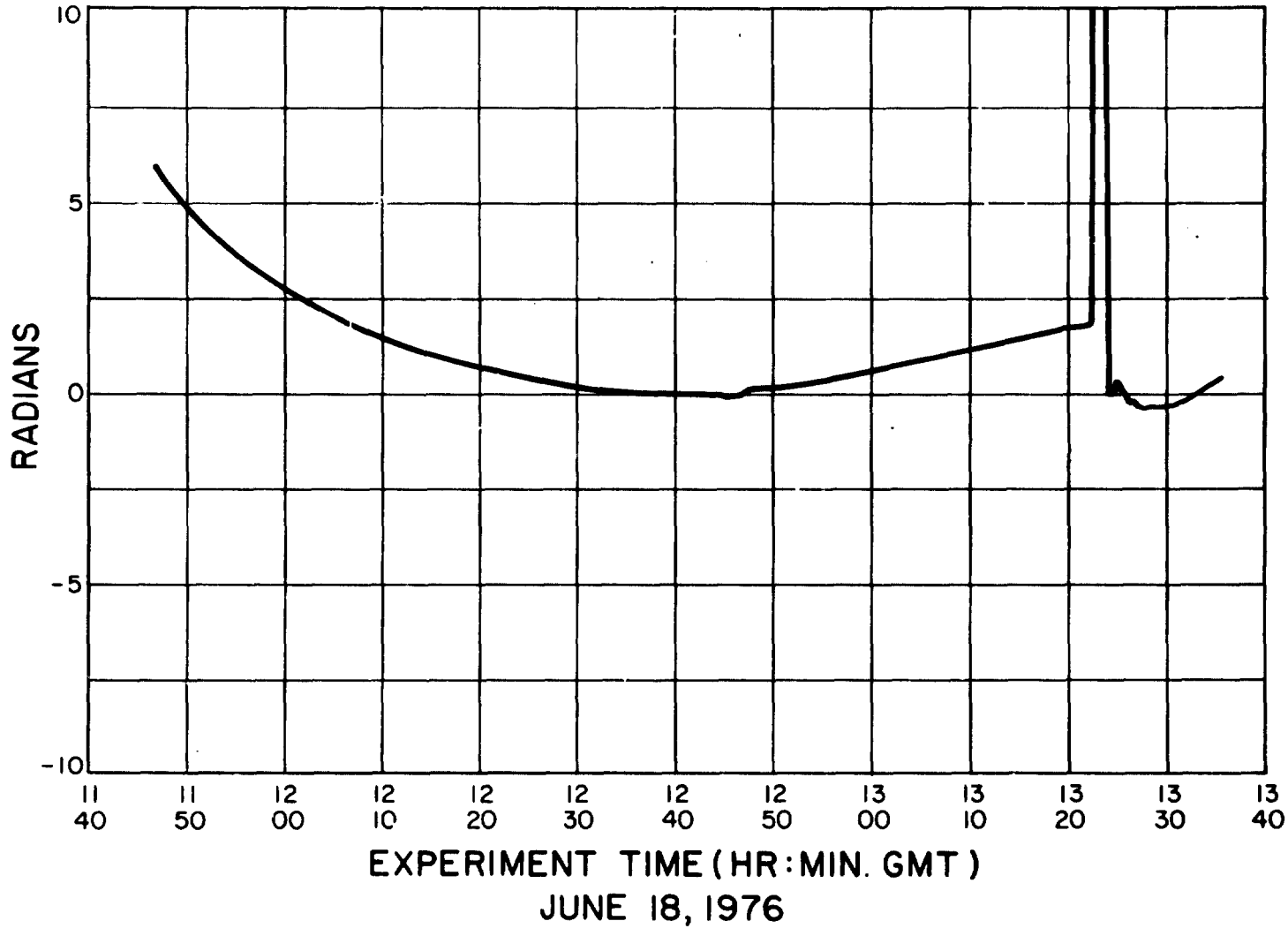

Figure 29. Redshift phase residuals -3.1×10^{-13} slope removed.

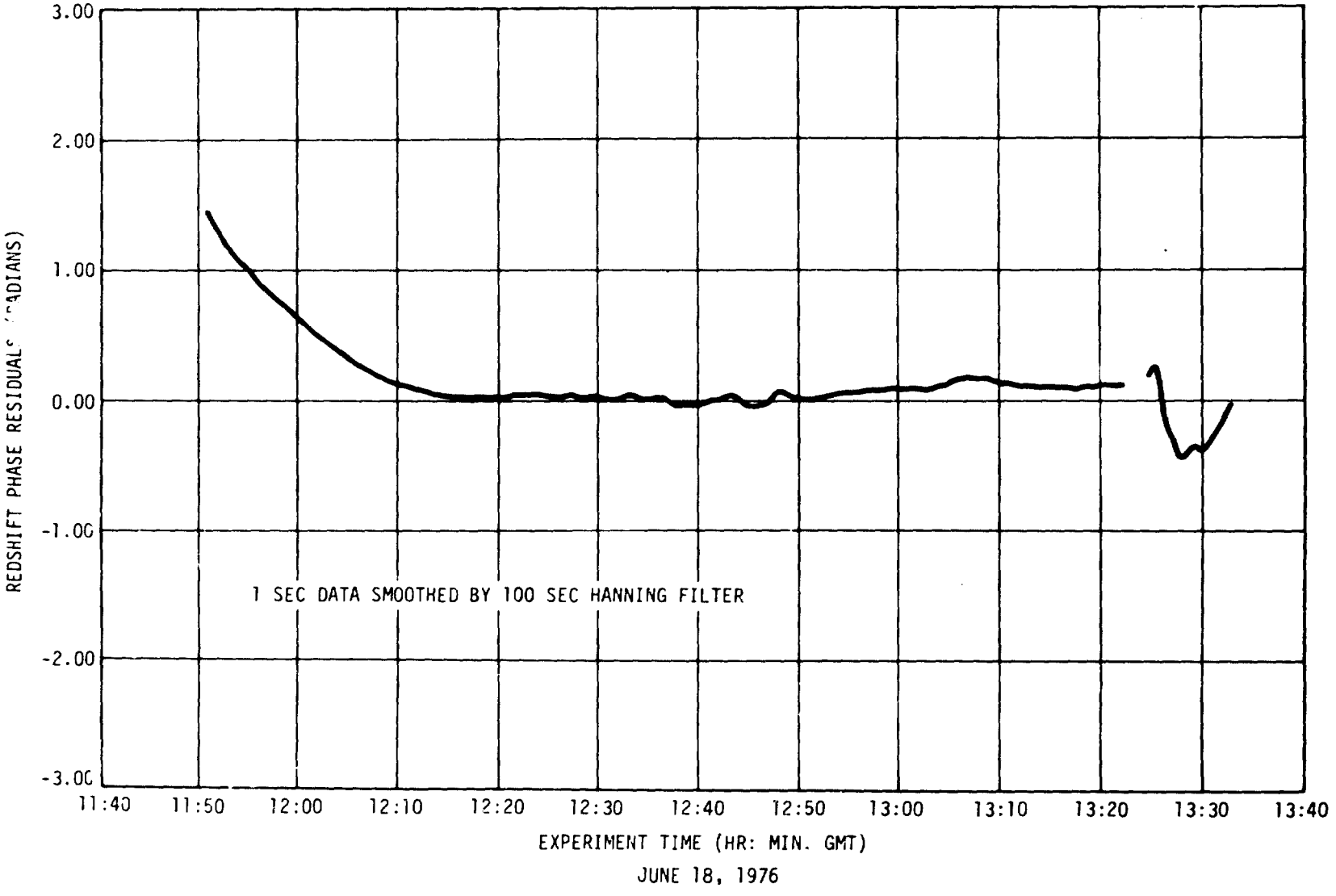

Figure 30. Redshift phase residuals.

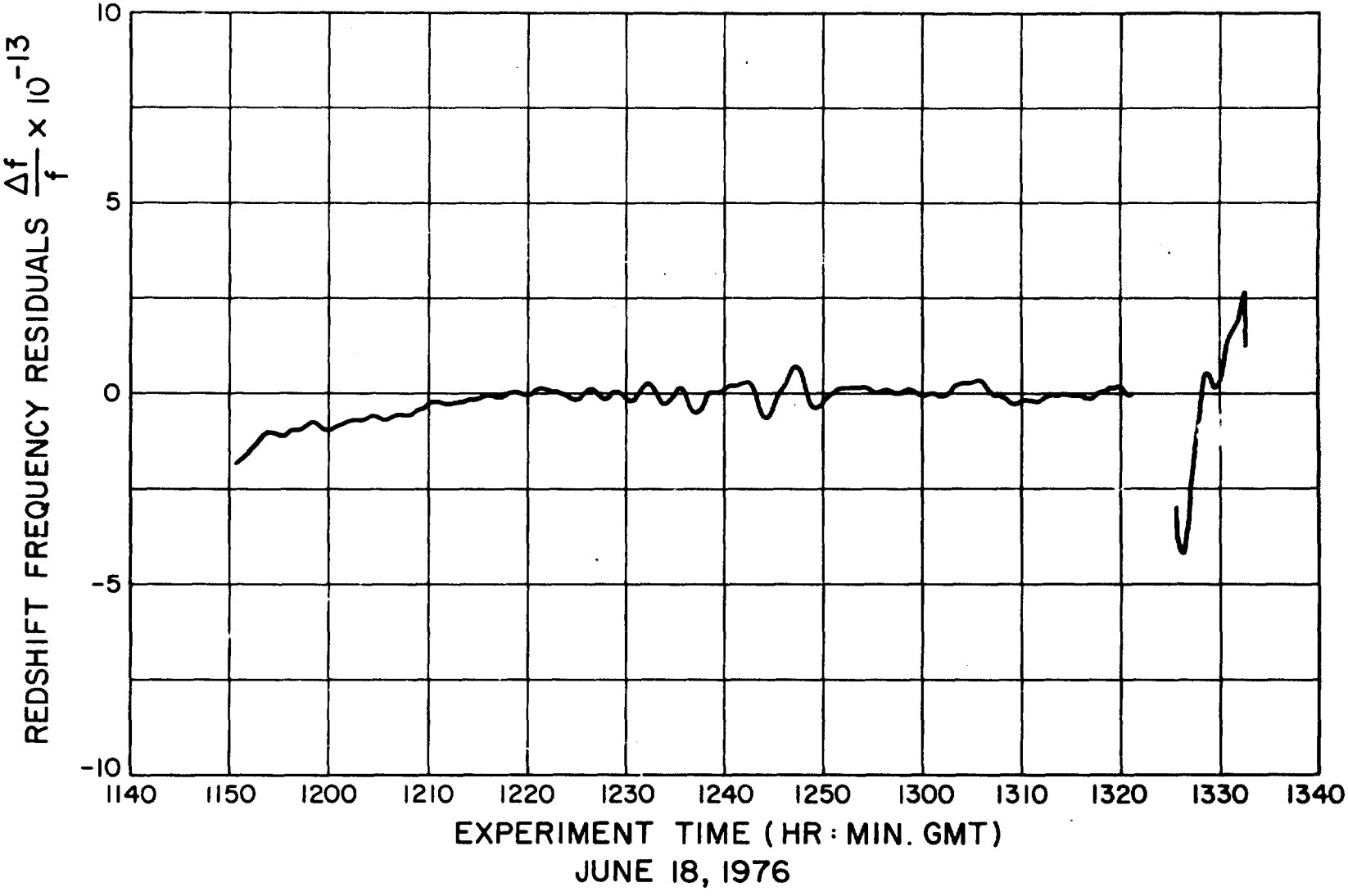

Figure 31. Redshift frequency residuals.

correctly and all monitored quantities were found to be normal. The opportunities for conjecture are almost boundless. Because of this uncertainty we have decided not to use the data after 1322:47.

The stabilization of the payload maser frequency after the thrust acceleration and mechanical shocks during launch was not simulated in ground tests and we could only estimate the time required. From the phase residual plot (Figure 30), we see that this restabilization required about 25 min, which was longer than anticipated. At 1215. the transient has died out and while there is only 2.94×10^{-11} change in $\Delta\phi/c^2$ up to apogee at 1240:27 these data are retained in the statistical consideration of the results. From apogee to 1322 we have a change of 1.13×10^{-10} and the experimental data set is chiefly over this range.

A statistical description of the data is shown in the regression analysis of frequency measurements made over separate 100-sec intervals over the time interval. Figure 32 shows the least squares fit of a straight line to the residual frequency data. The formal value of the quantity ϵ describing the agreement of our data with the redshift hypothesis is $\epsilon = (5 \pm 126) \times 10^{-6}$ and we have

$$\left.\frac{\Delta f}{f}\right|_{\text{formal}} = [1 + (5 \pm 126) \times 10^{-6}] \frac{\Delta\phi}{c^2} \quad .$$

We must combine the value of ϵ with the estimate of uncertainty from possible bias in the overall system shown in Table 4:

$$\frac{\left.\frac{\Delta f}{f}\right|_{\text{bias}}}{\frac{\Delta\phi}{c^2}} = \pm\frac{6.8 \times 10^{-15}}{1.13 \times 10^{-10}} = \pm\, 60.2 \times 10^{-6} \quad .$$

Combining the bias uncertainty with the formal statistical uncertainty as root-sum-squares we have

$$\frac{\Delta f}{f} = [1 \pm (5 \pm 140) \times 10^{-6}] \frac{\Delta\phi}{c^2}$$

as our final result.

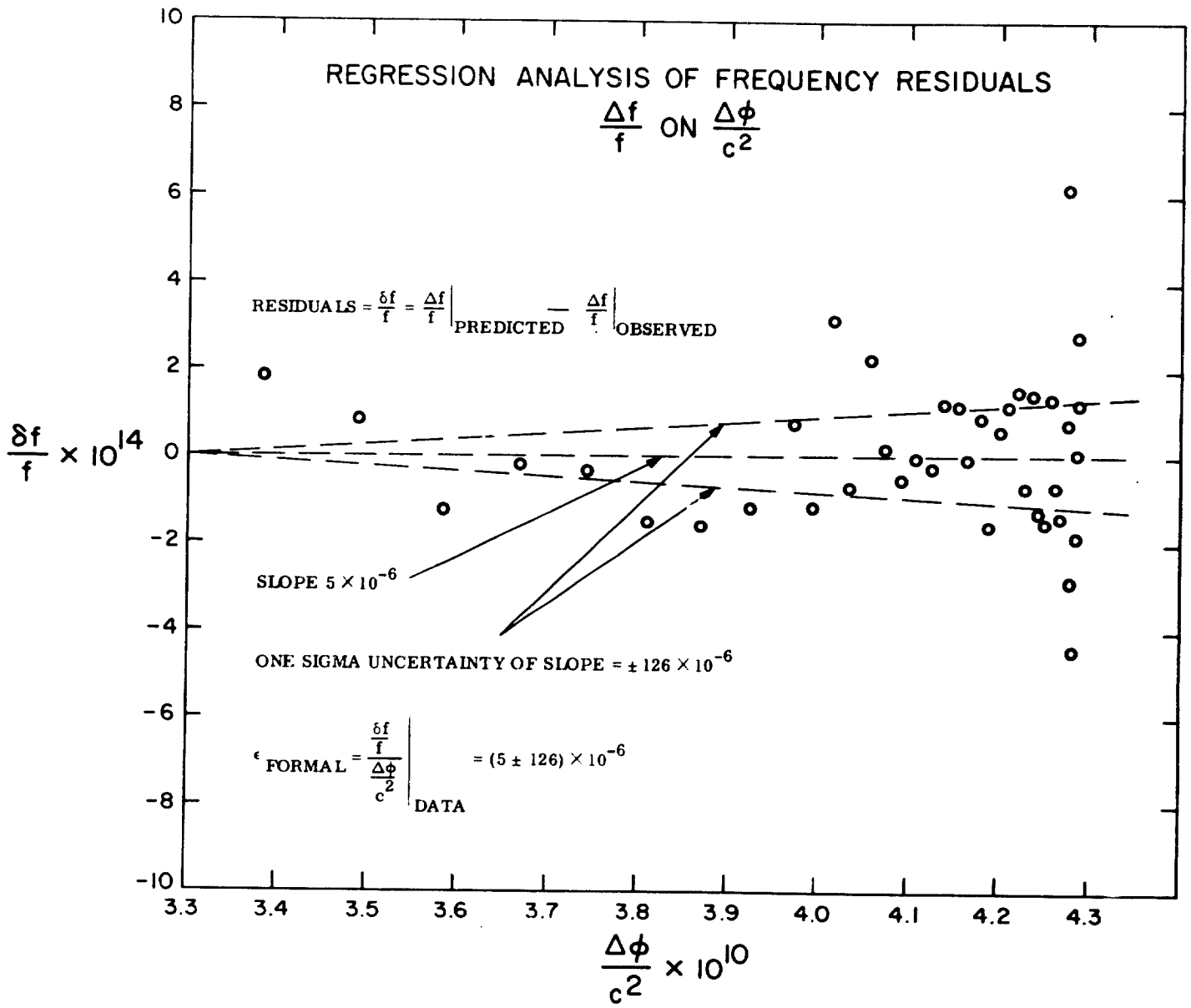

Figure 32. Regression analysis of frequency residuals.

16. CONCLUSIONS

The agreement of the experimental data with redshift prediction discussed in the previous section depends on two major a priori assumptions. First, we have assumed that the velocity of light is constant and isotropic for distances over which there is a substantial difference in gravitational acceleration and potential. Secondly, we have assumed that the time dilation, or second-order doppler effect, has been tested experimentally at sufficient accuracy to support the redshift conclusion and, further that the effect, which to date has been tested only under local conditions, can safely be applied to the nonlocal situation where there is substantial curvature in the spacetime metric.

The question of the precision of the verification of time dilation has been reviewed by Newman et al. (1978).* To date the smallest experimental uncertainty has been obtained in the measurement of muon lifetimes by Bailey et al. (1977), who cite lifetimes τ_0 at different values of $\gamma_i = (1 - \beta_i^2)^{-1/2}$ and conclude that

$$\frac{\tau_0(\gamma_1) - \tau_0(\gamma_2)}{\tau_0(\gamma_1)} = (0.02 \pm 0.09) \times 10^{-2} \quad \text{or} \quad 0.1\% \text{ precision.}$$

if we attribute all the uncertainty in our experiment to the second-order doppler effect and assume that the redshift is exactly predicted we have

$$\frac{\Delta f/f}{\Delta(v^2/2c^2)} = 1 + (5 \pm 140) \times 10^{-6}$$

and a corresponding precision of 0.014%. This precision is the same as that quoted for the redshift because the range of $v^2/2c^2$ is almost exactly the same as the range of $\Delta\phi/c^2$ since the probe was in nearly free fall.

The question of a possible asymmetry in the one-way and two-way velocity of light measurement can also be addressed if we refer to the relativistically corrected

*We are grateful to Prof. N. F. Ramsey for pointing out that the best test of special relativity to date is at the 10^{-3} level and that our previous conclusions should be reconsidered.

doppler frequency shift expressions given in equations (11) and (12), and write c_{12} as the velocity of light from earth to probe and c_{21} for the velocity in the opposite sense. Under these conditions, if we expand equations (11) and (12) we have the following:

$$\frac{f' - f_0}{f_0} \doteq \left(\frac{\phi_2 - \phi_3}{c^2} - \text{etc.}\right) + \frac{\dot{r}_{23}}{c}$$

$$\frac{f'' - f_0}{f_0} \doteq \frac{\dot{r}_{23}}{c} - \frac{\dot{r}_{12}}{c} \quad .$$

The output from mixer M3 in Figure 3 gives

$$\frac{\Delta f_c}{f_0} = \frac{1}{f_0}\left(f' - f_0 - \frac{f'' - f_0}{2}\right)$$

$$\doteq \frac{\Delta f}{f_0} + \frac{\dot{r}_{23}}{c_{23}} + \frac{\dot{r}_{12}}{2c_{12}} - \frac{\dot{r}_{23}}{2c_{23}}$$

$$\doteq \frac{\Delta f}{f_0} + \frac{\dot{r}}{2}\left(\frac{1}{c_{12}} - \frac{1}{c_{23}}\right) \quad .$$

Here we have written $\dot{\vec{r}}_{12} = -\dot{\vec{r}}_{23} = \dot{r}$. Writing $\Delta c = c_{23} - c_{12}$ we have

$$\frac{\Delta fc}{f} \doteq \frac{\Delta f}{f_0} + \frac{\dot{r}}{2}\frac{\Delta c}{c} \quad .$$

If we ascribe all the observed departure of frequency to the possible anisotropy of the velocity of light we conclude that the value of $\Delta c/c$ is on the order of 3×10^{-9} in the data set from 1215 to 1322 GMT.*

The concept of separating the several different effects is not really legitimate since the theory we are testing will fail if any of these effects is not correctly observed. What is actually being tested is the self consistency of the General Theory of Relativity.

*A recent result on the local invariance of the length of a laser cavity has been reported by Brillet and Hall (1979).

The measure of this self consistency is the experimentally determined one-sigma probability limits of the departure of the frequency shift from the prediction divided by the magnitude of the total frequency shift. From this point of view we have

$$\frac{\Delta f}{f} = [1 + (2.5 \pm 63) \times 10^{-6}] \left[\frac{\Delta\phi}{c^2} + \Delta\left(\frac{v^2}{2c^2}\right) \right]$$

as formal error to which we add the possible apparatus bias of $\pm 6.8 \times 10^{-15}$ in $\Delta f/f$, which causes a 29.4×10^{-6} probable error in the determination of

$$\left(\frac{\Delta\phi}{c^2} + \Delta \frac{v^2}{2c^2}\right) \quad .$$

The conclusion we reach for the self-consistency of the hypothesis is

$$\frac{\Delta f}{f} = [1 + (2.5 \pm 70) \times 10^{-6}] \left[\frac{\Delta\phi}{c^2} + \Delta\left(\frac{v^2}{2c^2}\right) \right] \quad .$$

The experiment confirms the self-consistency of the General Theory of Relativity at the 70 parts per million level. To date the best test of the Special Theory has been made with high-energy muons from CERN particle accelerator and the confirmation reported by Bailey et al. (1977) is at the 1000 parts per million level. The previous test of the gravitational redshift by R.V. Pound et al. (1965) using the Mössbauer radiation from Fe_{57} over a height of 75 feet is at the 10,000 parts per million level. We believe that the experiment described in this report has substantially improved the confidence we have in the General Theory of Relativity and the meshing of the Special Theory and the Principle of Equivalence upon which it is based.

17. REFERENCES AND BIBLIOGRAPHY

Allan, D.W. (1966). Proc. of the IEEE, 54, 221.

Appleton, E.V. (1932). J. Inst. Elect. Engrs., 7, 642.

Badessa, R.S., Kent, R.L., Nowell, J.C., and Searle, C.L. (1960). Proc. IRE, 48, 758.

Bailey, J., Borer, K., Combley, F., Drumm, H., Krienen, F., Lange, F., Picasso, E., von Ruden, W., Field, J.H., Flegel, W., and Hattersley, P.M. (1977). Nature, 218, 301-302.

Baugher, C. (1980). NASA/Marshall Space Flight Center Report. In preparation.

Braginsky, V.B., and Panov, V.I. (1971). Zurn, Éksp. Teor. Fiz., 61, 875.

Brillet, A., and Hall, J.L. (1979). Phys. Rev. Lett., 42 (no. 9), 549-552.

Dicke, R.H. (1964). The Theoretical Significance of Experimental Relativity, New York.

Drever, R.W. (1961). Phil. Mag., 6, 683-687.

Einstein, A. (1905). Ann. der Phys., 17, 891.

Einstein, A. (1911). Ann. der Phys., 35, 898.

Einstein, A. (1912). Ann. der Phys., 38, 355.

Einstein, A. (1913). Phys. Zs., 14, 1249.

Eddington, A.S. (1922). The Mathematical Theory of Relativity. London.

Eötvös, R. v., Pekov, D., and Iekete, E. (1927). Ann. der Phys., 68, 11.

Hellwig, H., Vessot, R.F.C., Levine, M.W., Zitzewitz, P.W., Allan, D.W., and Glaze, D.J. (1970). IEEE Trans. on Instr. Meas., IM-19 (no. 4).

Hughes, V.W., and Robinson, H.G. (1960). Phys. Rev. Lett., 4, 342-344.

Kleppner, D., Vessot, R.F.C., and Ramsey, N.F. (1970). Astrophys. and Sp. Sci., 6, 13.

Lightman, A.P., and Lee, D.L. (1973). Phys. Rev., D8, 364.

Newman, D., Ford, G.W., Rich, A., and Sweetman, E. (1978). Phys. Rev. Lett., 40 (no. 21), 1355-1358.

Newton, I. (1686). Philosophiae Naturalis Principia Mathematica, London.

Ni, W.T. (1977). Phys. Rev. Lett., 38, 301.

Ni, W.T. (1979). Preprint.

Pound, R.V. (1973). "Comments on the Problem Set by Propagation Effects." re: Gravitational Redshift Program Review, October 23.

Pound, R.V., and Rebka, G.A. (1960). Phys. Rev. Lett., 4, 337.

Pound, R.V., and Snider, J.L. (1965). Phys. Rev., 140, 13, 788.

Ramsey, N.F. (1956). Molecular Beams. Oxford.

Robertson, H.P. (1962). In Space Age Astronomy, ed. by A.J. Deutsch and W.B. Klemperer, New York, p. 228.

Roll, P.G., Krotkov, R., and Dicke, R.H. (1964). Ann. Phys., 26, 442-517.

Ryan, J.W. (1973). Error Analysis of the Gravitational Redshift Probe Trajectory (Redshift Review Action ITEM Letter to Dr. N.G. Roman, NASA Hq. Wash., D.C.). NASA Goddard Space Flight Center File #8203, December 7.

Schiff, L.I. (1962). General Relativity: Theory and Experiment. Journ. Indust. and Appl. Math., 10, 795-801; see also Comparison of Theory and Observation in General Relativity in Relativity Theory and Astrophysics. I. Relativity and Cosmology. American Mathematical Society, Providence, R.I. (1962).

Townsend, G.E., and Alford, R.L. (1972). Analysis of the Ground Based Tracking Requirements for "Redshift." Northrup Services, Inc., Huntsville, Ala.

Tucker, A.J., and Fannin, B.M. (1968). Journ. Geophys. Res. Space Phys., 73 (no. 13), 4325-4334.

Vessot, R.F.C., and Levine, M.W. (1971). In Proc. Conf. Experimental Tests of Gravitational Theories, ed. by R.W. Davies. NASA CalTech and JPL Tech Memo 33-499, pp. 54-64.

APPENDIX I

THE NASA/JPL TRAJECTORY SOLUTION

APPENDIX I

THE NASA/JPL TRAJECTORY SOLUTION

JET PROPULSION LABORATORY

ENGINEERING MEMORANDUM

314-187

7 May 1979

TO: T. H. Thornton

FROM: A. S. Liu/J. D. Anderson/D. L. Cain/P. A. Laing

SUBJECT: Gravitational Redshift Probe Orbit Determination from Counted Cycles Using SAO Hydrogen Masers

REFERENCE: Gravitational Redshift Space-Probe Experiment, R.F.C. Vessot, M. W. Levine, GP-A Project Report from Smithsonian Astrophysical Observatory, April 1977

I. INTRODUCTION

An experiment was undertaken in 1976 by Dr. R.F.C. Vessot and associates of the Smithsonian Astrophysical Observatory (SAO) to test Einstein's theory of the gravitational redshift effect (Ref. 1). This experiment used ground based as well as rocket-borne hydrogen maser atomic clock. By comparing the transmitted probe frequency (controlled by the probe hydrogen maser), with the ground reference frequency it was possible to measure the Einstein redshift effect to an accuracy of 1 part (10^{14}), which was 100 times more precise than ever achieved. To assist SAO in improving this experiment, we produced and sent to SAO a trajectory ephemeris. This trajectory was determined from simultaneous doppler tracking from 4 stations, 3 of which were equipped with SAO masers. The standard deviations of the orbital parameters were derived from a weighted least square fit to the doppler data. These standard deviations, were transformed into speed and radial distance errors by simple conic equations. The maximum radial distance error was 12 meters, occurring near the end of the flight, and the velocity error was .04 cm/sec.

With this trajectory, it will be possible to separate the redshift effect from doppler motion to the accuracy of 1 part/10^{15}.

II. ANALYSIS

The Gravitational Redshift Space-Probe was launched in 1976 by a Scout D rocket from Wallops Station. The rocket, which reached an altitude of 10,000 km, was tracked in a 2-way mode from Merrit Island Launch Area (MILA), and simultaneously in a 3-way mode by Bermuda, National Test and Training Facility (NTTF), and Ascension Island.

All stations, with the exception of Ascension Island, were equipped with SAO hyrdogen masers. A-priori station locations, given to us by Dr. Vessot, and post-priori, station locations determined by our orbit determination program, POEAS, are listed in Table I. Coordinates are given in a cylindrical system, (distance km from spin axis, CU, distance km from equatorial plane, CV, and longitude in degrees, LO). The post-priori statistics for all stations were about 7 meters. For the most part, station locations were adjusted from two to five meters, however, with the singular exception for longitudes of Bermuda and NTTF. Bermuda's longitude moved eastward by 27 meters and NTTF moved westward by 31 meters corresponding to about 1" error in station locations.

TABLE 1

POST-PRIORI VS A-PRIORI TRACKING STATION LOCATIONS

	CU (KM)	CV (KM)	LO (DEG)
MILA*	5609.0450398	3026.0982923	279.30656250
MILA⁻	5609.0448033	3026.1008317	279.30651987
BERMUDA*	5393.2967222	3393.4044091	295.34189244
BERMUDA⁻	5393.3020999	3993.4021880	295.34213250
NTTF*	4963.4455187	3992.1940424	283.15744095
NTTF⁻	4963.4450874	3992.2093687	283.15715810
ASCEN.IS*	6317.7157105	-876.90508990	345.67282925
ASCEN.IS⁻	6317.7158143	-876.90509810	345.67282940

* = Post-priori value

⁻ = A-priori value

The dynamical motion of the probe included perturbational forces caused by a 15th degree and order terrestrial gravitational harmonics, point source effects of the moon, sun and all the planets, plus a small thrust due to venting from the ammonia boiler. We were able to account for this force by first observing the probe's spin rate (approximately 115 rpm), which changed in time during the major portion of the flight. Using this spin information we constructed a cubic polynomial representing the time behavior of the spin rate, w.

1) $w(\text{radians/sec}) = .0288 + 5.47 \times 10^{-3} t + 1.329 \times 10^{-5} t^2 - 1.725 \times 10^{-7} t^3$
where t is the time interval in minutes.

From this, we derived an expression to account for the probe's gas leak acceleration as:

2) $f(\text{km/sec}^2) = f_o/m\ (1+4.8572641 \times 10^{-3} t - 9.4589428 \times 10^{-5} t^2)$
$f = 0$ after 13:18:00

where f_o is a constant (in dynes) to be determined from the tracking data. f_o is normalized for a probe mass of 100 kilograms. The ammonia gas was exhausted after 13:18:00 because no further change in the spin rate was observed.

In addition to the constant of the acceleration profile, two other parameters, U_x, U_y, describing the direction cosines of the thrust vector, were also included and were determined from the data. A third component U_z of this unit vector $\vec{U}$ is formed by:

3) $U_z = (1 - U_x^2 - U_y^2)^{\frac{1}{2}}$

The components of $\vec{U}$ are expressed in the Earth's mean Equator and Equinox of 1950.0 coordinate system. Table II lists the resulting values from a combined least square solution of the orbital elements and station positions and the thrust vector. The thrust magnitude, f_o, was found to be about 163 dynes acting on a 100 kilogram probe. The thrust direction did not deviate by more than 5° from the initial velocity vector because the "tip-off" direction during separation is controlled to about 5°. Using the doppler data, we found the angular separation between the velocity vector and the thrust vector to be 5° ± 7°,

indicating that insofar as the data would allow, the thrust vector and the initial velocity vector were aligned at separation. Since the probe was spinning at 115 rpm, the spin direction was assumed to be fixed throughout this experiment.

Phase coherent counter reading of the 2-way, 3-way data at each second was given us by SAO. These data were averaged to 1 minute doppler samples and processed by our double precision orbit program POEAS. Our final iteration by POEAS used the counter readings directly and a doppler phase or a differential "range" data trajectory was constructed.

The final analysis showed the S-band phase residuals to be less than .8 cycles. The maximum doppler error was 5 millihertz, (excluding last 3 points which were affected by the troposhpere), or a maximum velocity error of .3 mm/sec. A power loss of the uplink transmitter at MILA for about two minutes at 13:22:47 caused a momentary loss of data from all tracking stations. Data from Bermuda from 12:07 to 12:15 were also rejected. The data quality otherwise was superb. Doppler residuals from all stations were on the order of a few millihertz. Plots of the POEAS phase residuals are shown in Figures 1 and 2.

TABLE II

THRUST FROM THE

AMMONIA BOILER VENT

U_x	$-.589635 \pm .066375$
U_y	$-.469563 \pm .021204$
Force on 100 KG Probe	163.177 ± 1.366 (Dynes)

Data residuals from the other three stations, tracking in a 3-way mode, are shown in Figures 3, 4, 5. Plots are expressed in mm/sec vs time, where 1 mm/sec = .015 hz. Bermuda residuals are all on the order of 5 millihertz (Fig. 3). NTTF exhibited noisier data than Bermuda for reasons unknown at present (Fig. 4). Ascension Island's data were received at low elevation angles (below 5°) and at the beginning and end of track showed large tropospheric effects (Fig. 5).

ASL:bw

Distribution

A. L. Berman
W. D. Chaney
D. W. Curkendall
P. B. Esposito
F. B. Estabrook
H. J. Gordon
J. F. Jordan
W. E. Kirhofer
G. S. Levy
W. G. Melbourne
N. A. Renzetti
K. H. Rourke
W. L. Sjogren
G. L. Spradlin
C. J. Vegos

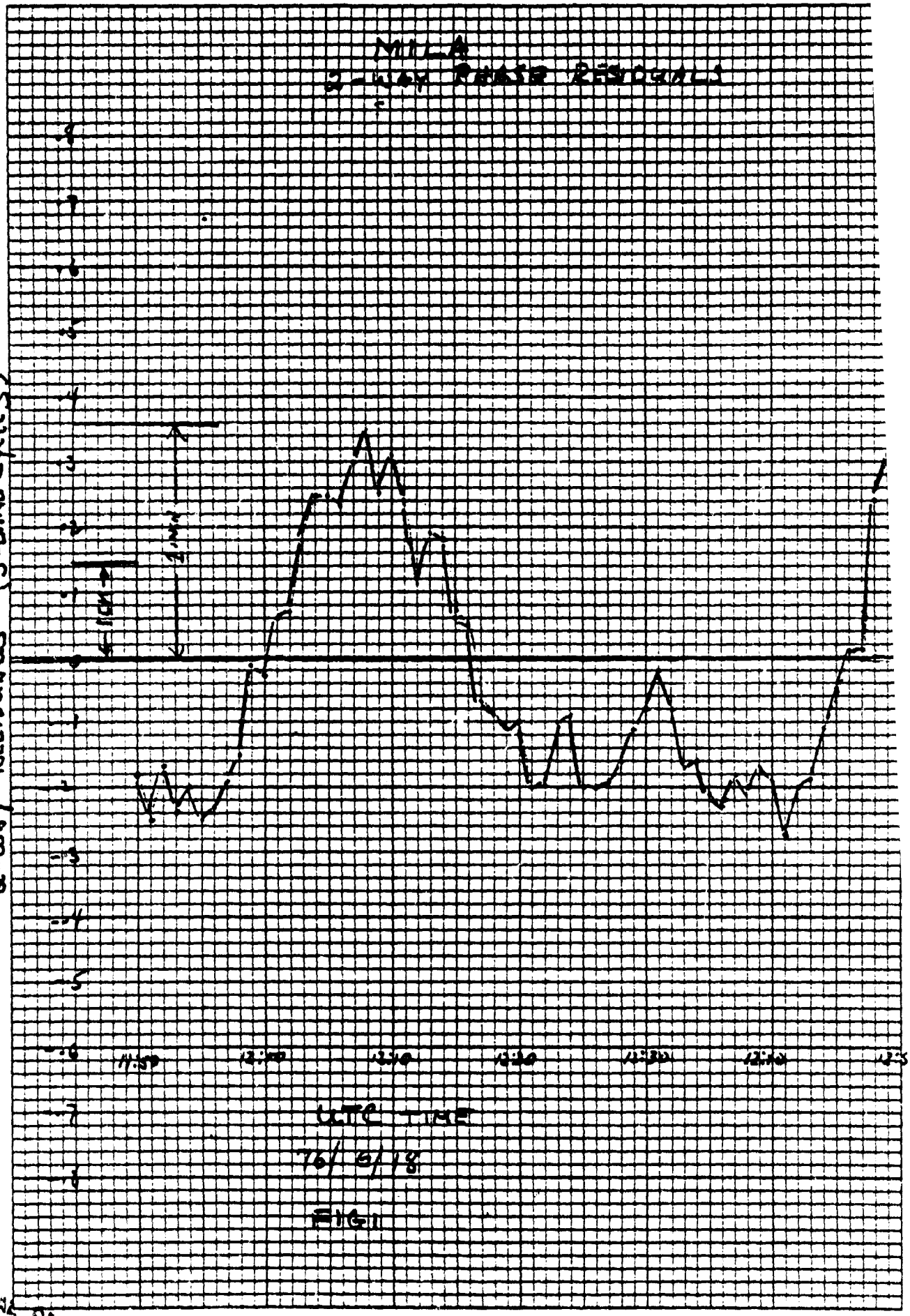

FIG 11

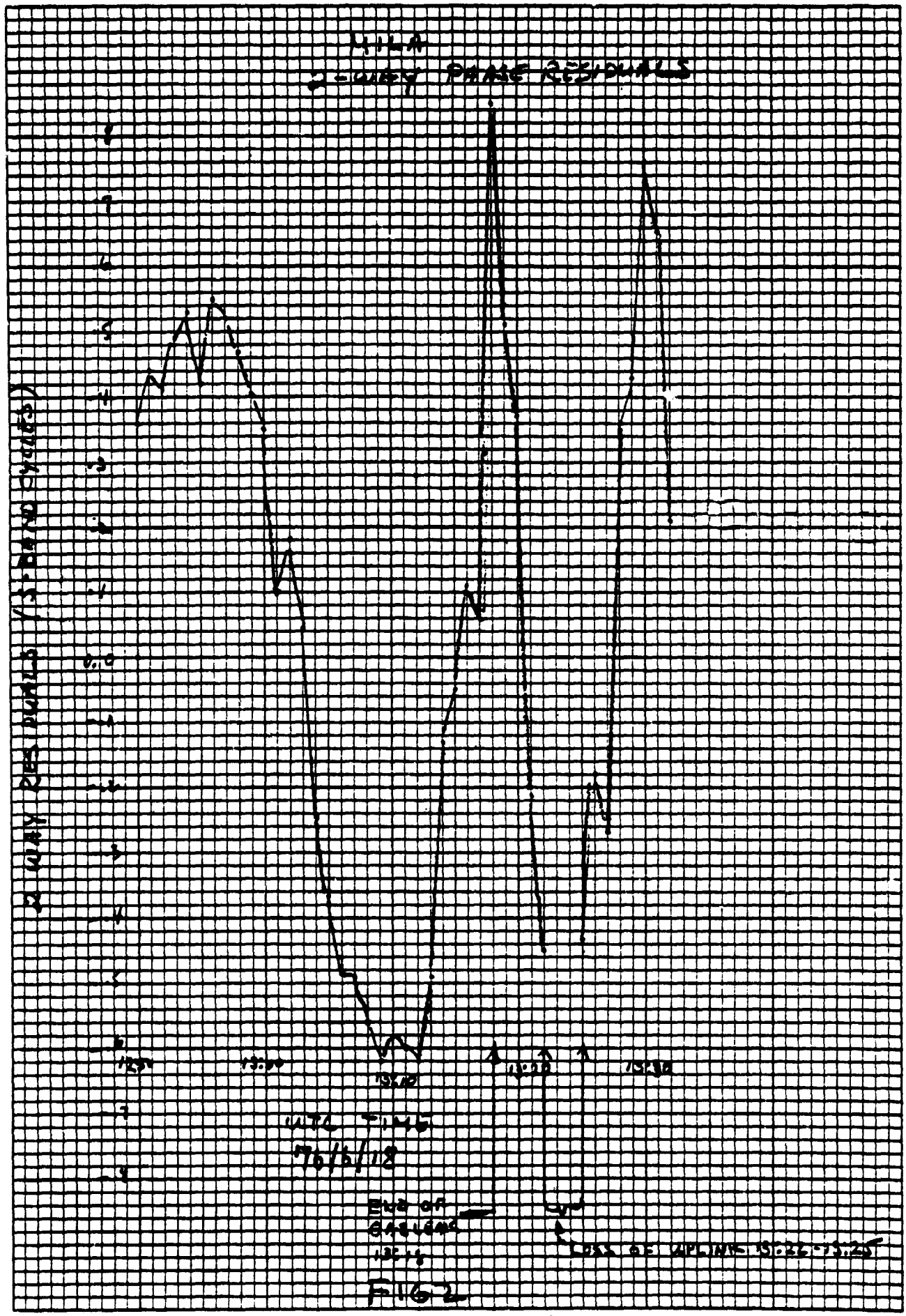

FIG 2

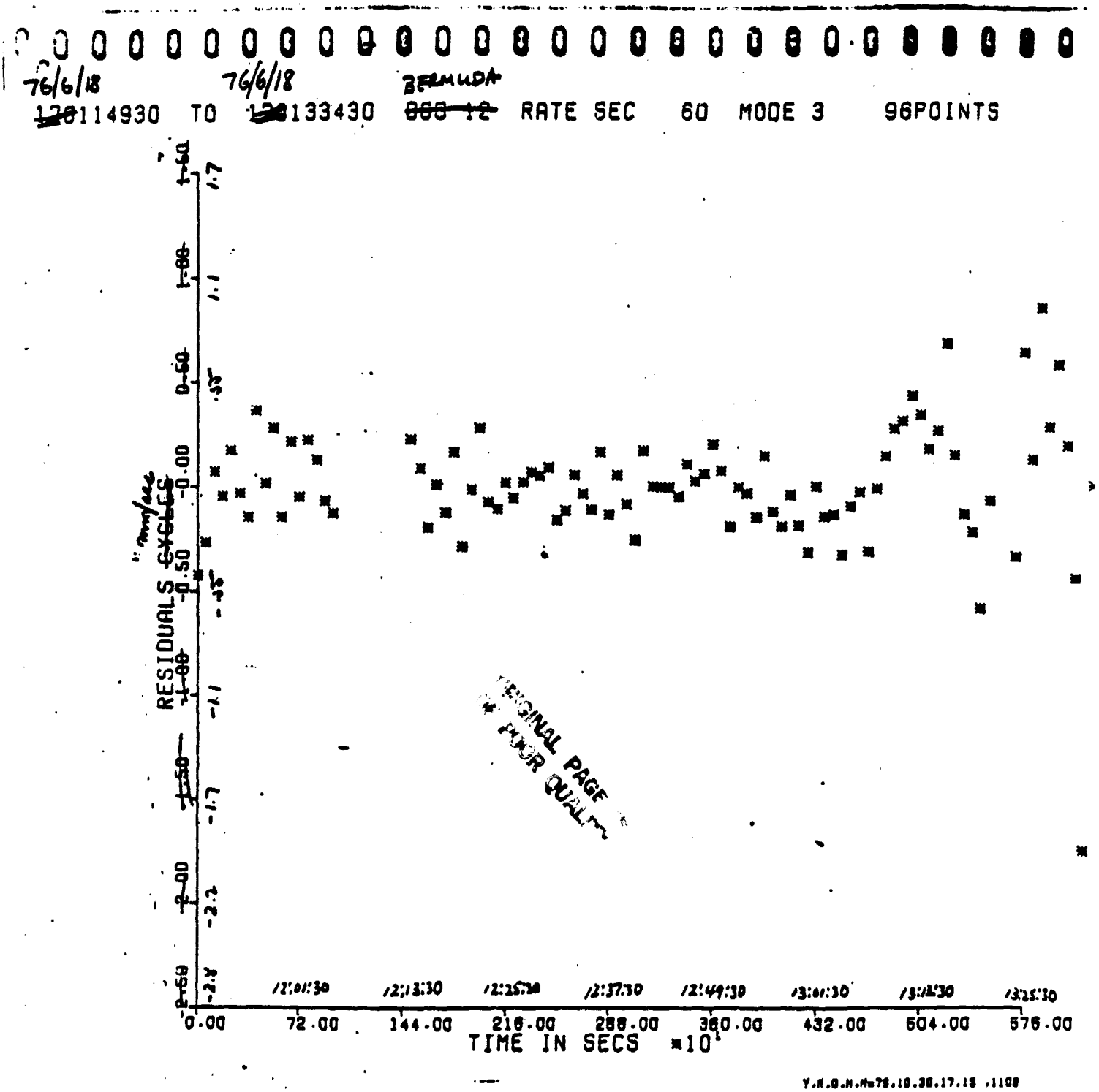
76/6/18
76/6/18
BERMUDA
~~178~~114930 TO ~~178~~133430 ~~060 12~~ RATE SEC 60 MODE 3 96POINTS
RESIDUALS ~~CYCLES~~ mm/sec
+1.50
+1.00
+0.50
-0.00
-0.50
-1.00
-1.50
-2.00
-2.50
1.7
1.1
.57
-.57
-1.1
-1.7
-2.2
-2.8
/2:01:30
/2:13:30
/2:25:30
/2:37:30
/2:49:30
/3:01:30
/3:13:30
/3:25:30
0.00
72.00
144.00
216.00
288.00
360.00
432.00
504.00
576.00
TIME IN SECS ×10
ORIGINAL PAGE IS POOR QUALITY
Y.M.D.H.M=76.10.30.17.15 .1100

FIG 3

76/6/18 76/6/18 NTTF

~~178~~14930 TO ~~178~~133430 ~~866 13~~ RATE SEC 60 MODE 3 104POINTS

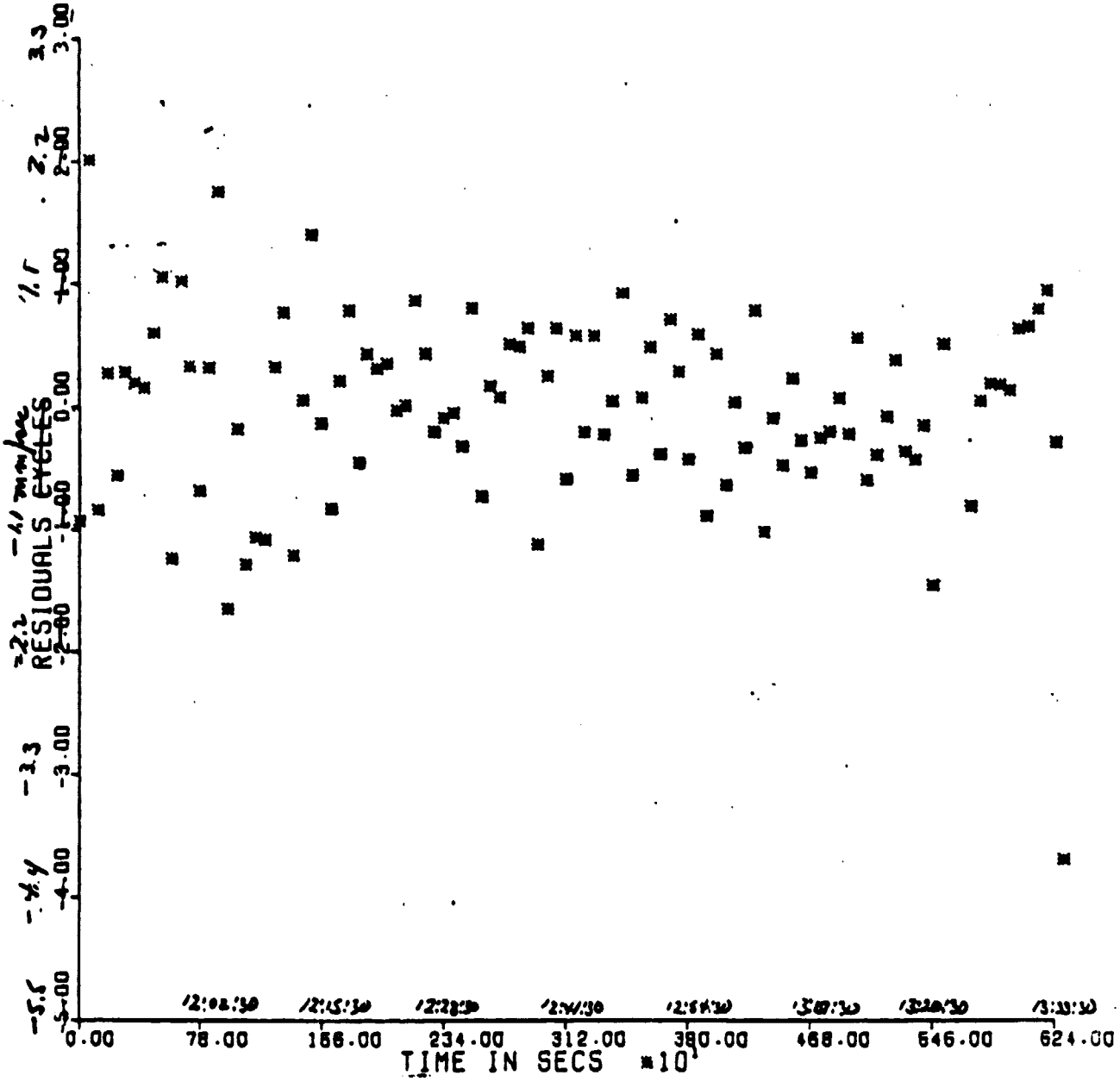

FIG 4

76/6/18 76/6/18 ASCENSION IS

~~178~~121130 TO ~~178~~132130 ~~GSS 14~~ RATE SEC 60 MODE 3 70POINTS

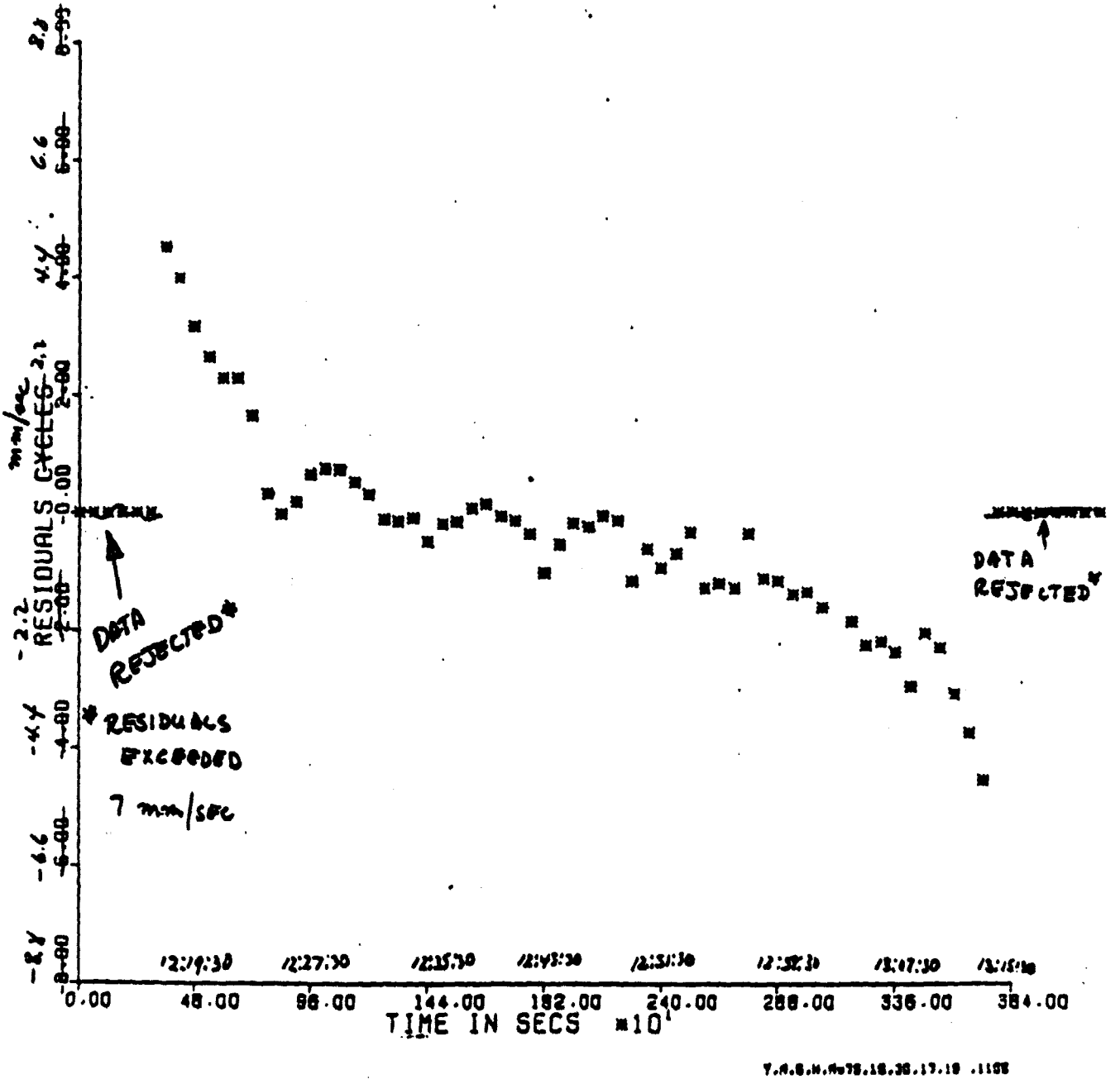

FIG 5

APPENDIX II

MASER FREQUENCY VARIATION CORRECTIONS

SYSTEM PHASE VARIATION CORRECTIONS

MAGNETIC FIELD (AXIAL)

INCLUDES CORRECTION NUMBERS.

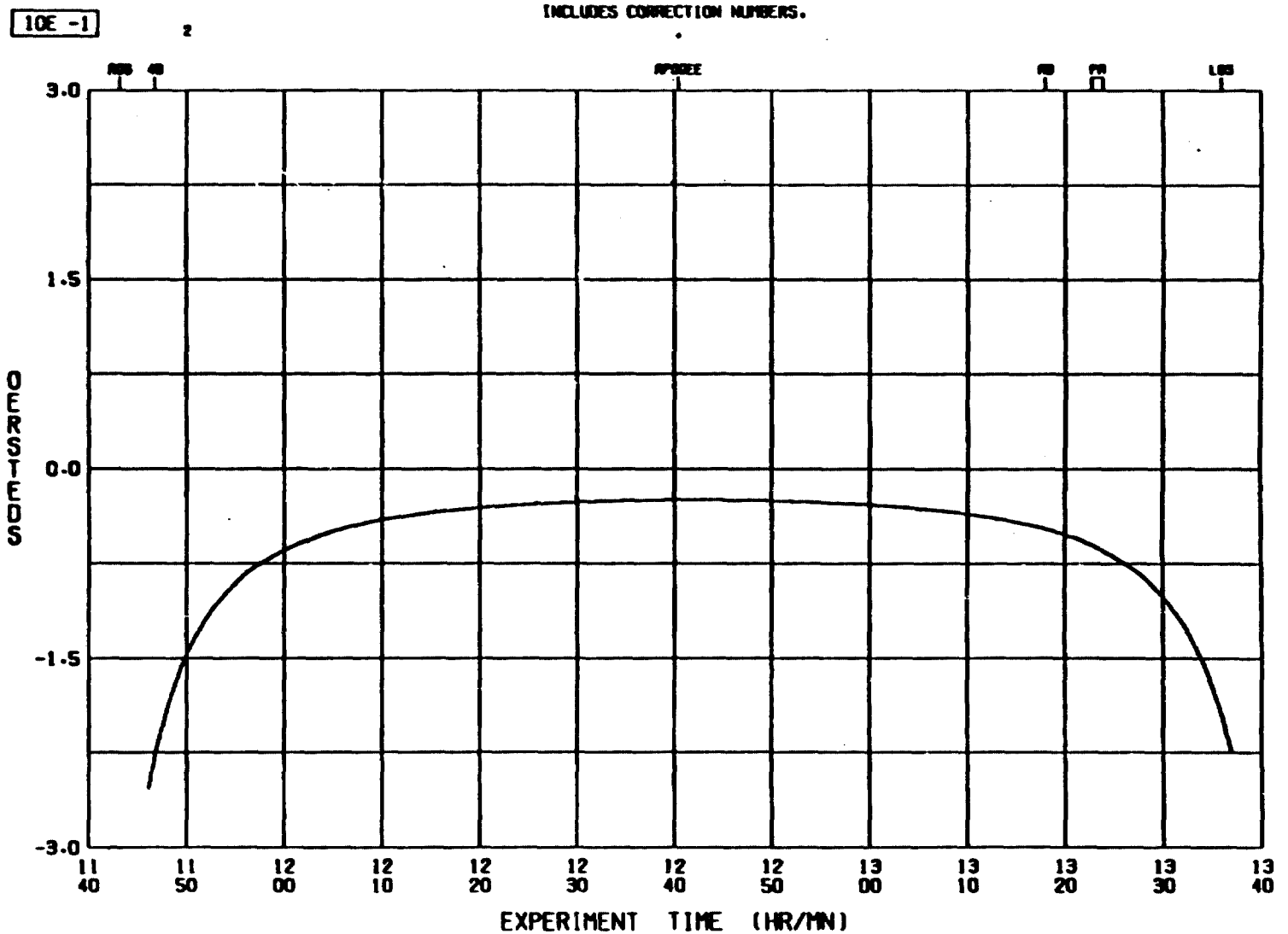

MAG FIELD (AXIAL) - FREQ CHANGE

INCLUDES CORRECTION NUMBERS.

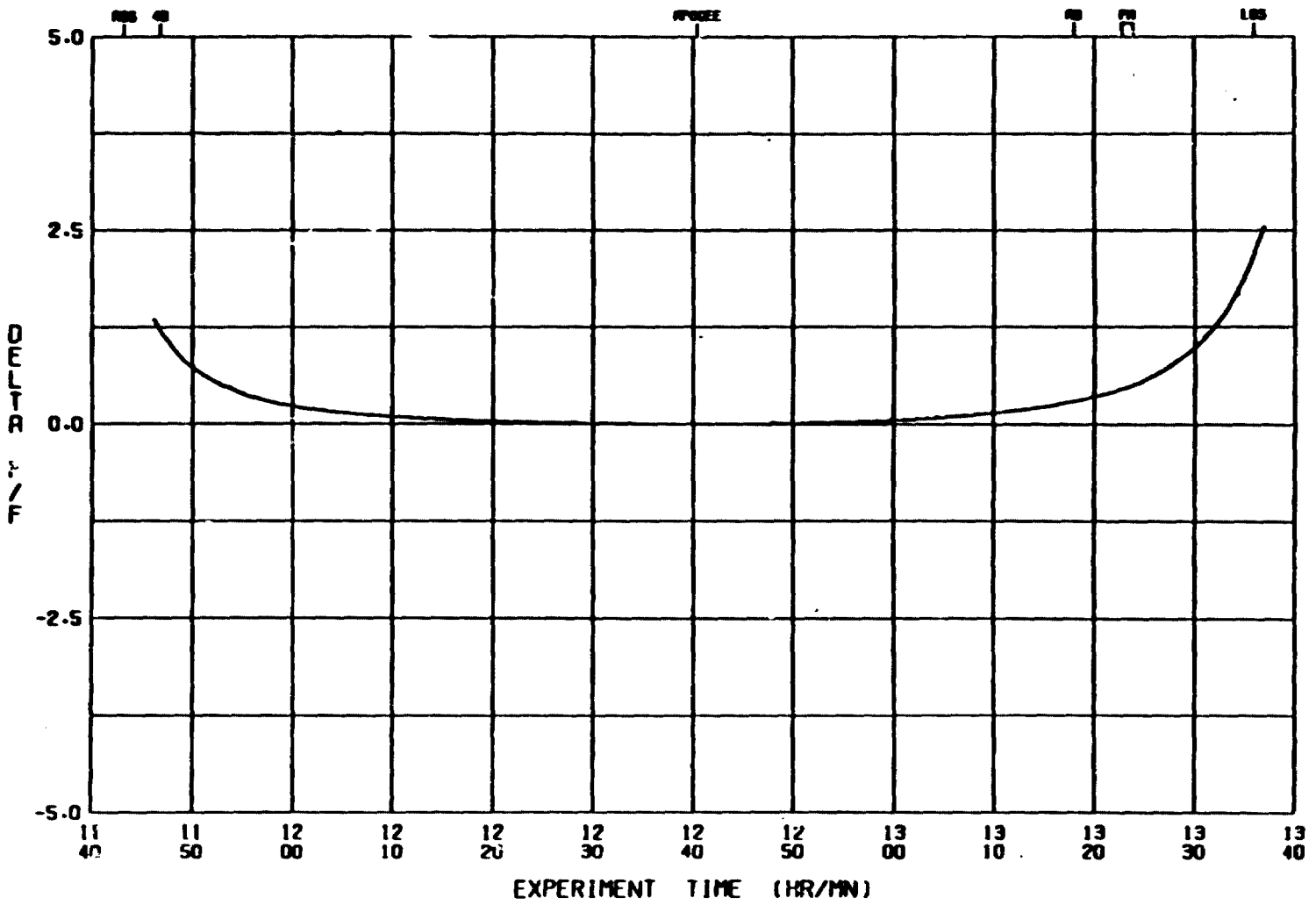

MAG FIELD (AXIAL) - PHASE CORRECTION

INCLUDES CORRECTION NUMBERS.

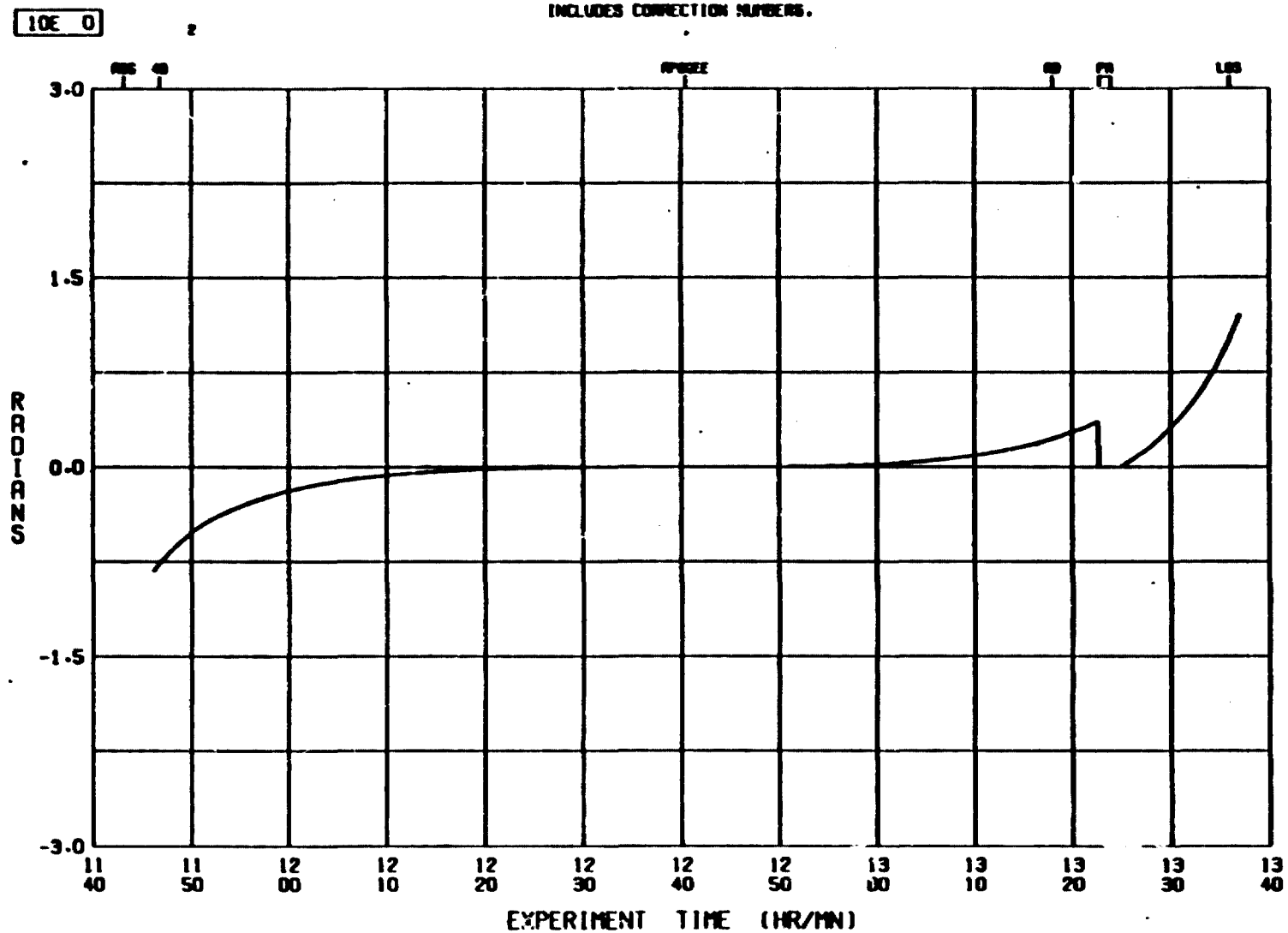

AFT OVEN HEATER

INCLUDES CORRECTION NUMBERS.

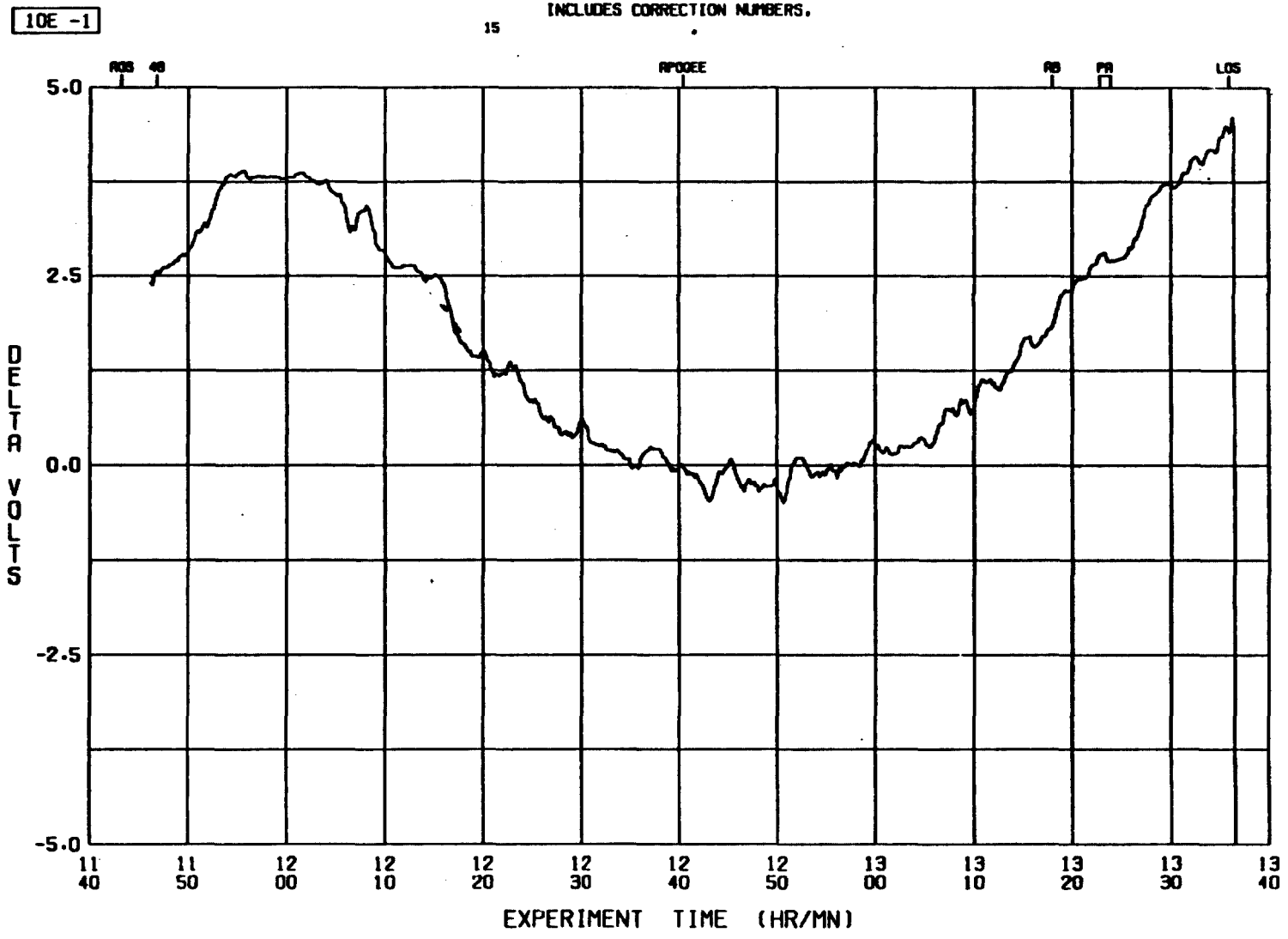

AFT OVEN HEATER - FREQ CHANGE

INCLUDES CORRECTION NUMBERS.

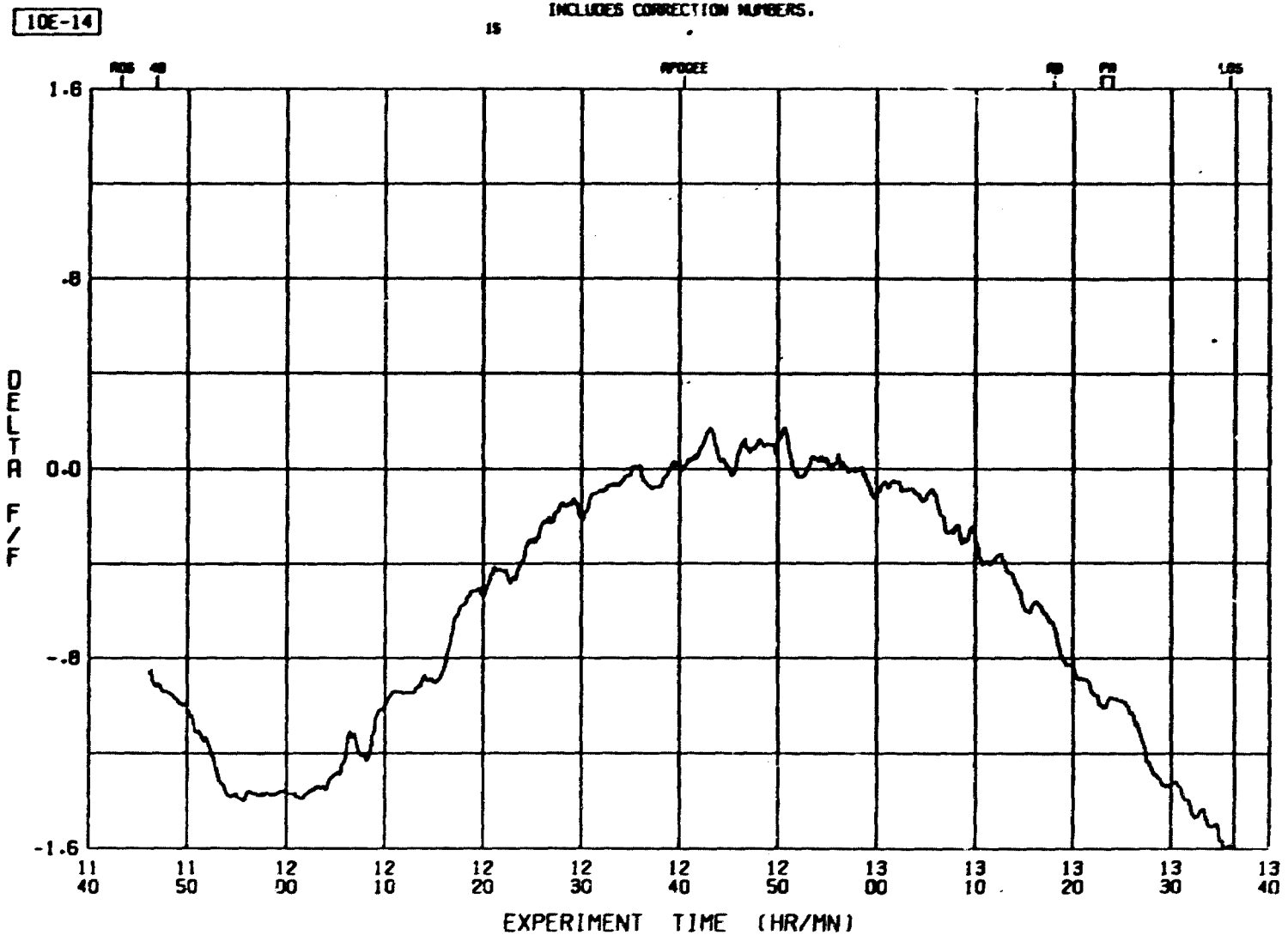

AFT OVEN HEATER - PHASE CORRECTION

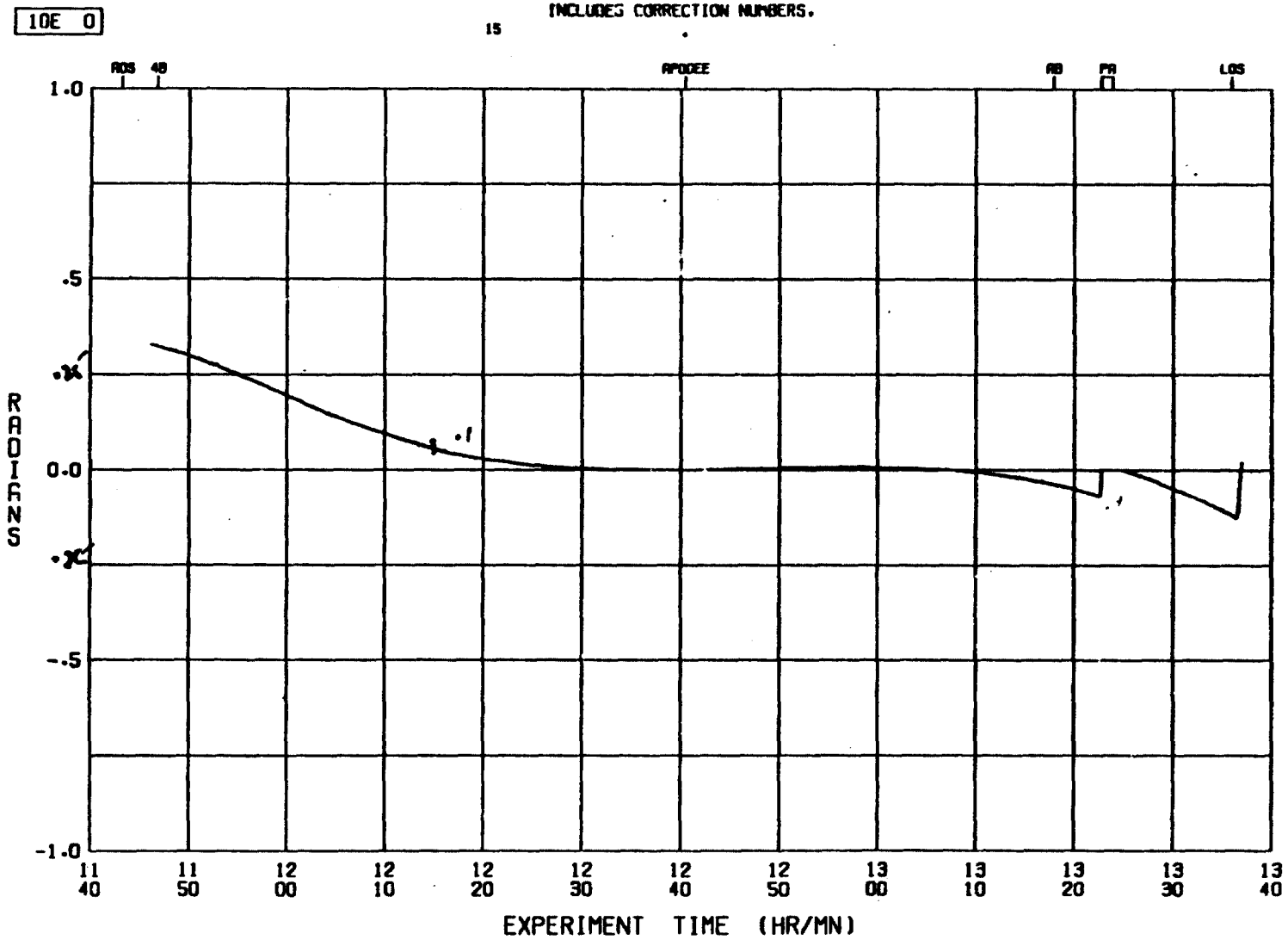

OUTER CAN PRESSURE

INCLUDES CORRECTION NUMBERS

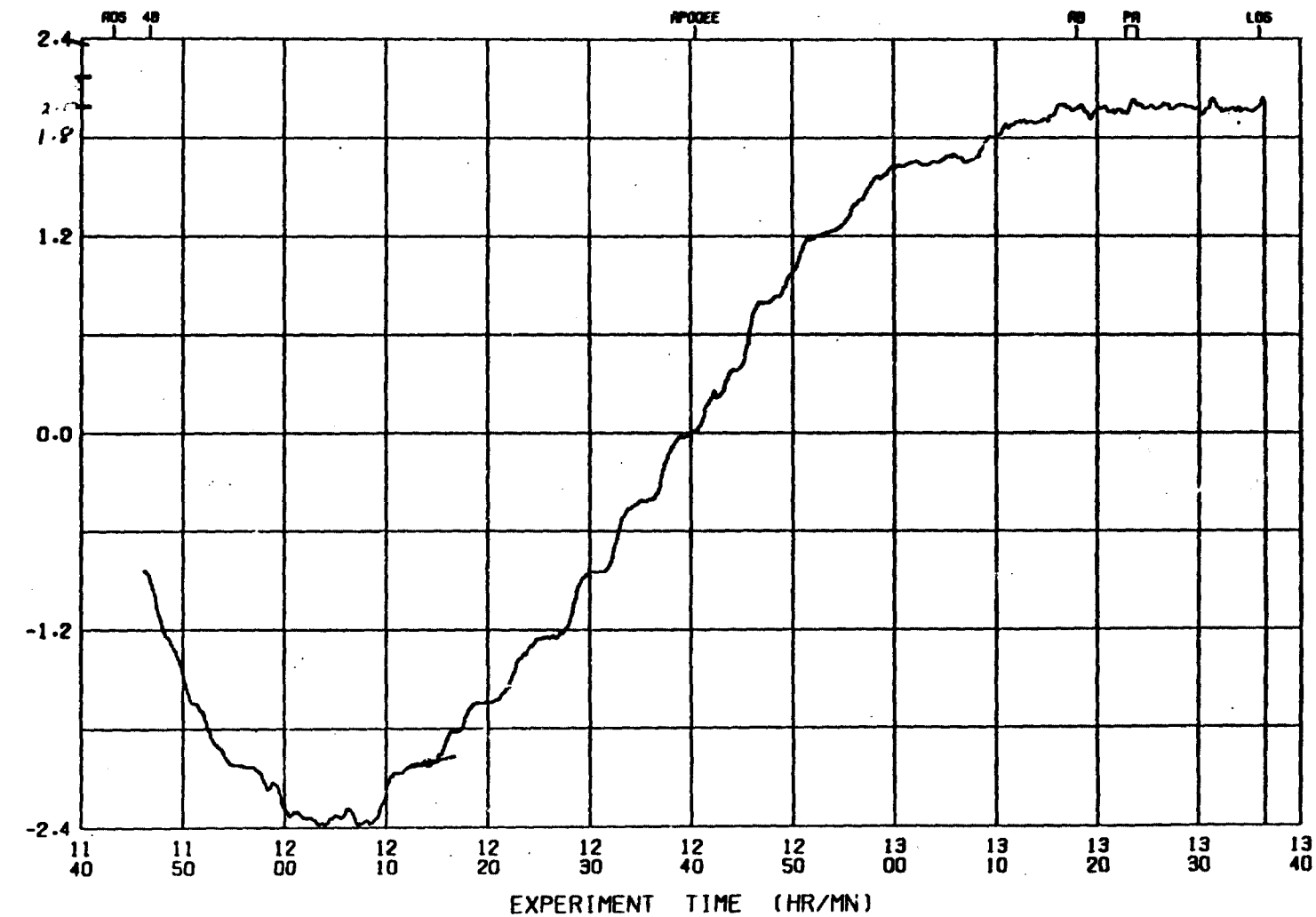

OUTER CAN PRESSURE -. FREQ CHANGE

INCLUDES CORRECTION NUMBERS

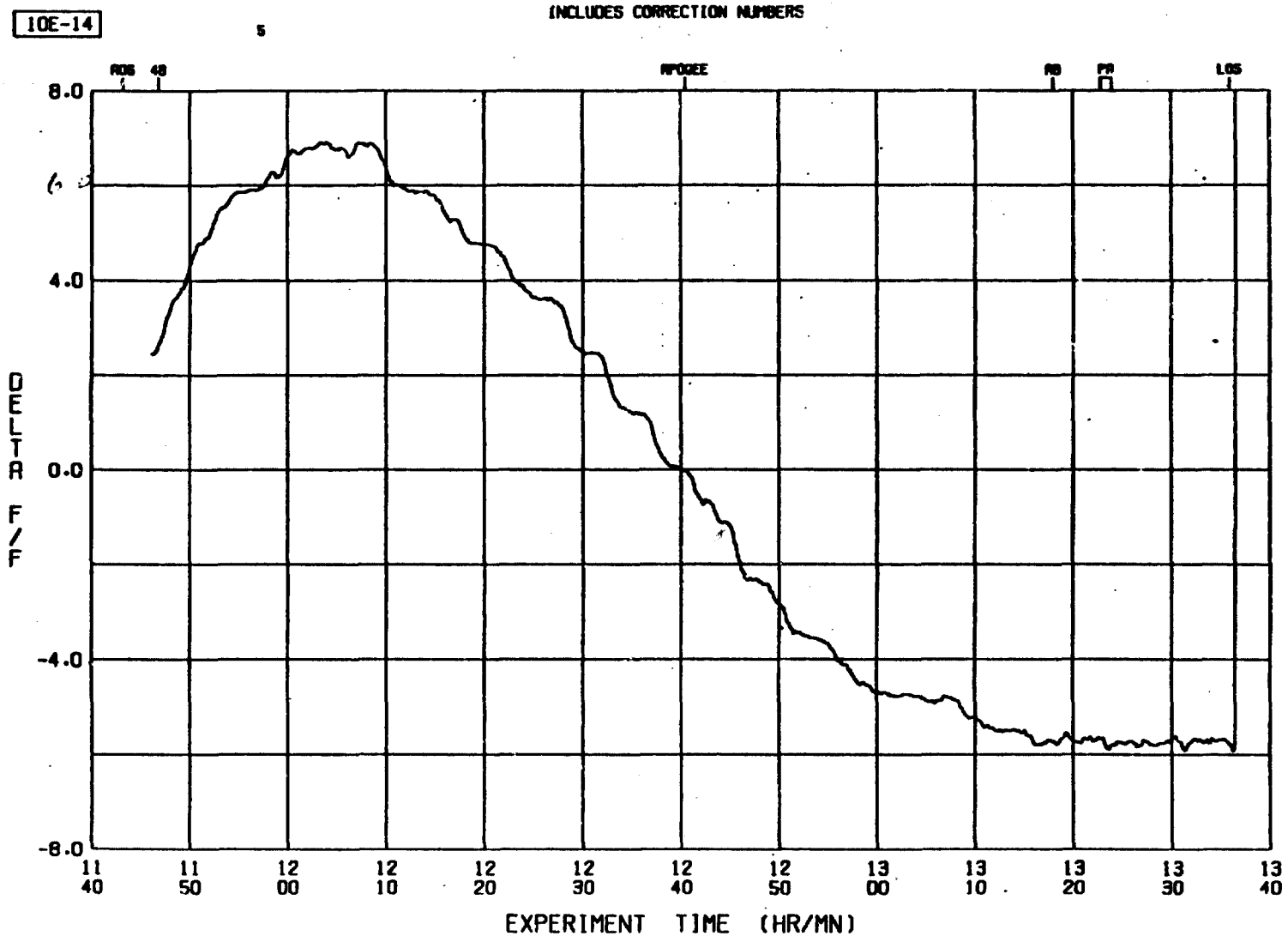

OUTER CAN PRESSURE - PHASE CORRECTION

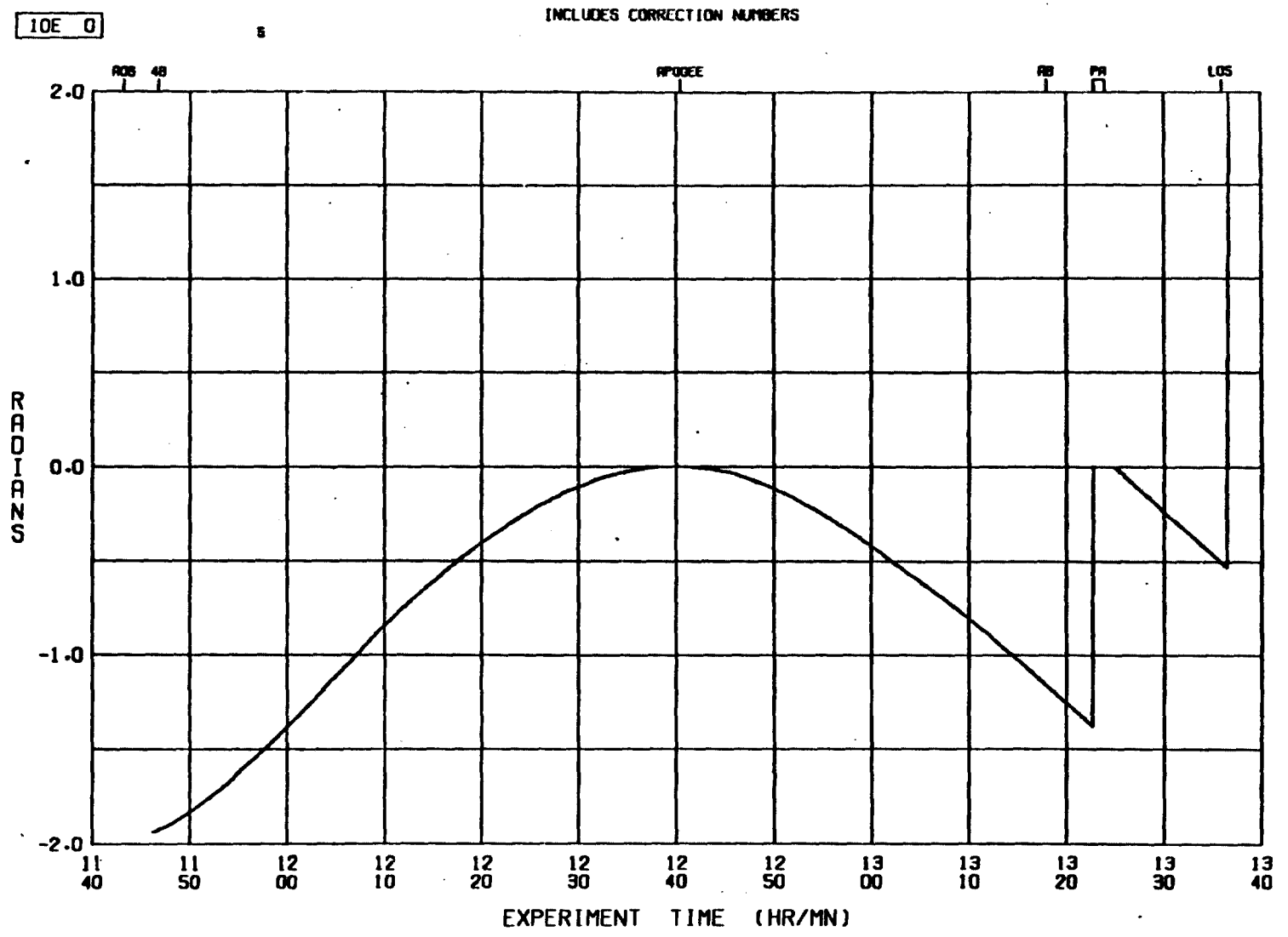

PROBE SPIN RATE

INCLUDES CORRECTION NUMBERS.

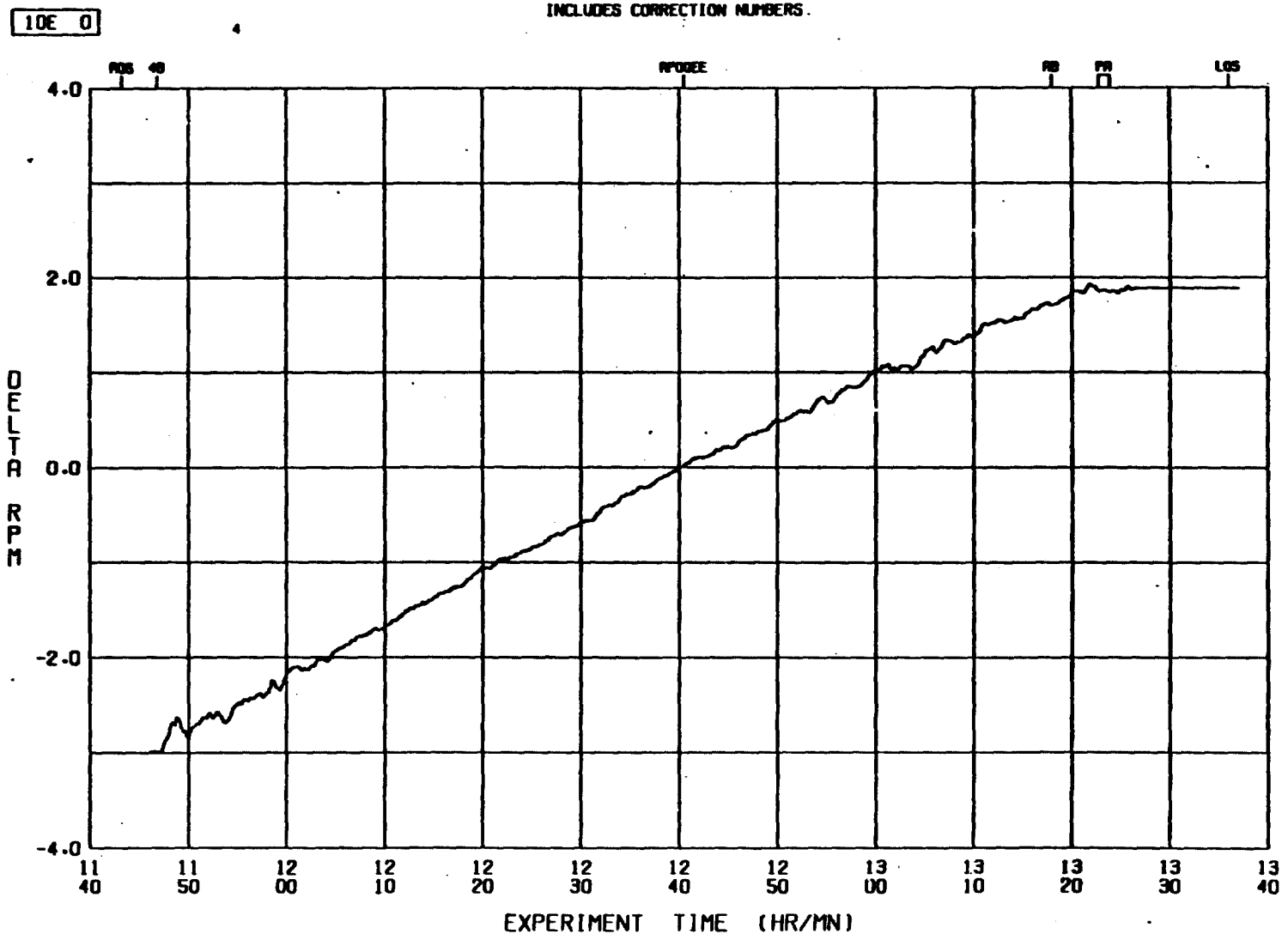

PROBE ROTATION - FREQ CHANGE

INCLUDES CORRECTION NUMBERS

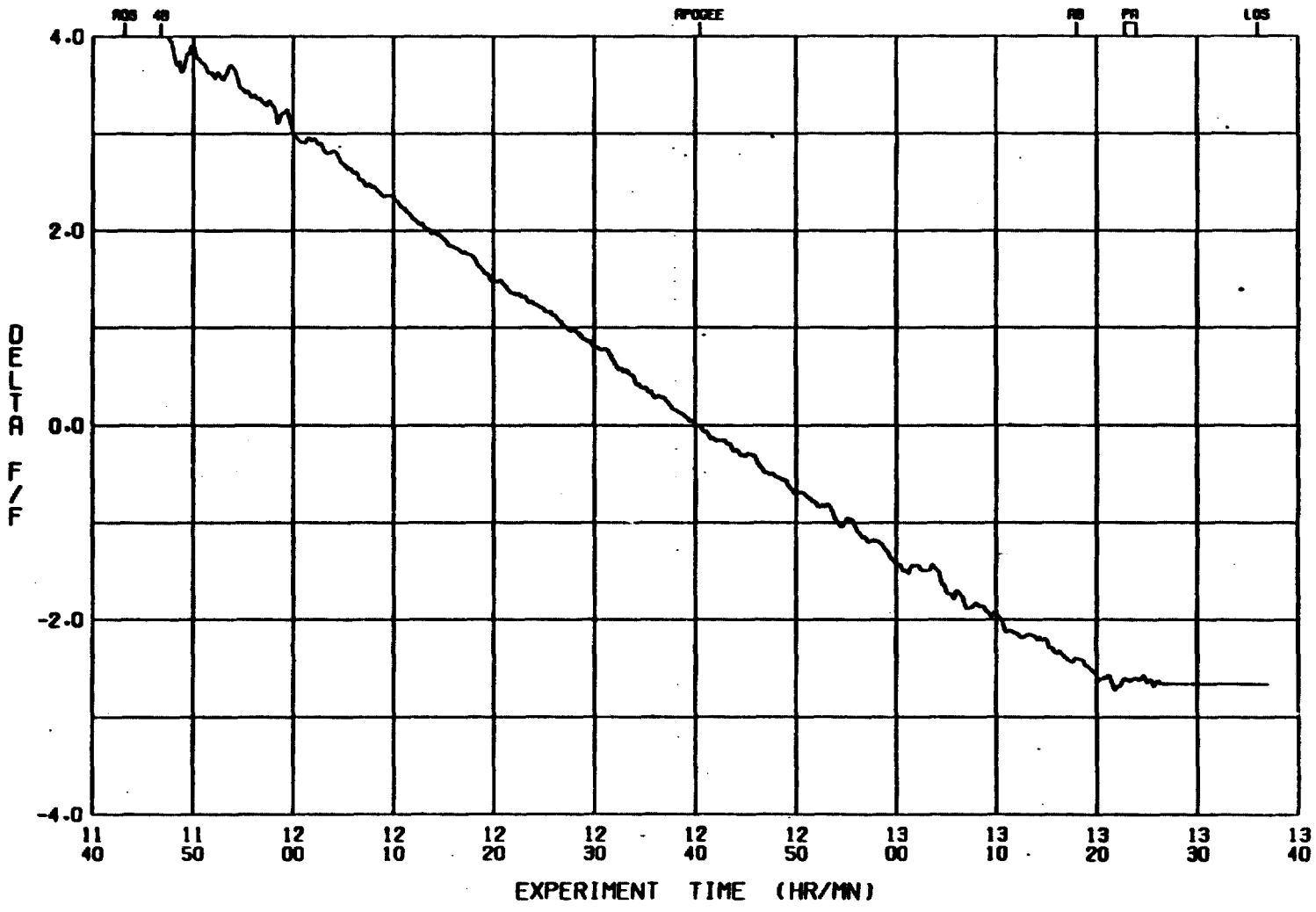

PROBE ROTATION - PHASE CORRECTION

INCLUDES CORRECTION NUMBERS.

10E 0

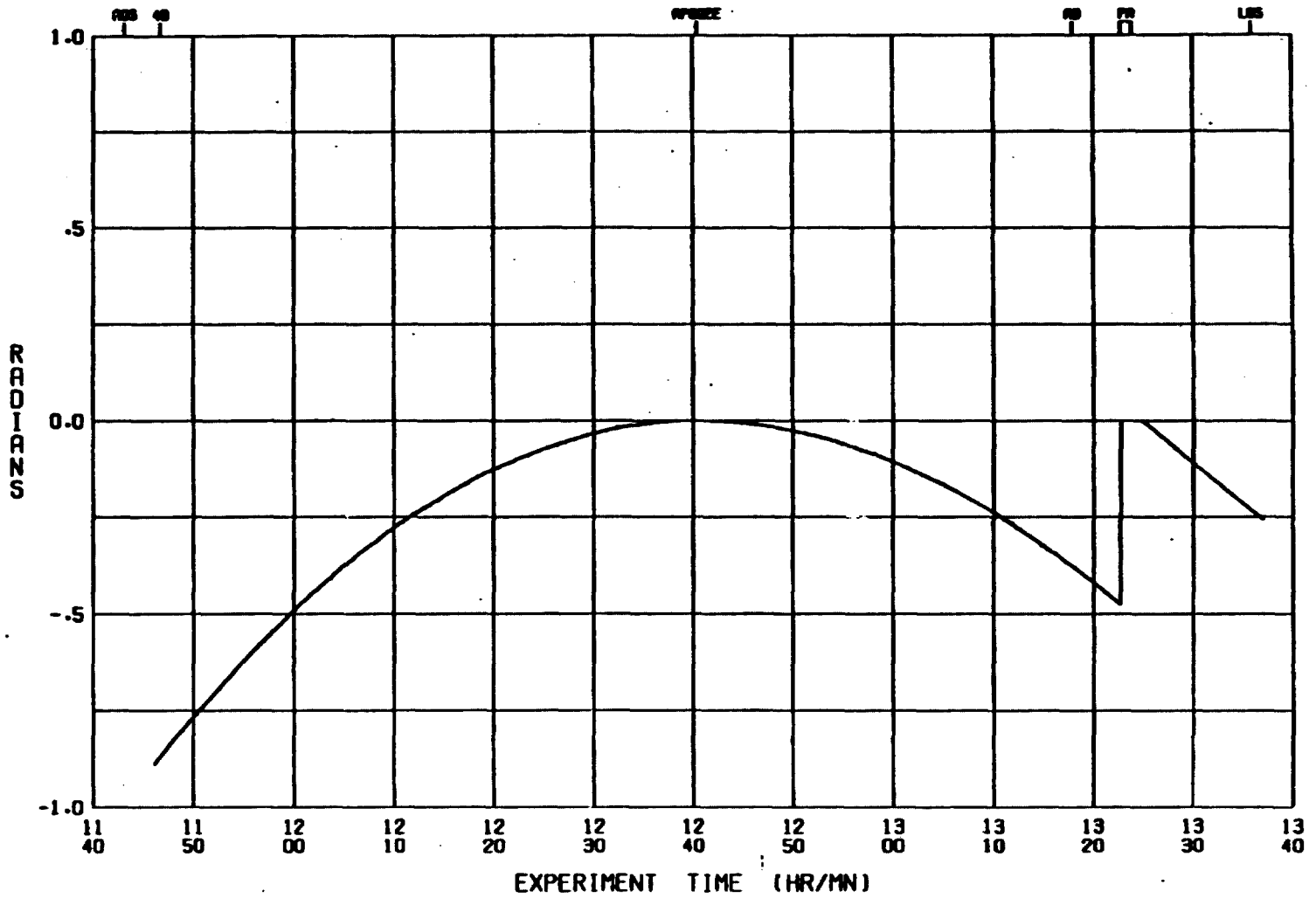

12/16/76
(18.36.25)

RECEIVER 1 AGC

INCLUDES CORRECTION NUMBERS.

91

10E 1

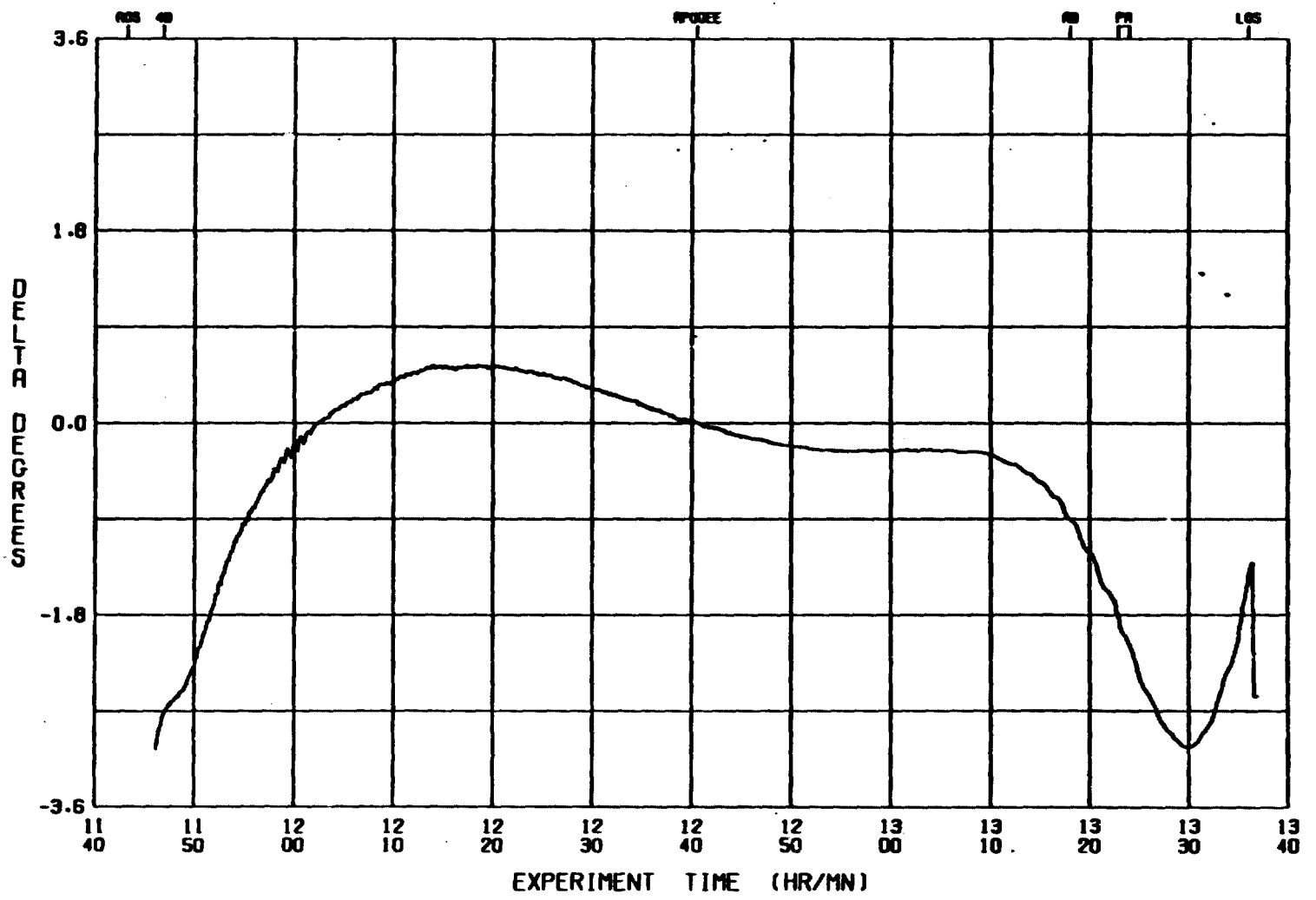

RECEIVER 1 AGC - PHASE CORRECTION

INCLUDES CORRECTION NUMBERS.

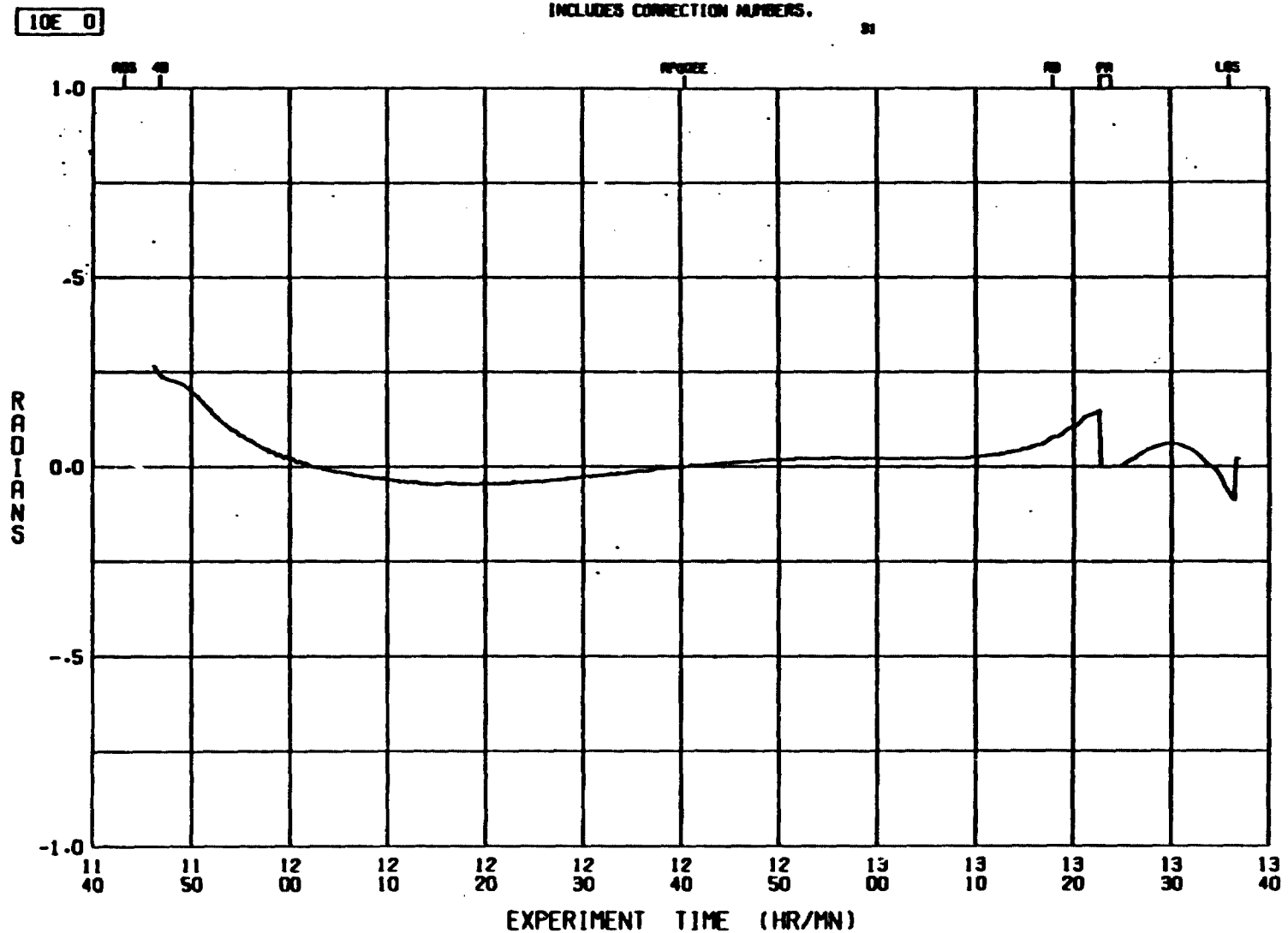

01/13/77
(10.41.22)

RECEIVER 2 AGC

INCLUDES CORRECTION NUMBERS.

32

10E 1

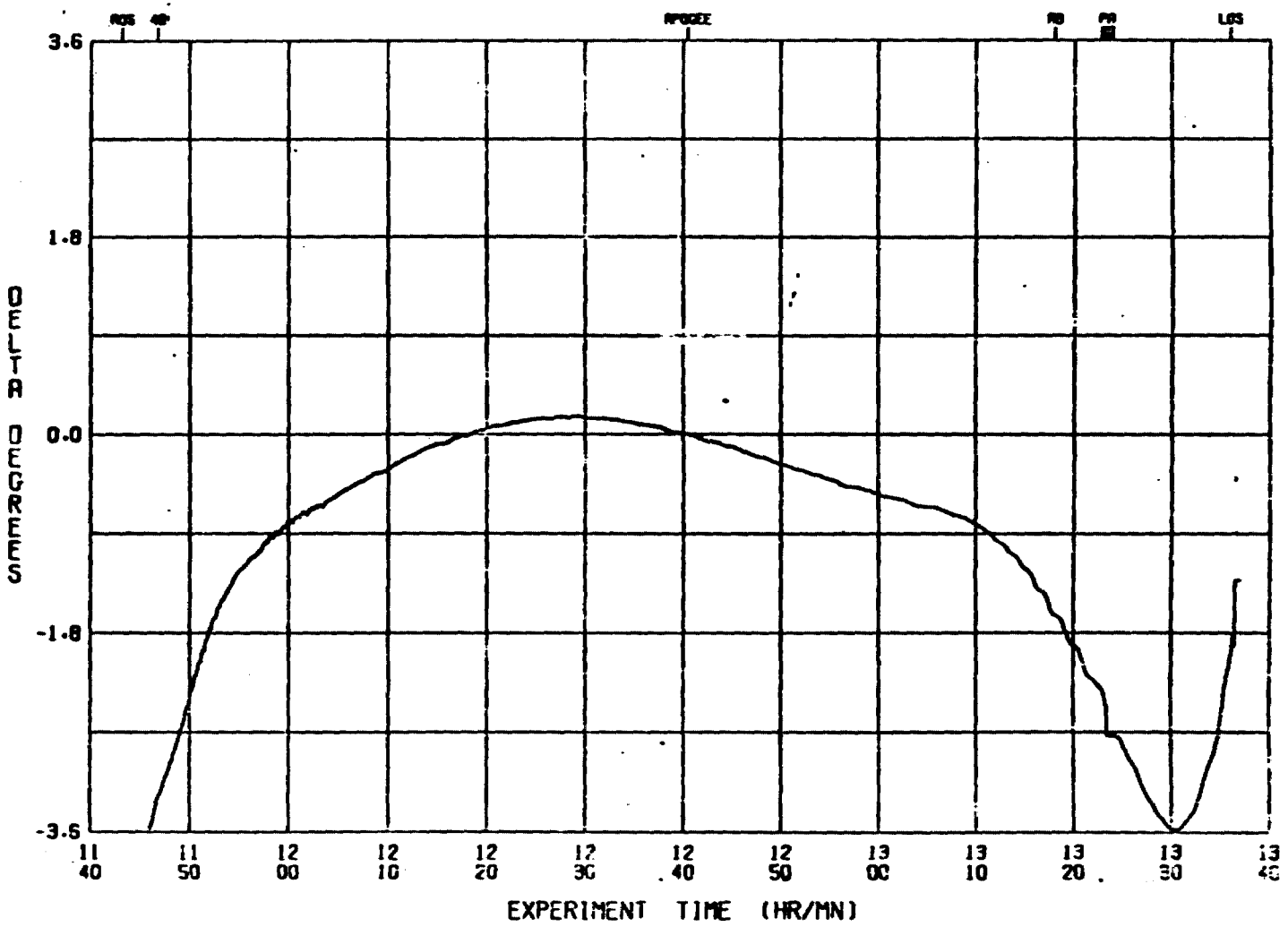

RECEIVER 2 AGC - PHASE CORRECTION

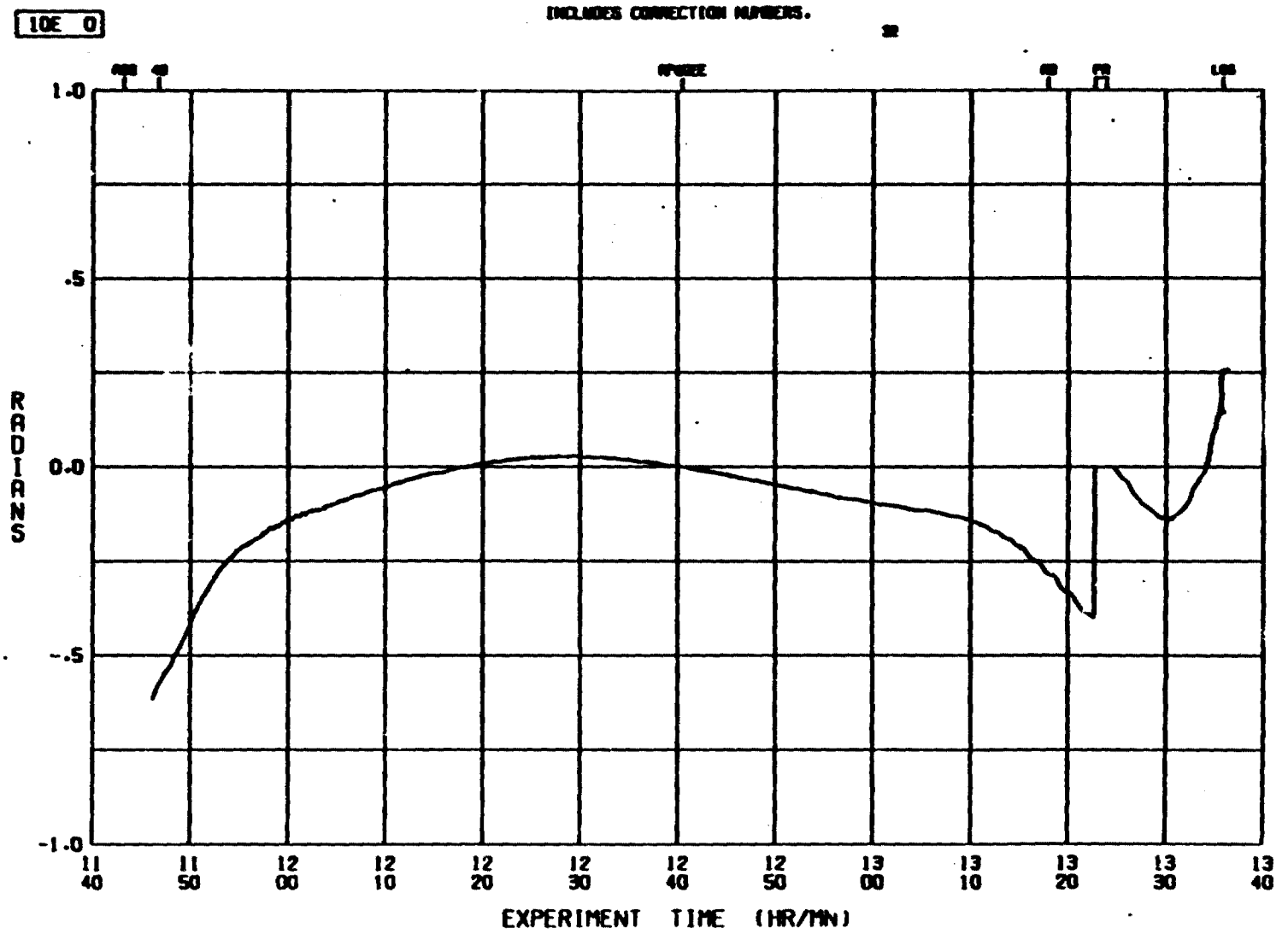

12/17/76
[16.43.01]

TRANSPONDER AGC

INCLUDES CORRECTION NUMBERS.

10E 1

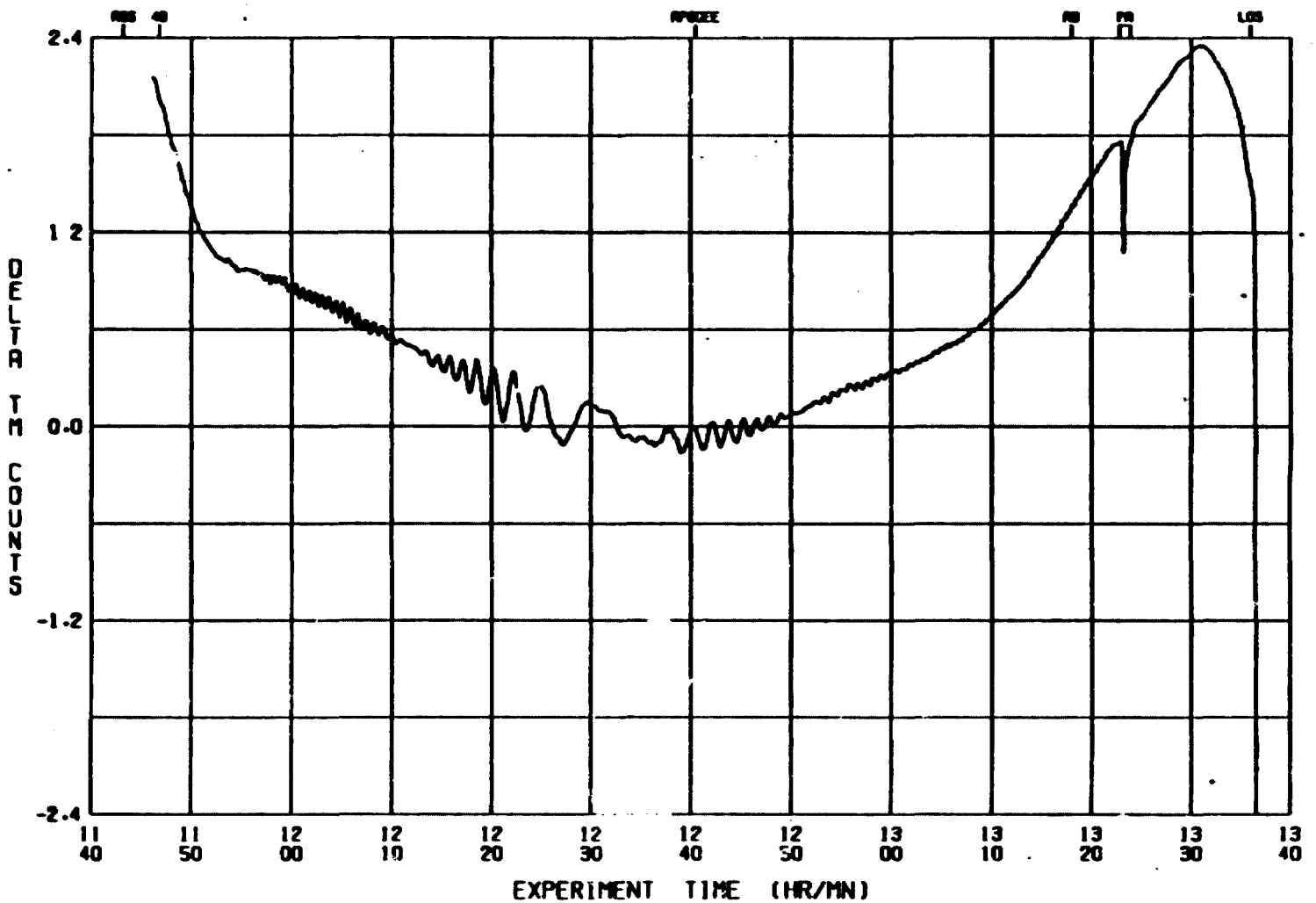

TRANSPONDER AGC - PHASE CORRECTION

INCLUDES CORRECTION NUMBERS.

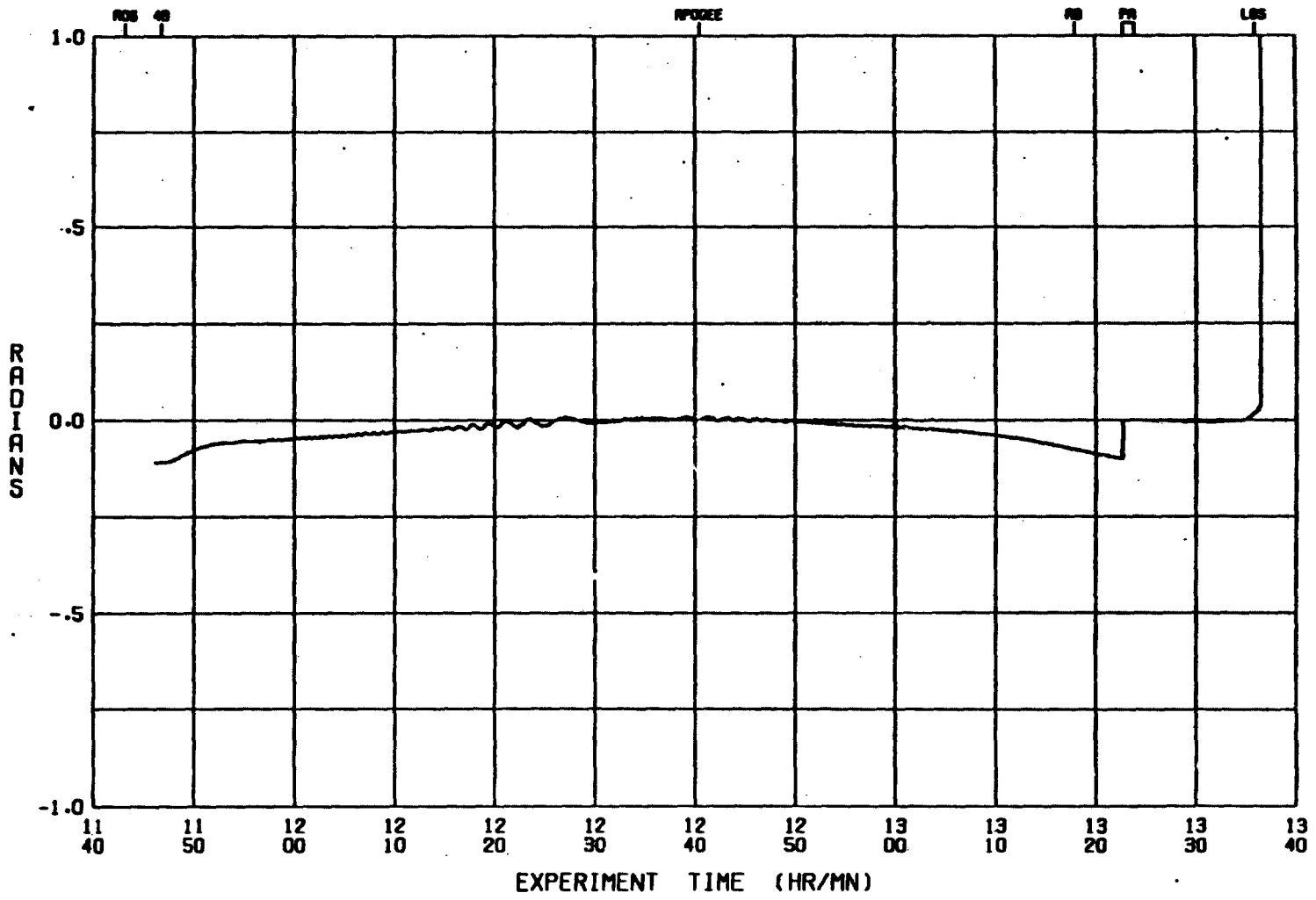

TRANSLATOR AGC VOLTAGE - CORRECTED PER GRD 78

2/16/77
17:03:53

INCLUDES CORRECTION NUMBERS.

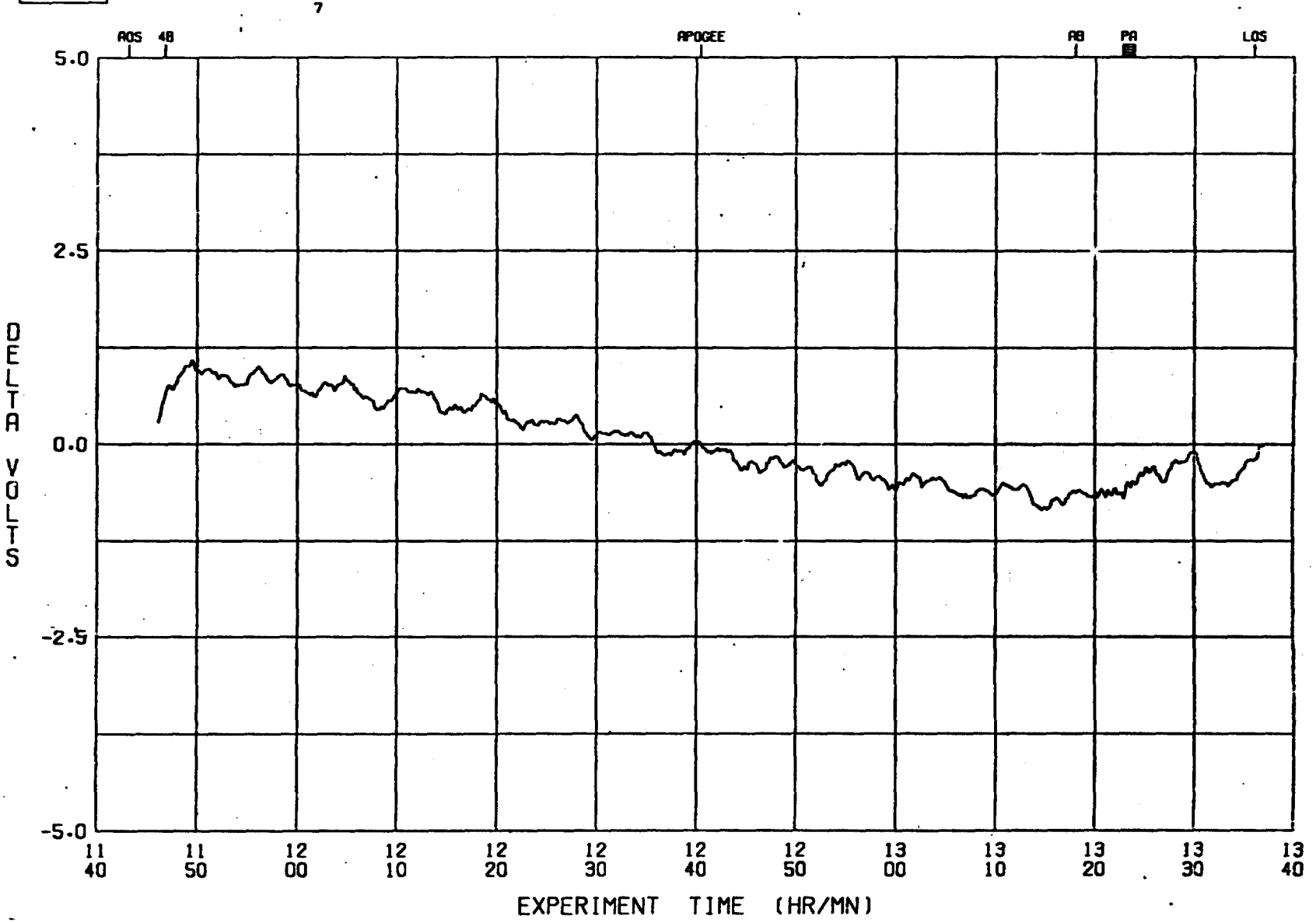

PHASE SHIFT RESULTING FROM

TRANSLATOR AGC VOLTAGE - CORRECTED PER GRD 78

INCLUDES CORRECTION NUMBERS.

2/15/77
17:03:53

10E 0

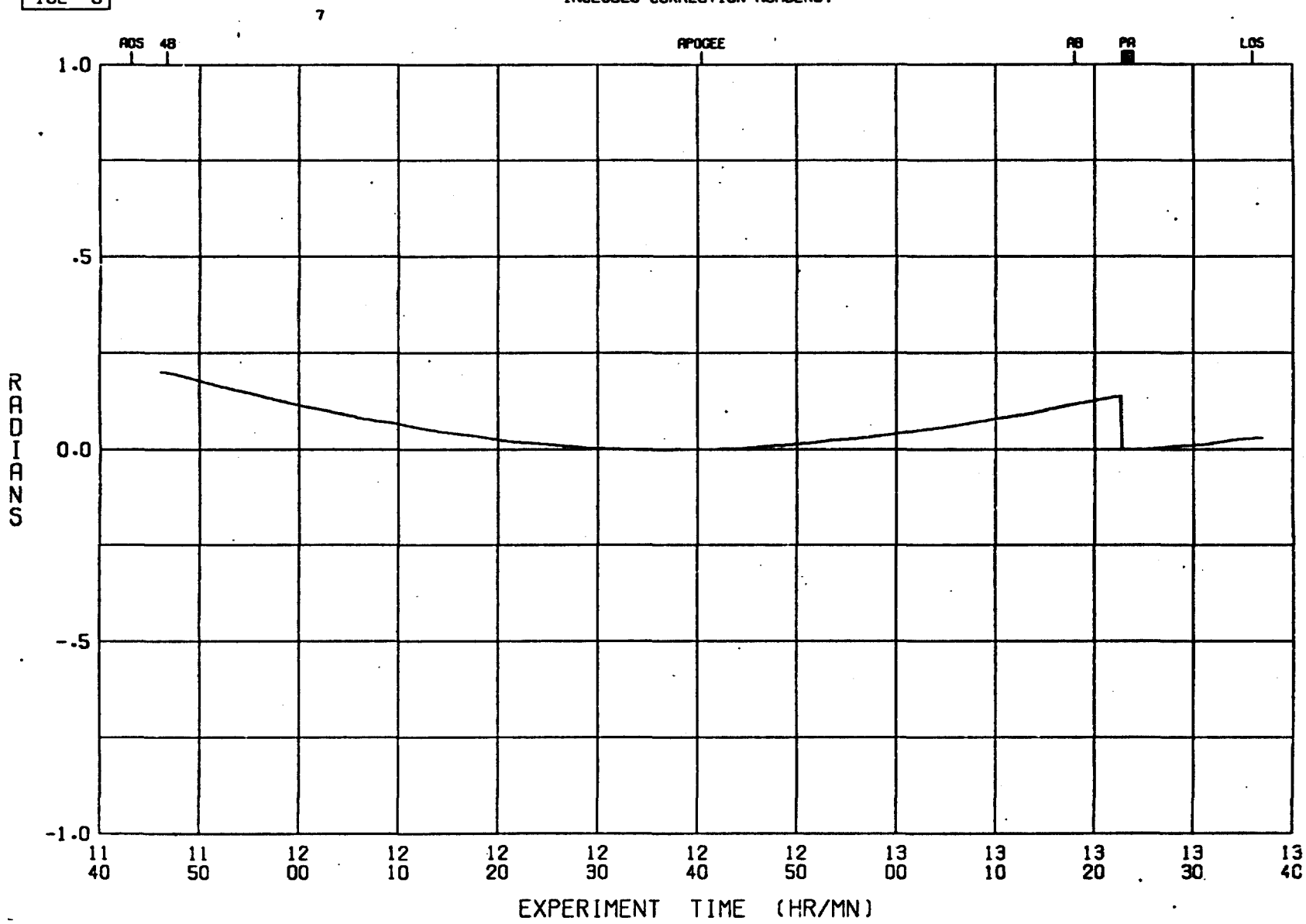

BOILER INTERFACE TEMPERATURE

12/16/76
(18.27.06)

INCLUDES CORRECTION NUMBERS.

10E 1

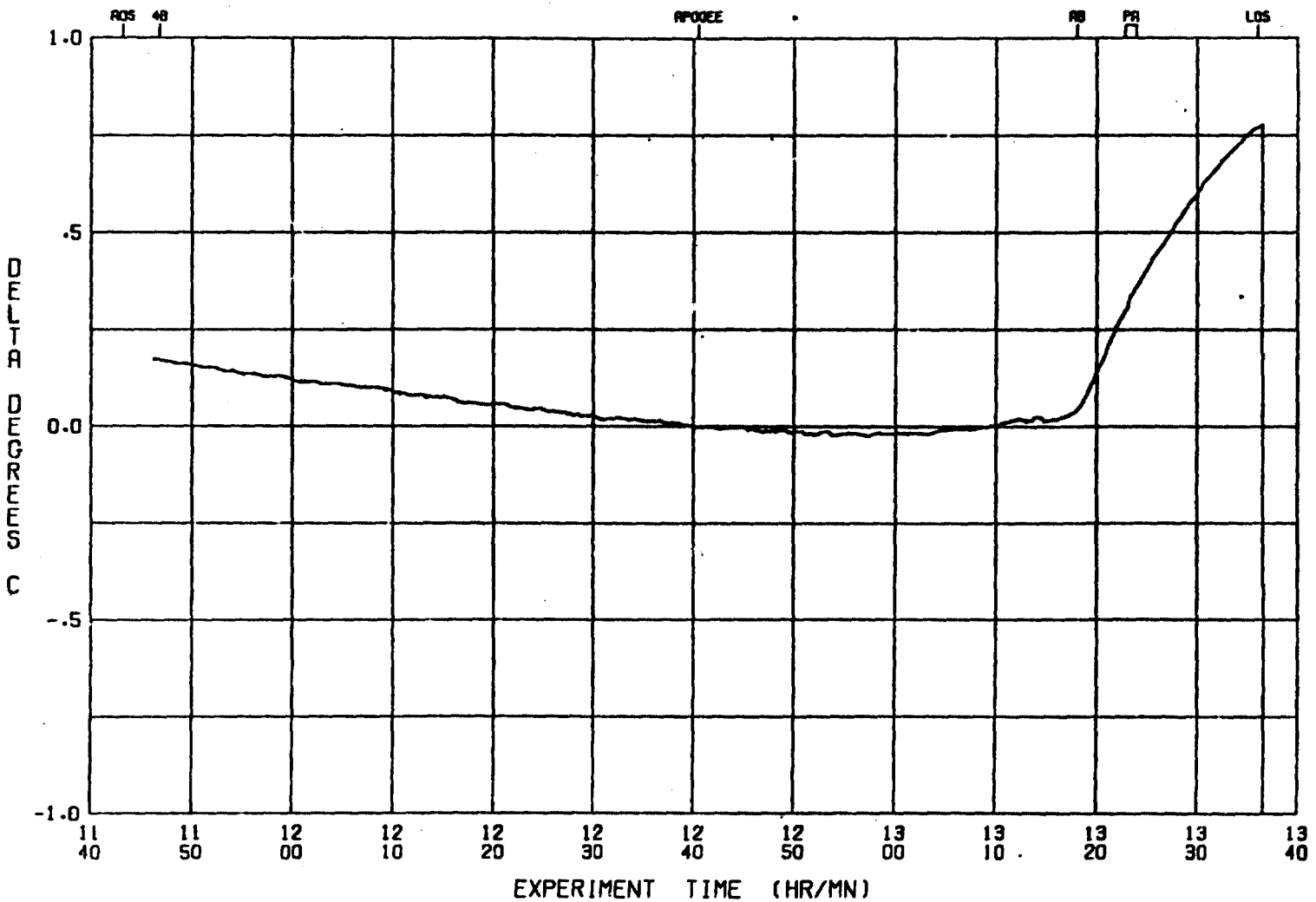

12/16/76
(18.27.06)

TRANSPONDER TEMPERATURE - PHASE CORRECTION

INCLUDES CORRECTION NUMBERS.

10E 0

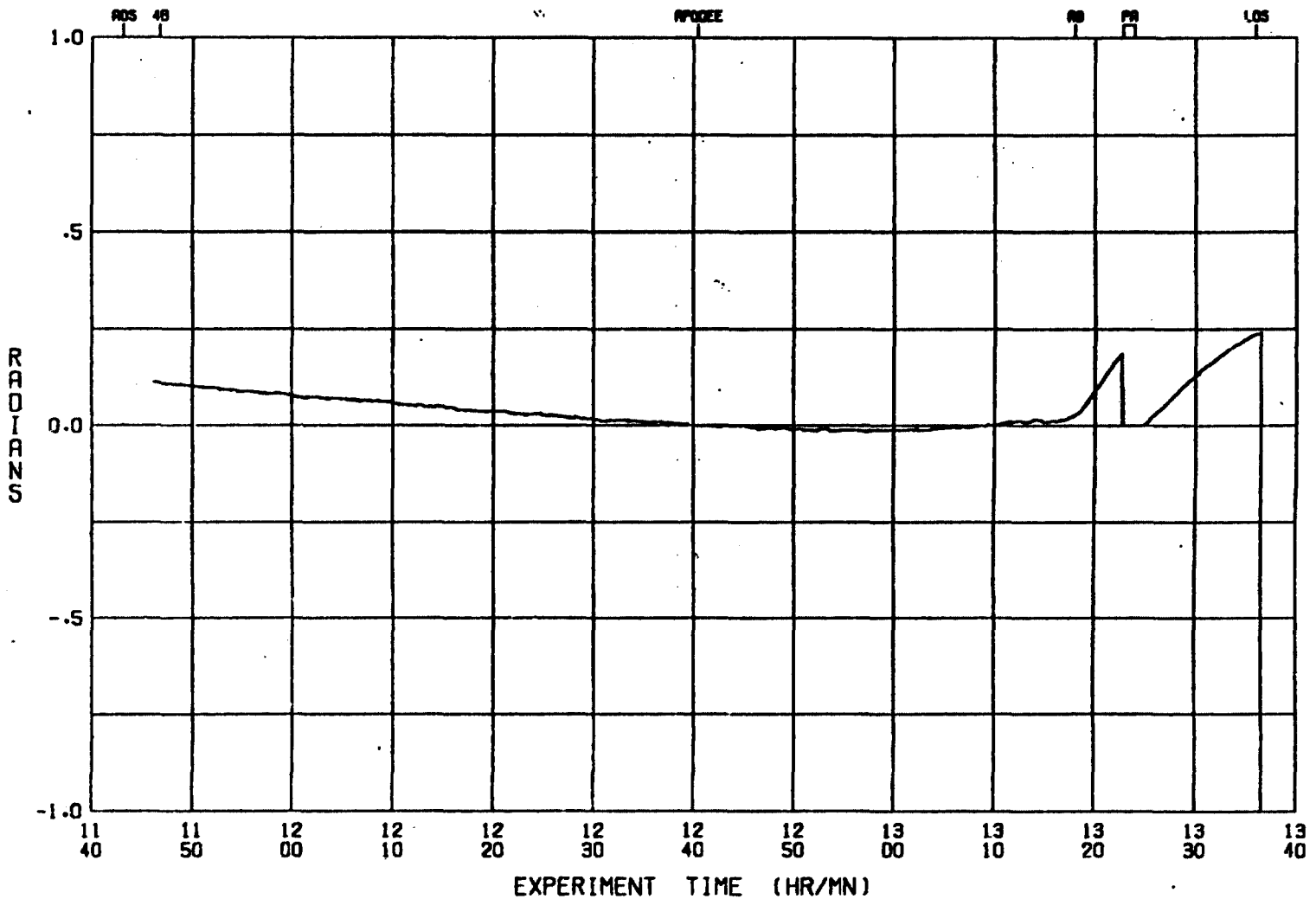

APPENDIX III

DOPPLER CANCELLING SYSTEM PERFORMANCE STATISTICS

APPENDIX III

DOPPLER CANCELLING SYSTEM PERFORMANCE STATISTICS

The effectiveness of the doppler cancelling system can be illustrated by observing the short-term fluctuations in the one-way and two-way doppler data separately as they are generated in mixers M1 and M2 of Figure 8. By computing the residual phase signature from the predicted cycle counts for the one-way and two-way data, using the trajectory we can remove the gross first-order doppler effects and look at the rapid fluctuations. Figure III-1 shows the one-way and two-way residuals plotted versus time. These data residuals include predictions of the relativistic effects and lightime refraction but do not include the known systematic effects given in Figure 27. By digitally reconstructing the function of the analog doppler cancelling system and including the corrections we obtain very nearly the same signature in the residual phase as shown in Figure 30. It is worth noting that, in this case, the one- and two-way data are not obtained at the same time. As mentioned earlier the recording of accumulated phase in the one- and two-way channels alternated every 0.2 sec. During this interval the spinning probe's orientation changed one third of a turn. Evidence of a slight asymmetry of the antenna pattern about the spin axis is shown in Figures 18 and 19 where the null combination of redshift and second-order doppler shows the rotational and nutational effects. In the nearly simultaneous cancellation from the analog system, where the cancellation was limited only by the light time between the earth and probe ($r < 0.03$ sec), this was almost completely removed. However for the 0.1-sec delay between adjacent one- and two-way readings, the rotation effect is not cancelled, and is the main reason for the sawtooth behavior in the phase signature.

Some insight may be available in the residuals after the uplink interruption. We notice that both the one- and two-way data show rather violent behavior, which is well cancelled before the break but appears to be imperfectly cancelled after. Propagation effects are not likely to be the cause. However, wherever the signal paths are functionally separated in the transmitter and receiver system there is an opportunity for incomplete cancellation since only the transmitter was interrupted and thermal effects in the antenna feed beyond the phase sampling point could occur. Further investigation in this might prove useful.

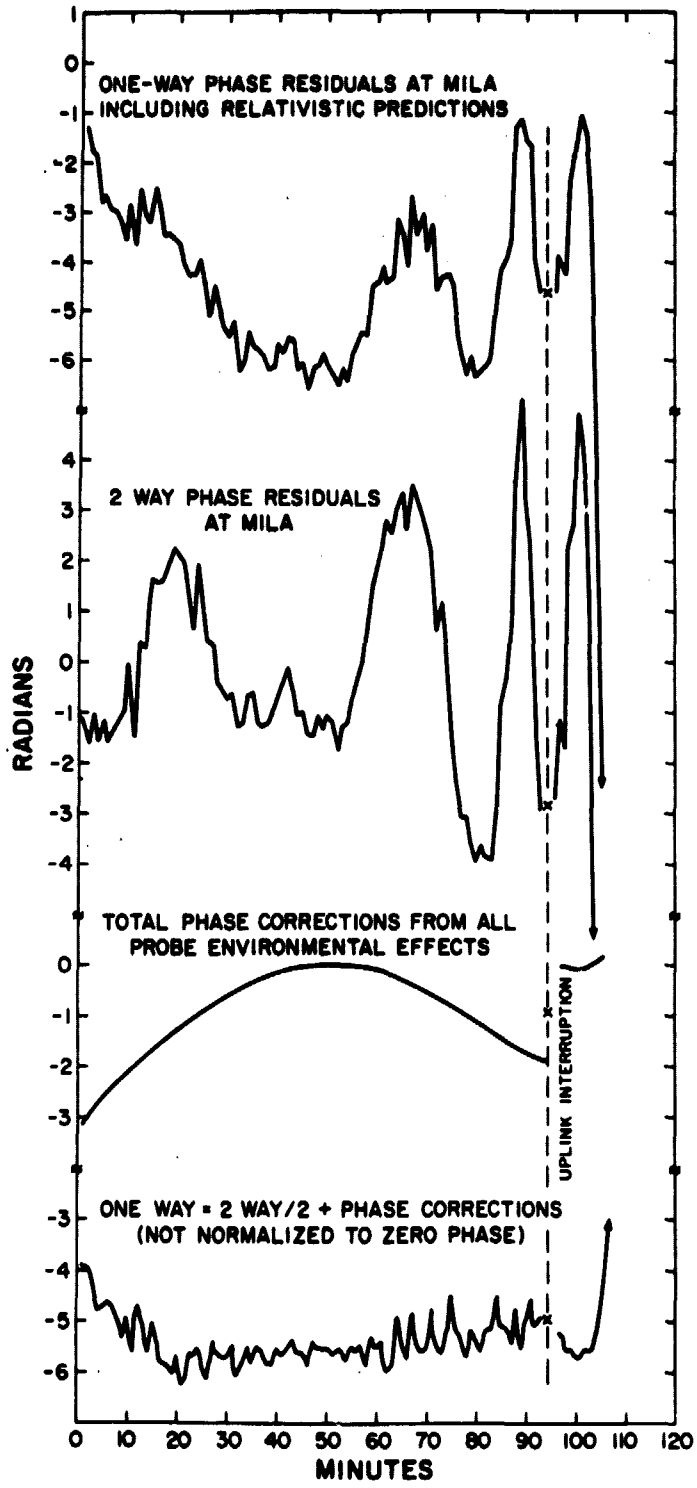

Figure III-1. Illustration of doppler cancelling system performance.

Statistical representations of the uncancelled one-way data, the cancelled data, and the data obtained between the two reference oscillators at the earth station are of interest, partly to evaluate the effectiveness of the cancellation method, and to assure us that the frequency stability of the ground-based oscillators was as expected. This information is contained in the Allan variance plots shown in Figure III-2, which were made using data taken during the interval 1215–1322 GMT for the probe versus the ground station control maser, P7 (VLG-11 S/N7) and for P7 vs. P6 (VLG-11 S/N6) directly at the ground station.

The statistics for both comparisons are made in the same way; the number of samples used is shown with the statistic. Relative frequency measurements between the ground masers were made at 0.83-sec intervals while the probe vs. ground maser data are taken in terms of phase measurements every second. Comparisons for time intervals less than 0.83 sec are not possible, however ample data have previously been taken between ground masers for shorter time intervals, as shown in Figure 5, which describes the performance of ground masers. In Figure 5 the statistics are given for measurements made between exactly similar maser oscillators and their performance, given by the variance, is attributed equally to each maser by dividing the comparison variance by $\sqrt{2}$. The noise bandwidth of the measuring system is 1 Hz for the probe comparison whereas it is 6 Hz for the ground masers. This has little effect for averaging times longer than 100 sec, however for averaging times of about 1 sec the additive white phase noise in the maser receiver system dominates and the contribution of this noise to the variance varies as the square root of the noise bandwidth. The behavior expected at 1 Hz-noise bandwidth for the P6-P7 comparison is shown dotted. This line is a factor $\sqrt{2/6}$ below the level shown in Figure 5 at $\tau = 1$ sec.

From Figure III-2 we conclude that the doppler cancelling system contributed very little noise and that the maser instability is the dominant source of inaccuracy in the experiment.

A study of the noise spectral characteristics in the one-way data is given in the following memorandum from J.D. Anderson and A.S. Liu of the Jet Propulsion Laboratories.

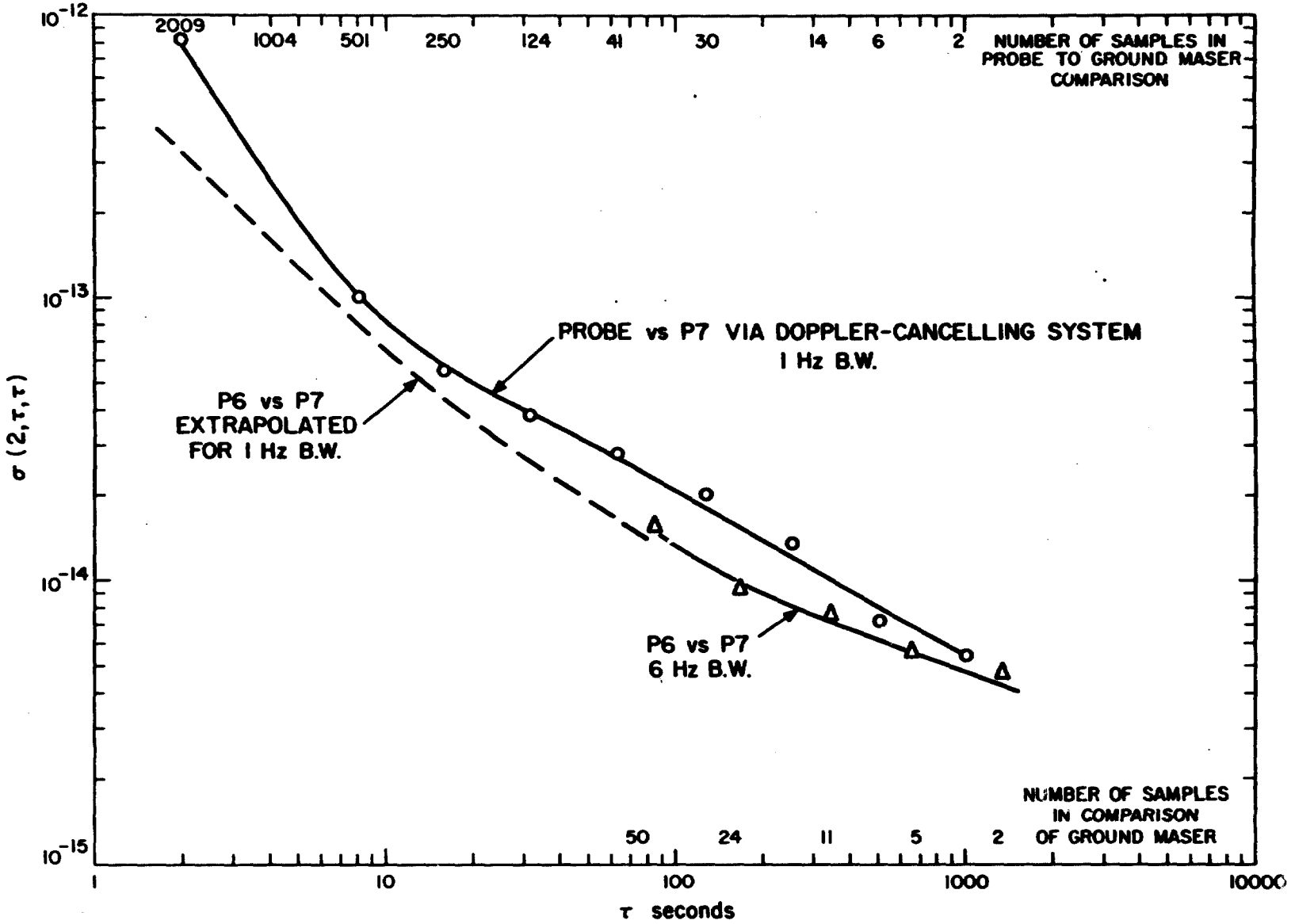

Figure III-2. Probe maser vs. P7 (ground maser) and P6 vs. P7 (ground maser comparison) during same time interval. Allan variance data taken during flight from 1215 to 1322 GMT, June 18, 1976.

JET PROPULSION LABORATORY

INTEROFFICE MEMORANDUM

315.5.212

21 May 1979

TO: Distribution

FROM: J. D. Anderson/A. S. Liu

SUBJECT: Noise Characteristics of One-Way S-Band Data from the Gravitational Redshift Space-Probe Experiment

Summary

One-way and two-way Doppler data from the 1976 gravitational redshift space-probe experiment have been sent to us by R. F. C. Vessot of the Smithsonian Astrophysical Observatory (SAO). Our determination of the trajectory of the Scout D rocket trajectory from the two-way phase data have been described elsewhere (Liu et al, EM 314-187, 7 May 1979). This memo describes some "quick-look" analysis of the one-way data. Power spectra in phase and frequency are generated by fast Fourier transform (FFT), and the Allan variance for the phase residuals is computed. For Fourier frequencies less than 10^{-2} Hz we find that the power spectrum increases with lower frequency, but because of the limited length of the data record (64 min) it is not possible to determine the precise powerlaw dependence on frequency. If a Kolmogorov spectrum is assumed, the phase spectrum obeys the following law.

$$S_\phi(f) = 263 \left(\frac{f}{0.001}\right)^{-2.6} \text{ radians}^2/\text{Hz}$$

An independent calculation of the Allan variance from one-way phase residuals yields:

$$\sigma_y(\tau) = \frac{5.3 \times 10^{-12}}{\tau^{\frac{1}{2}}}$$

For Fourier frequencies greater than 10^{-2} Hz the spectrum is representative of white phase noise ($S_\phi = 0.07$ radians^2/Hz). The spectrum of fractional frequency variations can be fit quite well by the following law.

$$S_y(f) = (6.1 \times 10^{-21}) f^2 \quad (f > 10^{-2} \text{ Hz})$$

and the associated Allan variance is given by

$$\sigma_y(\tau) = \frac{1.5 \times 10^{-11}}{\tau}$$

This is about one order of magnitude too large for hydrogen maser system noise, and may be the result of the aliasing of the payload spin ($\approx$ 116 rpm) in the spectrum, or it could be caused by high frequency environmental noise in the troposphere or in the payload. We plan to investigate this problem in the future.

The Kolmogorov spectrum is roughly of the same size as that for the Viking S-band data at opposition (Armstrong, Estabrook, and Wahlquist, Sec. 328 IOM, April 17, 1979). However, because Viking has an S/X band radio system, it is possible to attribute most of the low frequency noise to plasma turbulance. In the case of the redshift space-probe, only S-band data are available, and so it is impossible to separate troposphere and ionosphere effects. The spectrum is made up of some unknown combination of ionospheric and tropospheric turbulance. However, an upper bound of $\sigma_y(1000\ s) = 1.7 \times 10^{-13}$ can be placed on tropospheric noise in the one-way space probe radio link, which has a hydrogen maser on both ends. Conditions at Goldstone, where the air is dryer and where elevation angles are higher (redshift data are on the order of 59°), should result in considerably less tropospheric noise than indicated by our upper bound from the space probe.

Power Spectrum

First, the best-fit trajectory from the two-way phase data was passed through the one-way phase data recorded at a 60 s sample. Then a quadratic polynomial was fit to the resulting one-way residuals to remove trends caused by a frequency bias and a frequency drift in the data. The resulting residuals are shown in Figure 1. Next, the first 64 residuals were submitted to an FFT and the power spectrum was calculated. In addition 128 one-way phase data at a one second sample near the beginning of the trajectory were analyzed in the same way. The combined high frequency ($1/128 < f < \frac{1}{2}$) and low frequency ($1/3840 < f < 1/120$) spectrum from the two sets of residuals is shown in Figure 2. It is our intention to compute a spectrum from a long record of one second data in the future.

The spectrum can be fit reasonably well by the following model

$$S_\phi(f) = 263\left(\frac{f}{.001}\right)^{-2.6} + 0.070 \quad (\text{radians}^2/\text{Hz})$$

The constant term in this model represents white phase noise. The standard deviation for the phase noise can be evaluated from the formula

$$\sigma_\phi^2 = \int_0^{f_N} S_\phi(f)\, df$$

and for the white phase component,

$$\sigma_\phi = (.070/2)^{\frac{1}{2}} = 0.19 \text{ radians}$$

The 128 one-second phase residuals were also augmented by one point and then 128 fractional frequency residuals were computed by the formula

$$y_k = \frac{\phi_{k+1} - \phi_k}{2\pi(2.2 \times 10^9)}$$

The power spectrum was computed for these residuals as well (Figure 3), and it was found that the resulting $S_y(f)$ could be represented by the following law.

$$S_y(f) = (6.1 \times 10^{-21}) f^2$$

The standard deviation σ_y can be found from

$$\sigma_y^2 = \int_0^{f_N} S_y(f)\, df$$

$$= 1/3(6.1 \times 10^{-21}) f_N^3$$

and

$$\sigma_y = 1.6 \times 10^{-11}$$

There is a small incompatibility between σ_y and σ_ϕ as computed from the two spectra, because for white phase noise, with no correlation between samples, the following relation should hold.

$$\sigma_y^2 = \frac{2\,\sigma_\phi^2}{(2\pi\,\nu_o)^2}$$

If we compute S_ϕ from $S_y = hf^2$, we find that

$$S_\phi = \frac{(2\pi\,\nu_o)^2}{6}\; hf_N^2$$

and for $f_N = \frac{1}{2}$, $\nu_o = 2.2 \times 10^9$, $h = 6.1 \times 10^{-21}$,

$$S_\phi = 0.049$$

which is reasonably close to the high frequency spectrum of Figure 2. The incompatibility is not significant.

Allan Variance

The Allan variance is a two-sample variance for average fractional frequency variations over a cycle count time τ. When we are dealing with phase residuals with trends removed, and the count time is equal to the sample time T, the average fractional frequency variation over T is:

$$\bar{y}_k(T) = \frac{\phi_{k+1} - \phi_k}{2\pi\,\nu_o\,T}$$

which is simply Doppler frequency residuals divided by ν_o.

We can also compute $\bar{y}_k$ for $\tau > T$, but to avoid correlation between samples of $\bar{y}_k$, they must be exactly adjacent in time. This can be accomplished by defining

$$\bar{y}_k(2T) = \tfrac{1}{2}\left[\bar{y}_{2k}(T) + \bar{y}_{2k-1}(T)\right]$$

This produces a list of $\bar{y}_k(2T)$ which is at most one half the size of the list of $\bar{y}_k(T)$. Similarly we can produce a list of $\bar{y}_k(4T)$ which is at best ¼ the size of the list of $\bar{y}_k(T)$, and so on until there are too few values of $\bar{y}_k(\tau)$ to compute a meaningful estimate of the two-sample variance.

The two-sample variance is a little strange, but it is used in practice to characterize oscillator stability. Normally from a sample of N values $\bar{y}_k$, we would compute the mean by

$$\bar{\bar{y}} = \frac{1}{N} \sum_{k=1}^{N} \bar{y}_k$$

Then the unbiased estimate of the variance would be given by

$$\sigma_y^2 = \frac{1}{N-1} \sum_{k=1}^{N} (\bar{y}_k - \bar{\bar{y}})^2$$

If we have only two samples of $\bar{y}_k$, then the above two equations can be combined to yield

$$\sigma_y^2 = \frac{(\bar{y}_2 - \bar{y}_1)^2}{2}$$

The Allan variance is defined as the average of the estimates of the two-sample variance. Therefore, for a list of m values of $\bar{y}_k$, the Allan variance is given by:

$$\sigma_y^2(\tau) = \frac{1}{m-1} \sum_{k=1}^{m-1} \frac{(\bar{y}_{k+1} - \bar{y}_k)^2}{2}$$

We have applied this formula to the 93 phase residuals at a one minute sample rate (T = 60s). First we computed the differenced Doppler residual and divided by 2.2×10^9 to produce a list of 92 values of $\bar{y}_k(T)$. Then 46 values of $\bar{y}_k(2T)$ were

produced and so on. The resulting Allan variances are given in the following table.

τ	m	$\sigma_y(\tau)$
60 s	92	7.21×10^{-13}
120 s	46	3.87×10^{-13}
240 s	23	3.38×10^{-13}
480 s	11	2.75×10^{-13}
960 s	5	1.80×10^{-13}

The five values of $\sigma_y(\tau)$ can be represented by the following law.

$$\sigma_y(\tau) = \frac{5.30 \times 10^{-12}}{\tau^{\frac{1}{2}}}$$

This is an alternative description of noise to the more familiar power spectrum, but in fact they are related through the relation

$$\sigma_y^2(\tau) = 2 \int_0^{f_N} S_y(f) \frac{\sin^4(\pi f \tau)}{(\pi f \tau)^2} \, df$$

For white phase noise ($S_y = hf^2$) this expression can be integrated to yield

$$\sigma_y^2(\tau) = \frac{3hf_N}{(2\pi\tau)^2} + \frac{h}{2(2\pi\tau)^3} \left[\sin(4\pi f_N \tau) - 8\sin(2\pi f_N \tau)\right]$$

and

$$\sigma_y(\tau) \approx \frac{(3hf_N)^{\frac{1}{2}}}{2\pi\tau} \qquad \tau >> 1$$

For the white phase spectrum of the one-second data, the formula yields

$$\sigma_y(\tau) \approx \frac{1.5 \times 10^{-11}}{\tau}$$

The Allan variance for hydrogen maser systems typically reaches 10^{-14} for integration times of 100 s. Therefore the phase noise in the one-second data that we have analyzed is an order of magnitude too large for system noise. It must be caused by something else.

JDA:nm,tg

Distribution:

J. Armstrong
K. Bartos
D. A. Bathker
W. H. Bayley
A. L. Berman
R. R. Breshears
J. F. Boreham
D. W. Brown
D. L. Brunn
H. Buchanan
S. A. Butman
P. S. Callahan
D. L. Cain
R. C. Clauss
W. D. Chaney
R. C. Coffin
D. W. Curkendall
R. W. Davies
N. F. deGroot
R. M. Dickinson
H. Donnelly
W. J. Downhower
M. F. Easterling
P. B. Esposito
F. B. Estabrook
V. L. Evanchuk
W. C. Frey
C. R. Gates
E. C. Gatz
R. R. Green
J. R. Hall
R. W. Hellings
C. W. Johnson
J. F. Jordan
K. R. Kimball
W. E. Kirhofer
T. Komarek
W. G. Leflang
G. S. Levy
W. L. Martin
R. P. Mathison
W. G. Melbourne
R. B. Miller
H. W. Norris
T. Y. Otoshi
E. C. Posner
R. V. Powell
R. A. Preston
W. I. Purdy
L. W. Randolph
D. G. Rea
N. A. Renzetti
K. H. Rourke
H. Royden
E. J. Smith
W. P. Spaulding
G. L. Spradlin
R. Stevens
F. W. Stoller
E. E. Suggs
R. L. Sydnor
C. L. Thornton
T. H. Thornton
C. J. Vegos
R. F. Vessot (SAO)
W. K. Victor
H. D. Wahlquist
C. P. Wiggins
C. F. Winn
R. Woo
G. Wood
M. L. Yeater

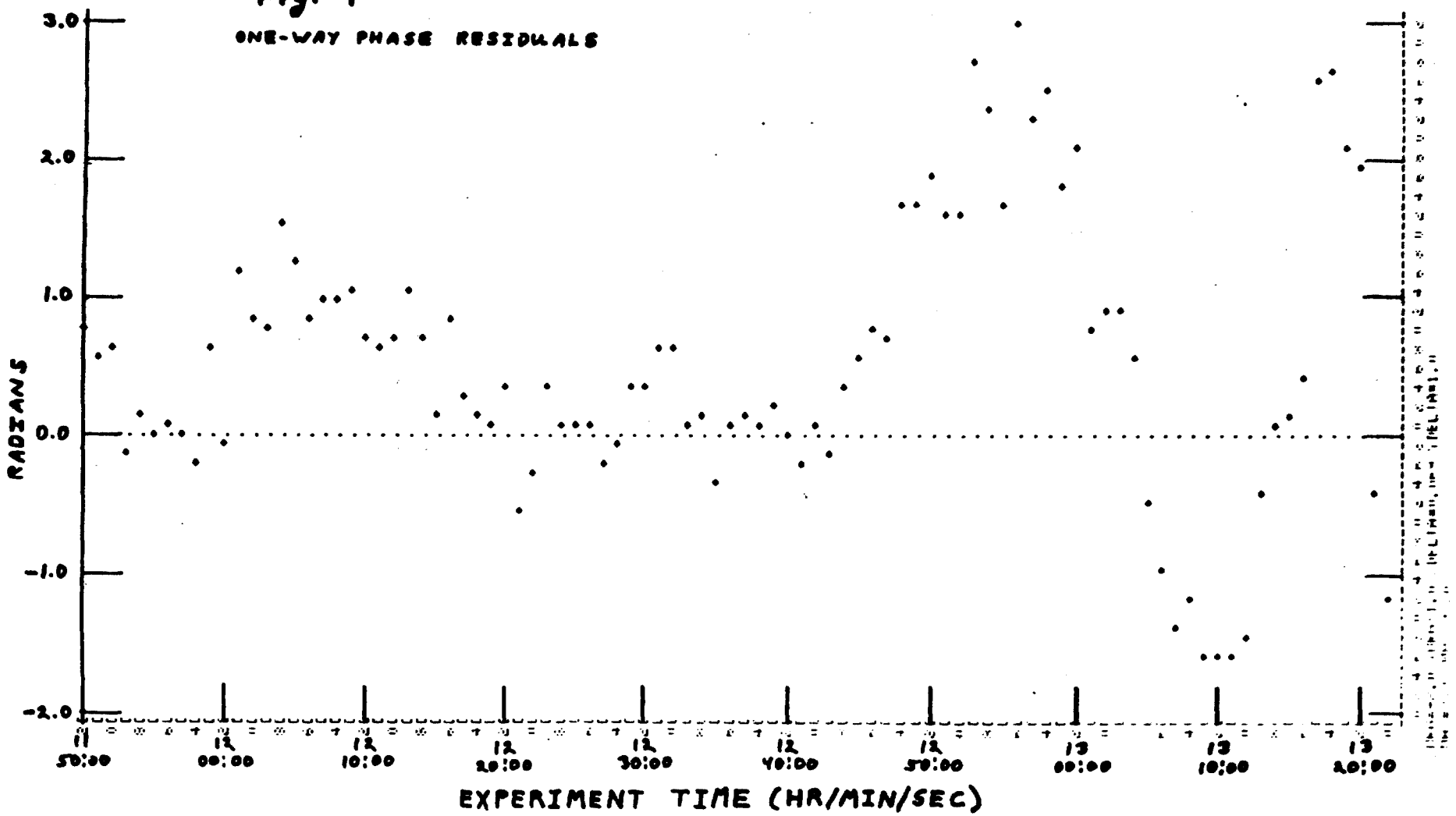
Fig. 1
ONE-WAY PHASE RESIDUALS
3.0
2.0
1.0
0.0
-1.0
-2.0
RADIANS
11 50:00
12 00:00
12 10:00
12 20:00
12 30:00
12 40:00
12 50:00
13 00:00
13 10:00
13 20:00
EXPERIMENT TIME (HR/MIN/SEC)

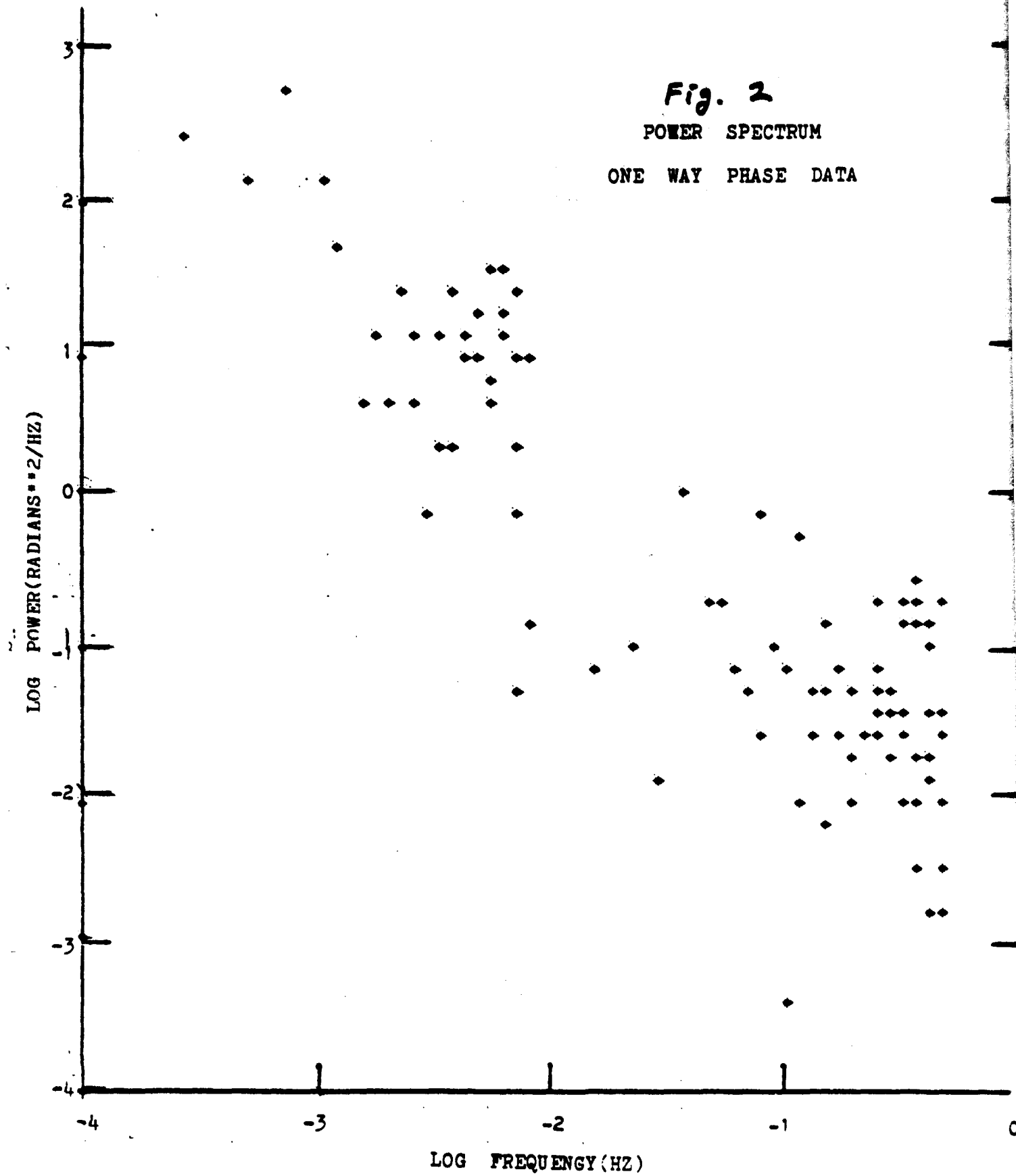

Fig. 2

POWER SPECTRUM

ONE WAY PHASE DATA

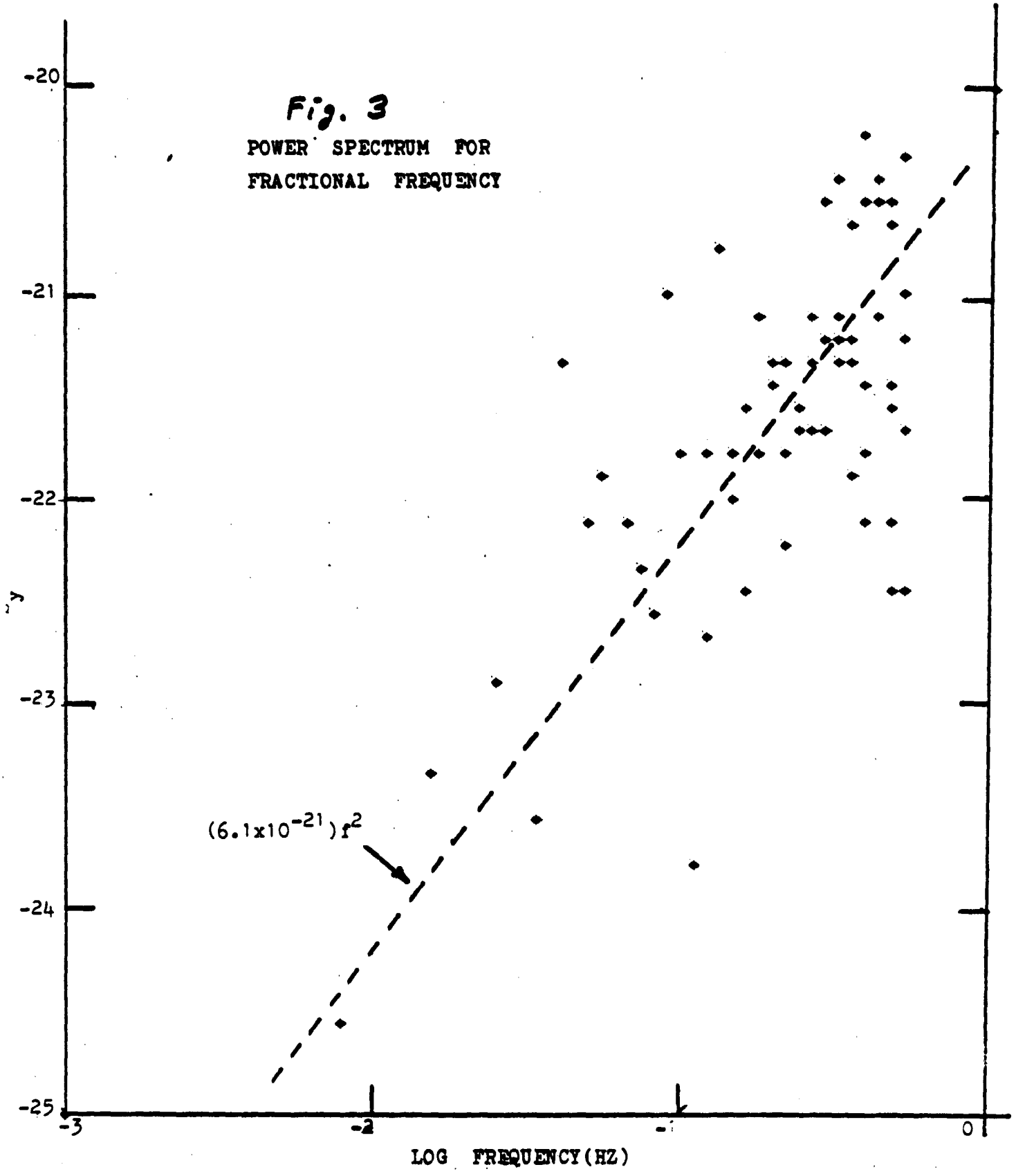
Fig. 3
POWER SPECTRUM FOR
FRACTIONAL FREQUENCY
-20
-21
-22
-23
-24
-25
y
$(6.1 \times 10^{-21}) f^2$
-3
-2
-1
0
LOG FREQUENCY(HZ)